2015-03-25

Terrestrial and Micro-Gravity Studies in Electrohydrodynamic Conduction-Driven Heat Transport Systems

Viral K. Patel
Worcester Polytechnic Institute

TERRESTRIAL AND MICRO-GRAVITY STUDIES IN ELECTROHYDRODYNAMIC CONDUCTION-DRIVEN HEAT TRANSPORT SYSTEMS

by

Viral K. Patel

A Dissertation

Submitted to the Faculty

of the

WORCESTER POLYTECHNIC INSTITUTE

in partial fulfillment of the requirements for the

Degree of Doctor of Philosophy

in

Mechanical Engineering

March 2015

APPROVED:

Dr. Jamal Yagoobi, Major Advisor

Dr. John Blandino, Committee Member

Dr. Brian Savilonis, Committee Member

Dr. Michael Timko, Committee Member

Dr. Cosme Furlong, Graduate Committee Representative

ACKNOWLEDGMENT

I am grateful to the NASA Headquarters – Microgravity Fluid Physics Program for the financial support of this research project. The experiments in microgravity could not be completed without the great efforts of Jeffrey Didion, Franklin Robinson and Mario Martins at NASA Goddard Spaceflight Center and it was a pleasure working with them all. I also thank the members of my dissertation committee, Dr. John Blandino, Dr. Brian Savilonis, Dr. Michael Timko and Dr. Cosme Furlong for their valuable input in my research. I have had many brilliant and inspiring professors throughout my academic career but most of all, I am grateful to my faculty advisor, Dr. Jamal Yagoobi, who gave me this wonderful opportunity for advanced learning and instilled in me the importance of the endless pursuit of knowledge. This, I believe, is the highest ideal anyone can hope to strive for, and I will always appreciate the profound influence he has had on my career and life.

I am forever grateful to my dear family and friends, too many to list here. My grandparents, parents, uncles and aunts, brothers and sisters and good friends; they are literally all over the world. I thank them for listening to me and for always asking about my research even though they knew that I was going to tell them about it. I would not be at this stage in my life without their constant support and guidance. I dedicate this work to them all.

TABLE OF CONTENTS

ACKNOWLEDGMENT iii
LIST OF TABLES vii
LIST OF FIGURES viii
LIST OF SYMBOLS xiv
ABSTRACT xix
CHAPTER 1 - INTRODUCTION 1

1.1 Electrohydrodynamic conduction pumping 1

1.1.1 Electrohydrodynamics 1
1.1.2 EHD conduction analytical model 3
1.1.3 Numerical solution of governing equations for EHD conduction 7
1.1.4 Recent single-phase flow experimental work in EHD conduction 12
1.1.5 Recent flow boiling experimental work in EHD conduction 22

1.2 Enhancement of boiling heat transfer using electrohydrodynamic conduction pumping 27

1.2.1 Pool boiling and liquid film flow boiling 27
1.2.2 Terrestrial work in pool boiling and liquid film flow boiling 30

1.3 Enhancement of boiling heat transfer using dielectrophoresis 39

1.3.1 Dielectrophoresis 39
1.3.2 Terrestrial work in DEP-enhanced pool boiling 44
1.3.3 Microgravity work in DEP-enhanced pool boiling 52

1.4 Objectives of current study 56

CHAPTER 2 – MESO-SCALE EHD CONDUCTION PUMPING OF DIELECTRIC LIQUID: SINGLE-PHASE FLOW STUDIES 58

2.1 Introduction 58
2.2 Terrestrial single-phase flow study 59

2.2.1 Meso-scale EHD conduction pump design 59
2.2.2 Experimental setup and procedure 61
2.2.3 Results and discussion 64

2.3 Micro-gravity single-phase flow study 67

2.3.1 Experimental setup and parabolic flight rack design 67
2.3.2 Experiment procedure during parabolic maneuver 69
2.3.3 Results and discussion 70

2.4 Conclusions 73

CHAPTER 3 – MESO-SCALE EHD CONDUCTION PUMPING OF DIELECTRIC LIQUID: TWO-PHASE FLOW STUDIES 75

3.1 Introduction 75
3.2 Experimental setup 78
3.3 Experimental method to determine flow boiling heat transfer coefficients and vapor quality 81

3.4 Two-phase flow experimental results: EHD-driven evaporator dryout recovery 83
3.5 Fundamental observation of EHD pump net pressure generation 87
3.6 Two-phase flow experimental results: Low mass flux boiling heat transfer coefficients ... 88
3.7 Two-phase flow experimental results: Long-term performance evaluation 95
3.8 Conclusions 103

CHAPTER 4 – ELECTRICALLY DRIVEN LIQUID FILM FLOW BOILING IN THE PRESENCE AND ABSENCE OF GRAVITY 106

4.1 Introduction 106
4.2 Terrestrial and micro-gravity EHD-driven liquid film flow boiling study on bare heater surface 107

4.2.1 EHD pump substrate disc design 107
4.2.2 Experiment housing design and flight rack 110
4.2.3 Experiment procedure during flight 114
4.2.4 Terrestrial results 114
4.2.5 Parabolic flight results 118

4.3 Terrestrial EHD-driven liquid film flow boiling study on nano-fiber enhanced heater surface 124

4.3.1 New heater design 126
4.3.2 Nano-fiber mat deposition process 129
4.3.3 Results and discussion 130

4.4. Conclusions 137

CHAPTER 5 – COMBINED DIELECTROPHORETIC AND EHD CONDUCTION PUMPING FOR ENHANCEMENT OF LIQUID FILM FLOW BOILING 140

5.1 Introduction 140
5.2 Experimental setup 141

5.2.1 EHD pump substrate disc and heater design 141
5.2.2 DEP electrode design 142
5.2.3 Combined EHD and DEP electrode installation 143

5.3 Experimental results and discussion 145
5.4 Numerical simulation of non-uniform electric field in dielectric liquid 152
5.5 Conclusions 160

CHAPTER 6 – CONCLUSIONS AND RECOMMENDATIONS 162

6.1 Conclusions 162
6.2 Recommendations 164

APPENDIX A – UNCERTAINTY ANALYSIS 166

A.1 General uncertainty analysis 166

A.1.1 Systematic or bias errors 166
A.1.2 Random or precision errors 167
A.1.3 Propagation of error for derived quantities 167

A.2 Temperature measurement 170

A.3 Pressure measurement 172
A.4 Flow rate 173
A.5 Voltage and current 174
A.6 EHD voltage and current 175
A.7 Acceleration due to gravity 176
APPENDIX B – NUMERICAL SIMULATION RESULTS FOR ENGINEERING DESIGN. 177
B.1 Meso loop evaporator 177
B.2 Liquid film flow boiling ceramic heater 178
B.3 Liquid film flow boiling copper heater 181
BIBLIOGRAPHY 183

LIST OF TABLES

Table I: EHD pump dimensions corresponding to Figure 7 13

Table II: EHD pump dimensions corresponding to Figure 16 24

Table III: EHD electrode design dimensions corresponding to Figure 21 31

Table IV: EHD electrode design dimensions corresponding to Figure 25 37

Table V: Component dimensions for Figure 35 61

Table VI: Fluid properties of HCFC-123 at 25°C and 1 atm [63] 63

Table VII: Maximum systematic error of various measurement devices for chapter 2 64

Table VIII: Maximum systematic error of various measurement devices and experimental uncertainty for chapter 3 81

Table IX: Maximum systematic error of various measurement devices and experimental uncertainty for chapter 4, section 4.2 113

Table X: Maximum systematic error of various measurement devices and experimental uncertainty for chapter 4, section 4.3 129

Table XI: Select ΔT values and corresponding enhancements for all cases 137

Table XII: Maximum systematic error of various measurement devices and experimental uncertainty for chapter 5 144

Table XIII: Experimental matrix for chapter 5 145

Table XIV: Enhancements in heat flux for ΔT = 14.1°C for all cases 149

LIST OF FIGURES

Figure 1: Schematic depicting stages of EHD conduction process 4

Figure 2: Schematic depicting heterocharge layers attracted towards electrodes during EHD conduction resulting in fluid flow 5

Figure 3: Numerical domain for solution of governing equations in EHD conduction model by Yazdani and Seyed-Yagoobi [19] 10

Figure 4: Numerical results for electric field magnitude in [19] 11

Figure 5: Numerical results for stream traces and contours of electric body force in [19] 11

Figure 6: Numerical results for streamlines of fluid flow in [19] 12

Figure 7: EHD conduction pump design showing flush electrodes embedded into rectangular pumping channel by Pearson and Seyed-Yagoobi [31] 13

Figure 8: Meso-scale EHD conduction pump performance curves as a function of applied potential in [31] 14

Figure 9: Power input and current through EHD electrodes for meso-scale pump as a function of applied potential in [31] 15

Figure 10: Pressure generation at zero flow for micro-scale EHD conduction pump as a function of applied potential [31] 15

Figure 11: Power input and current through EHD electrodes for micro-scale pump as a function of applied potential in [31] 16

Figure 12: EHD conduction micro-pump design of Mahmoudi et al. [32] 18

Figure 13: Comparison between numerical and experimental results of pressure generation for Mahmoudi et al. [32] 18

Figure 14: Flow pattern for six asymmetric electrode pairs by Hemayatkhah et al. [34] 20

Figure 15: Potential distributions measured between EHD pump electrodes and comparison to theory by Hanaoka et al. [37] 21
Figure 16: EHD conduction pump design showing flush electrodes embedded into rectangular pumping channel by Pearson and Seyed-Yagoobi [42] 23
Figure 17: Effect of heat flux on flow rate in two-phase loop at fixed applied potential to EHD electrodes (750V) in [42] 25
Figure 18: Effect of heat flux on evaporator pressure drop in two-phase loop at fixed applied potential to EHD electrodes (750V) in [42] 26
Figure 19: EHD-driven liquid film boiling conceptual schematic 29
Figure 20: Heater dryout at critical heat flux during liquid film flow boiling 30
Figure 21: Pool boiling surface with embedded EHD electrodes by Pearson and Seyed-Yagoobi [43] 31
Figure 22: Pool boiling curve for heater design A in [43] 32
Figure 23: Pool boiling curve for heater design B in [43] 33
Figure 24: Influence of electric body force on critical heat flux – Result of hydrodynamic stability analysis in [43] 35
Figure 25: Condenser surface in liquid film flow boiling experiment with embedded EHD electrodes designed by Pearson and Seyed-Yagoobi [44] 36
Figure 26: Results for liquid film boiling: effect of EHD conduction pumping on boiling curve for two film thicknesses in [44] 38
Figure 27: Electrophoresis and dielectrophoresis in uniform and non-uniform DC electric field 40
Figure 28: Electrophoresis and dielectrophoresis in non-uniform AC electric field 40
Figure 29: Forces acting on a dipole 41

Figure 30: Free and bound charges in a parallel plate capacitor 42
Figure 31: Electrode configuration and forces acting on a single bubble for experiments of Wang et al. [51] 46
Figure 32: Comparison of minimum bubble collision height for theoretical and experimental results (x_i=5 mm for theory calculation) for Wang et al. [51] 48
Figure 33: EHD pool boiling curves of a wire in a non-uniform dc electric field by Kweon and Kim [54] (● 0 kV, ■ 5 kV, ▲ 10 kV, ♦ 15 kV) 49
Figure 34: Assembled EHD pump with 20 pairs of electrodes (top) and individual electrodes and spacers (bottom) 60
Figure 35: Single-pair electrode and spacer arrangement 61
Figure 36: Experimental setup for both single- and two-phase flow terrestrial tests 62
Figure 37: Net EHD pump pressure generation vs. applied EHD voltage for single-phase liquid flow 65
Figure 38: Mass flux vs. applied EHD voltage for single-phase liquid flow 66
Figure 39: Modified experimental setup for single-phase flow micro-gravity tests 68
Figure 40: Vertical equipment rack installed in aircraft for micro-gravity tests 69
Figure 41: Parabolic flight maneuver 70
Figure 42: EHD pump pressure generation and current vs. applied EHD voltage 71
Figure 43: EHD pump flow rate and flow velocity vs. applied EHD voltage 72
Figure 44: EHD pump power consumption vs. applied EHD voltage 73
Figure 45: Evaporator temperature and heater power variation during heat transport and dryout recovery experiments of EHD-driven two-phase flow device 84

Figure 46: Net EHD pump pressure generation and evaporator pressure drop during heat transport and dryout recovery experiments of EHD-driven two-phase flow device 86
Figure 47: Flow boiling heat transfer coefficient of HCFC-123 vs. quality for circular copper tube (D=1.5 mm), with comparison to two correlations 89
Figure 48: Typical EHD pump pressure generation and flow rate for 8-hour experiment 96
Figure 49: Typical applied EHD voltage and current for 8-hour experiment 96
Figure 50: Typical temperature variation for 8-hour experiment 100
Figure 51: EHD pump pressure and flow rate averaged over 7 hours/day for 15 days 101
Figure 52: Applied EHD voltage and current averaged over 7 hours/day for 15 days 101
Figure 53: Heat removal rate for full phase change in evaporator and EHD pump input power averaged over 7 hours/day for 15 days 103
Figure 54: Ceramic substrate electrode disc with lithographically printed electrodes and heater at center 108
Figure 55: Schematic showing electrode dimensions and spacing between electrode pairs for EHD liquid film pump in chapter 4 108
Figure 56: Bottom of heater piece showing printed resistance heater and printed thermistor for heater surface temperature measurement 109
Figure 57: Experiment housing showing fluid, sensor and electrical connections 111
Figure 58: Layout of hardware in Vertical Equipment Rack for variable gravity flight 112
Figure 59: Photograph of completed flight experiment rack 112
Figure 60: Terrestrial results for liquid film flow boiling with and without EHD conduction pumping of liquid film 116

Figure 61: Parabolic flight results for liquid film flow boiling for first 30 min, showing first three parabolas 119

Figure 62: Parabolic flight results for liquid film flow boiling: average data for 0-g and 1.8-g 120

Figure 63: Heater assembly showing copper heater piece installed in Delrin insulator 127

Figure 64: Electrode disc with bare surface copper heater 128

Figure 65: SEM image of copper-plated nanofiber mat 130

Figure 66: Liquid film flow boiling for bare and nano-fiber enhanced surfaces with and without EHD conduction pumping 134

Figure 67: Low heat flux portion of Figure 66 134

Figure 68: Boiling heat transfer coefficient for bare and enhanced surfaces with and without EHD conduction pumping 135

Figure 69: Schematic showing electrode dimensions and spacing between electrode pairs for EHD liquid film pump in chapter 5 142

Figure 70: Stainless steel DEP electrode design 143

Figure 71: Combined EHD and DEP electrode installation in liquid film flow boiling experiment 144

Figure 72: Experimental data for combined EHD- and DEP-enhanced liquid film flow boiling and pool boiling 146

Figure 73: Low heat flux data for all cases from Figure 72 147

Figure 74: Image of liquid film flow boiling with film thickness: 2.0 mm, Heat flux: 15.0 W/cm^2, Applied EHD potential: 2.0 kV, Applied DEP potential: 2.5 kV 151

Figure 75: Image of pool boiling with pool depth: 10.0 mm, Heat flux: 12.0 W/cm^2, Applied EHD potential: 0 kV, Applied DEP potential: 2.5 kV 152

Figure 76: Heater/DEP electrode geometry 153

Figure 77: Electric potential (top left and right) and electric field distribution (bottom left and right) for heater/DEP electrode geometry 154

Figure 78: x-locations for electric field calculations 155

Figure 79: Square of electric field magnitude along y-axis at various x-locations 156

Figure 80: Estimation of DEP force magnitude along y-axis at various x-locations vs. buoyancy force for 0.5 mm bubble diameter 157

Figure 81: Results of Rohsenow correlation [89] for prescribed heat fluxes, estimated effect of DEP force on boiling curves and comparison to experimental data 159

Figure 82: Typical calibration curve for differential pressure transducer 172

Figure 83: Calibration curve for flow meter 174

Figure 84: Copper evaporator tube temperature distribution 178

Figure 85: Copper evaporator tube radial heat flux distribution 178

Figure 86: Ceramic heater temperature distribution for q = 35W, non-uniform heat transfer coefficient 180

Figure 87: Ceramic heater axial heat flux for q = 35W, non-uniform heat transfer coefficient . 180

Figure 88: Ceramic heater axial heat flux for q = 35W, non-uniform heat transfer coefficient . 181

Figure 89: Temperature distribution for q" = 35 W/cm^2 182

Figure 90: Temperature distribution and arrows showing heat flux for q" = 35 W/cm^2 182

LIST OF SYMBOLS

a	Bubble radius, m
A	Heat transfer surface area of evaporator, based on tube inner diameter, m^2
A_c	Cross-sectional area of evaporator, m^2
b	Ion mobility, $m^2/V{\cdot}s$
Bo	Boiling number = $\frac{q''}{Gh_{fg}}$
c	Concentration of neutral species
C_0	Dimensionless parameter, defined by Eq. (18)
Co	Convection number = $\left(\frac{1-x}{x}\right)^{0.8}\left(\frac{\rho_v}{\rho_l}\right)^{0.5}$
Cn	Confinement number = $\left(\frac{\sigma}{g(\rho_l-\rho_v)D_h^2}\right)^{\frac{1}{2}}$
c	Neutral species concentration
c_p	Specific heat, kJ/kg·K
d	Spacing distance, m
	Characteristic length, m
$\boldsymbol{d}$	Dipole separation, m
D	Evaporator tube inner diameter, m
	Ion diffusion coefficient
D_h	Hydraulic diameter, m
e	Electron charge, C
$\boldsymbol{E}$	Electric field vector, V/m
E	Electric field intensity, V/m

$\boldsymbol{f}_e$ Electric body force density, N/m^3

$\boldsymbol{F}$ Force vector, N

F Convection heat transfer correction factor

F_{Fl} Fluid-surface parameter

$\boldsymbol{g}$ Gravitational acceleration vector, m/s^2

G Mass flux through evaporator = $\frac{\dot{m}}{A_c}$, kg/m^2·s

h_i Local heat transfer coefficient at thermocouple station i, W/m^2·K

$h_{conv,tp}$ Convective heat transfer term, W/m^2·K

h_{fg} Latent heat of vaporization, kJ/kg

h_{FB} Flow boiling heat transfer coefficient, W/m^2·K

h_{NB} Nucleate boiling component of overall flow boiling heat transfer coefficient, W/m^2·K

$h_{FB,NBD}$ Flow boiling heat transfer coefficient for only nucleate boiling-dominant flow, W/m^2·K

h_{LO} Single-phase, laminar, all-liquid flow heat transfer coefficient, W/m^2·K

I_1 Modified Bessel function of the first kind

J_e Joule heating term, W/m^3

k Thermal conductivity, W/m·K

k_B Boltzmann constant, J/K

k_d Field enhanced dissociation rate

k_D Dissociation rate constant

k_R Recombination rate constant

l_i Distance from evaporator inlet to thermocouple station i, m

L Overall length of evaporator, m

M_0 Mobility ratio, defined by Eq. (18)

$\dot{m}$ Mass flow rate of refrigerant, kg/s

m_{eff} Effective mass, kg

Nu Nusselt number = $Nu_i = \frac{h_i D}{k_l}$

n Negative charge density, C/m^3

p Positive charge density, C/m^3

$\boldsymbol{p}$ Dipole moment, Cm

$\boldsymbol{P}$ Polarization density, C/m^2

P Pressure, Pa

P_{sat} Saturation pressure, Pa

Pe Peclet number defined by Eq. (18)

Pr Prandtl number

q Heat transfer rate, W

Electric charge, C

q'' Heat flux, W/m^2

$\boldsymbol{r}$ Position vector, m

$\mathrm{Re_{EHD}}$ EHD Reynolds number defined by Eq. (18)

$\mathrm{Re_{LO}}$ All-liquid flow Reynolds number = $\frac{GD}{\mu_l}$

$\mathrm{Re_{VO}}$ All-vapor flow Reynolds number = $\frac{GD}{\mu_v}$

S Nucleate boiling suppression factor

t Time, s

T Temperature, K

$T_{S,i}$ Evaporator wall surface temperature at thermocouple station i, K

$T_{sat,exit}$ Evaporator exit saturation temperature, K

ΔT Temperature difference, K

$\boldsymbol{u}$ Fluid velocity vector, m/s

$\boldsymbol{v}$ Particle velocity vector, m/s

$\dot{\boldsymbol{v}}$ Particle acceleration vector, m/s^2

u_e EHD velocity, m/s

V Applied voltage, V

Volume, m^3

x_i Vapor quality at thermocouple station i

x x-coordinate, m

y y-coordinate, m

Greek Symbols

$\boldsymbol{\Gamma}$ Particle flux vector, $C/s \cdot m^2$

α Dimensionless parameter, defined by Eq. (21)

ε Electric permittivity, F/m

κ Dielectric constant

μ Dynamic viscosity, $N \cdot s/m^2$

ν Kinematic viscosity

ρ Density, kg/m^3

ρ_e Net charge density, C/m^3

σ Surface tension, N/m

σ_e Electric conductivity, S/m

ϕ Electric potential, V

Subscripts

eq Equilibrium

l Liquid

v Vapor

+ Positive ions

- Negative ions

Superscripts

* Non-dimensional

ABSTRACT

Electrohydrodynamic (EHD) phenomena involve the interaction between electrical and flow fields in a dielectric fluid medium. In EHD conduction, the electric field causes an imbalance in the dissociation-recombination reaction of neutral electrolytic species, generating free space charges which are redistributed to the vicinity of the electrodes. Proper asymmetric design of the electrodes generates net axial flow motion, pumping the fluid. EHD conduction pumps can be used as the sole driving mechanism for small-scale heat transport systems because they have a simple electrode design, which allows them to be fabricated in exceedingly compact form (down to micro-scale). EHD conduction is also an effective technique to pump a thin liquid film. However, before specific applications in terrestrial and micro-gravity thermal management can be developed, a better understanding of the interaction between electrical and flow fields with and without phase-change and in the presence and absence of gravity is needed.

With the above motivation in mind, detailed experimental work in EHD conduction-driven single- and two-phase flow is carried out. Two major experiments are conducted both terrestrially and on board a variable gravity parabolic flight. Fundamental behavior and performance evaluation of these electrically driven heat transport systems in the respective environments are studied. The first major experiment involves a meso-scale, single-phase liquid EHD conduction pump which is used to drive a heat transport system in the presence and absence of gravity. The terrestrial results include fundamental observations of the interaction between two-phase flow pressure drop and EHD pump net pressure generation in meso-scale and short-term/long-term, single- and two-phase flow performance evaluation. The parabolic flight results show operation of a meso-scale EHD conduction-driven heat transport system for the first time in microgravity. The second major experiment involves liquid film flow boiling driven by

EHD conduction in the presence and absence of gravity. The terrestrial experiments investigate electro-wetting of the boiling surface by EHD conduction pumping of liquid film, resulting in enhanced heat transfer. Further research to analyze the effects on the entire liquid film flow boiling regime is conducted through experiments involving nanofiber-enhanced heater surfaces and dielectrophoretic force. In the absence of gravity, the EHD-driven liquid film flow boiling process is studied for the first time and valuable new insights are gained. It is shown that the process can be sustained in micro-gravity by EHD conduction and this lays the foundation for future experimental research in electrically driven liquid film flow boiling. The understanding gained from these experiments also provides the framework for unique and novel heat transport systems for a wide range of applications in different scales in terrestrial and microgravity conditions.

CHAPTER 1 - INTRODUCTION

1.1 Electrohydrodynamic conduction pumping

1.1.1 Electrohydrodynamics

The use of strong electric fields to generate electrical body forces and induce motion in either liquids or gases has been studied in detail for more than a century. This area of research, where the interaction between electric fields and fluid flow is investigated, is known as electrohydrodynamics (EHD). There are many types of EHD phenomena which are distinguished by the type of fluid being studied and the geometry of electrodes (which result in a uniform or non-uniform electric field). These determine the dominant electric body force that is generated. A general expression of the electric body force in EHD phenomena is given by Eq. (1) [1].

$$\boldsymbol{f}_e = \rho_e \boldsymbol{E} - \frac{1}{2} E^2 \nabla \varepsilon + \frac{1}{2} \nabla \left[E^2 \left(\frac{\partial \varepsilon}{\partial \rho} \right)_T \rho \right] \tag{1}$$

The first term in Eq. (1) represents the Coulomb force which acts on free charges within the fluid. The second term and third terms represent the translational and distortional responses of polarized charges resulting from the imposed electric field and are known as the dielectrophoretic and electrostriction forces, respectively. For isothermal, incompressible liquids, these forces can be neglected. There are three types of dielectric liquid pumping techniques that rely on the Coulomb force to function: ion-drag, induction and conduction pumping [2]. The focus of this work is on conduction pumping but brief descriptions of ion-drag and induction pumping techniques are given here. In addition, dielectrophoresis is described in detail in later sections.

Ion-drag pumping involves creation of space charge by injecting ions into the fluid via corona source from an emitter electrode. The electric field is formed between the emitter and collector electrode; ions move along the electric field lines to the collector. As they move, they drag surrounding fluid and this effect can be used to generate fluid motion. Ion-drag pumping has been studied for decades and earlier theoretical and experimental work was done by Steutzer [3], Pickard [4, 5] and Krawinkel [6], among others. Research in ion-drag pumping is limited because over time it results in electrode damage and degradation in properties of the working fluid which limits potential long-term applications. However, there is still some ongoing work, such as recent experimental research by Foroughi et al. [7]. They developed a micro-scale ion-drag pump for cryogenic spot-cooling and bioengineering applications. The working fluid tested was liquid nitrogen and two pump designs were investigated. The first consisted of flat emitter and collector electrodes and the second consisted of a saw-tooth design for the emitter electrode. Electrode spacing was on the order of 50 μm and spacing between consecutive electrode pairs was on the order of 100 μm. Static pressure generation and current were measured to characterize the performance. They found that the pumps were able to generate up to 30 Pa at an applied potential of 1,700V. The saw-tooth design also performed favorably compared to the flat design, because of improved ion-injection at the tip of the sharp electrodes. Other recent numerical and experimental research in ion-drag pumping can be found in [8] and [9] and references therein.

Induction pumping works on the basis of induced charges due to a gradient or discontinuity in electric conductivity of the liquid. Charges can be repelled or attracted using a traveling AC wave and this leads to fluid motion. The technique can be used in a stratified liquid/vapor medium for applications in flow management or heat transfer enhancement. The

concept was introduced by Melcher [10] and references for initial theoretical and numerical research can be found in the summary paper by Seyed-Yagoobi [2]. More recently, induction pumping has been used in thermal management applications, such as experimental work by Brand and Seyed-Yagoobi [11]. They studied induction pumping of a dielectric micro liquid film in external horizontal condensation and its effect on heat transfer from a fundamental perspective. The induction pump was fabricated by wrapping insulated wiring around the external surface of a copper tube and applying an AC traveling wave to the wire. Liquid condensing on the outer surface of the copper tube formed a thin micro-layer and was pumped by the induction technique and this improved the condensation heat transfer. The voltage and frequency of the traveling wave were varied and surface/bulk temperatures were measured. They were able to gain a new understanding of EHD induction and characterize the performance based on significant improvement in condensation heat transfer coefficient for a given attraction pumping mode. The use of EHD induction in this way for thermal management is one of the areas of ongoing research.

1.1.2 EHD conduction analytical model

EHD conduction differs from the above techniques in the way space charge is generated within the dielectric liquid. Rather than ion injection, for example, it relies on the process of dissociation/recombination. A review of recent advances in EHD conduction pumping can be found in [12]. A simple conduction model was first proposed by Atten and Seyed-Yagoobi [13] (and later built upon) and it involves a reversible dissociation-recombination process of neutral electrolytic species AB into univalent positive A^+ and negative B^- ions, as shown in Eq. (2).

$$AB \overset{Disocciation}{\underset{Recombination}{\longleftrightarrow}} A^+ + B^- \tag{2}$$

At thermodynamic equilibrium when the applied electric field is low, the dissociation and recombination rates are constant. However, when the field exceeds a certain threshold (which is a function of fluid properties) the rate of dissociation becomes higher than that of recombination. This results in an excess of ions which are free to move in the liquid. The charges move along the electric field lines due to the Coulomb force in Eq. (1) and are redistributed in the vicinity of the electrodes. There they form layers of charge opposite to that of the adjacent electrode, referred to as heterocharge layers. Fluid motion occurs when the heterocharge layers are attracted towards the electrodes. This process is illustrated in Figure 1.

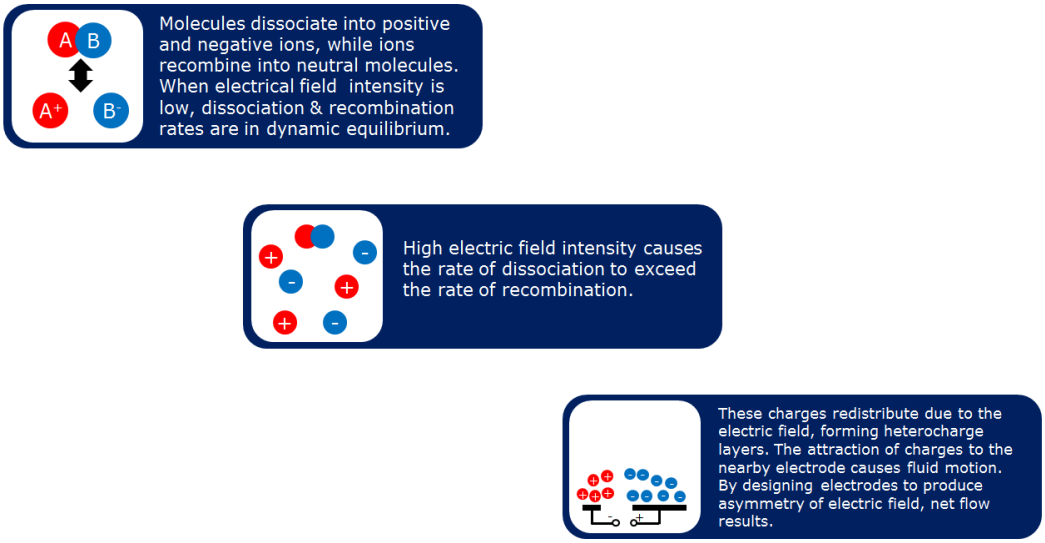

Figure 1: Schematic depicting stages of EHD conduction process

Fluid flow in a given direction can only occur if there is a net electric body force. The imbalance required to generate a net force can be imposed by designing asymmetric electrodes as shown in Figure 2.

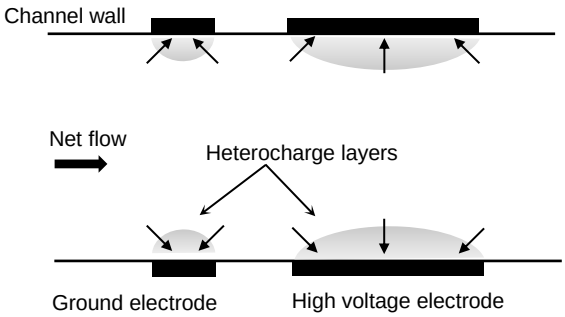

Figure 2: Schematic depicting heterocharge layers attracted towards electrodes during EHD conduction resulting in fluid flow

In the configuration described above, the flow is from the narrow electrode to the high voltage electrode. This has been demonstrated numerically as will be shown in the next section. The Coulomb force manifests itself in the governing equations for fluid flow in the form of an electric body force density. For steady-state conditions in an incompressible, Newtonian fluid, the continuity, momentum and energy equations are

$$\nabla \cdot \boldsymbol{u} = 0 \tag{3}$$

$$\rho(\boldsymbol{u} \cdot \nabla)\boldsymbol{u} = -\nabla P + \mu\nabla^2\boldsymbol{u} + \rho\boldsymbol{g} + \rho_e\boldsymbol{E} \tag{4}$$

$$\rho c_p(\boldsymbol{u} \cdot \nabla T) = k_l\nabla^2 T + J_e \tag{5}$$

where the last term on the right hand side of Eq. (4) represents the electric body force density and the last term on the right hand side of Eq. (5) represents Joule or Ohmic heating. In order to determine the electric body force and solve for the velocity field in these equations, the net charge density, ρ_e, and electric field vector, $\boldsymbol{E}$, must be known. The net charge density is determined from the equations of charge distribution within a control volume. As noted above, the EHD conduction model involves neutral species that dissociate into positive ions and

negative ions and recombine. Equations (6) and (7) govern the positive and negative charge densities, *p* and *n*:

$$\frac{\partial p}{\partial t} + \nabla \cdot \boldsymbol{\Gamma}_+ = k_D c - k_R p n \tag{6}$$

$$\frac{\partial n}{\partial t} + \nabla \cdot \boldsymbol{\Gamma}_- = k_D c - k_R p n \tag{7}$$

In the above equations, the first terms on the left hand side are the rates of change of charge density. The second terms represent the particle flux vector, $\boldsymbol{\Gamma}$ (described in detail below). The first and second terms on the right hand side represent dissociation of neutral species (*c* is the neutral species concentration) and recombination of positive and negative ions, respectively. Here k_D and k_R are the constant rates of dissociation and recombination. The particle flux vector describes how the charged particles leave or enter the control volume through the sides and contains the following terms for the positive and negative ions:

$$\boldsymbol{\Gamma}_+ = b_+ p \boldsymbol{E} + p \boldsymbol{u} - D_+ \nabla p \tag{8}$$

$$\boldsymbol{\Gamma}_- = -b_- n \boldsymbol{E} + n \boldsymbol{u} - D_- \nabla n \tag{9}$$

The first term on the right hand side represents the mobility (*b* is the mobility coefficient), i.e. the motion of the charge carriers in the fluid due to the electric field. The second term represents charge motion due to fluid convection. The final term represents charge diffusion (*D* is the diffusion coefficient) due to thermal kinetic effects. The electric field vector is found from Gauss's law in Eq. (10) and the electric field is related to electric potential using Eq. (11).

$$\nabla \cdot \boldsymbol{E} = \frac{\rho_e}{\varepsilon} = \frac{p - n}{\varepsilon} \tag{10}$$

$$\boldsymbol{E} = -\nabla\phi \tag{11}$$

As can be seen, the above equations are coupled together. In order to determine the charge distribution, the fluid velocity must be known in order to account for convection. However, the space charge must be known to determine the electric field, which will in turn determine the electric body force and influence the flow field. The above equations have been solved numerically with certain assumptions, boundary conditions and fluid properties and recent results are discussed in the next section.

1.1.3 Numerical solution of governing equations for EHD conduction

Some of the first theoretical and numerical confirmations of the above analytical model that accounted for fluid flow were done by Jeong et al. [14, 15] and Feng and Seyed-Yagoobi [16, 17]. More recently, Yazdani and Seyed-Yagoobi [18-25] have performed detailed numerical simulations. From the theoretical model above, the governing equations were nondimensionalized and the velocity field and pressure generation in a thin film of liquid were computed. However, before the numerical simulation could be done, certain assumptions were made. The first of these was that mobility and diffusion coefficients are equal for both the positive and negative charge carriers.

$$b_+ = b_- = b \text{ and } D_+ = D_- = D \tag{12}$$

The constant dissociation rate was also replaced with a field-enhanced dissociation term. The dissociation was thus a function of the external electric field and temperature. The field-enhanced dissociation model was first introduced by Onsager [26] and is given here as

$$k_d = k_D F(\omega) = k_D \frac{I_1(2\omega)}{\omega},\ \omega = \sqrt{\frac{e^3\|\boldsymbol{E}\|}{4\pi\varepsilon k_B^2 T^2}} \tag{13}$$

where I_1 is the Bessel function of the first kind. The field-enhanced dissociation model replaced the constant dissociation, k_D, with the field-dependent dissociation, k_d, in the charge distribution equations (Eqs. (6) and (7)). The variables appearing in the governing equations were non-dimensionalized in the following ways for the charge densities, electric field, electric potential, pressure, velocity, temperature and gradient operator:

$$\begin{gathered} p^* = \frac{p}{n_{eq}} \qquad n^* = \frac{n}{n_{eq}} \qquad \boldsymbol{E}^* = \frac{\boldsymbol{E}}{V/d} \qquad \phi^* = \frac{\phi}{V} \\ P^* = \frac{P}{\mu^2/\rho d^2} \qquad \boldsymbol{u}^* = \frac{\boldsymbol{u}}{u_e} = \frac{\boldsymbol{u}}{bV/d} \qquad T^* = \frac{u_e^2}{c_p} \qquad \nabla = \frac{\nabla^*}{d} \end{gathered} \tag{14}$$

where *eq* represents equilibrium values. Substituting the above non-dimensional quantities into Eqs. (3) and (4) resulted in the following equations for continuity, momentum and energy:

$$\nabla^* \cdot \boldsymbol{u}^* = 0 \tag{15}$$

$$(\boldsymbol{u}^* \cdot \nabla)\boldsymbol{u}^* = -\left(\frac{1}{Re_{EHD}}\right)^2 \nabla^* P^* + \frac{1}{Re_{EHD}} \nabla^{*^2} \boldsymbol{u}^* + M_0^2 C_0 (p^* - n^*)\boldsymbol{E}^* \tag{16}$$

$$(\boldsymbol{u}^* \cdot \nabla^* T^*) = \frac{1}{Pe} \nabla^{*2} T^* + J_e^* \tag{17}$$

where

$$Re_{EHD} = \frac{\rho b V}{\mu} \qquad Pe = Re_{EHD} Pr \qquad M_0 = \sqrt{\frac{\varepsilon}{\rho b^2}}$$
$$C_0 = \frac{n_{eq} d^2}{\varepsilon V} = \frac{\sigma_e d^2}{2 b \varepsilon V} \qquad J_e^* = J_e \left(\frac{c_p d^2}{Pe k_l u_e^2} \right) \tag{18}$$

where Re_{EHD} was the EHD Reynolds number and M_0 was the mobility ratio. The parameter C_0 was the dimensionless form of n_{eq} and was also thought of as half the ratio between ionic transit time and charge relaxation time. The ionic transit time corresponds to the required time for a charged particle to travel the distance between the electrodes with a velocity of bE (mobility limit). The charge relaxation time represents the time during which a charged particle maintains its charge in a medium. In the same way, equations (6) and (7) for charge distribution became the following when non-dimensionalized:

$$\nabla^* \cdot (p^*(\boldsymbol{u}^* + \boldsymbol{E}^*) - \alpha \nabla^* p^*) = 2C_0(F(\omega) - p^* n^*) \tag{19}$$

$$\nabla^* \cdot (n^*(\boldsymbol{u}^* - \boldsymbol{E}^*) - \alpha \nabla^* n^*) = 2C_0(F(\omega) - p^* n^*) \tag{20}$$

where

$$\alpha = \frac{D}{bV} = \frac{k_B T}{eV} \tag{21}$$

The quantity α was dependent on the applied voltage and diffusion coefficient and was a coefficient of the diffusion terms in equations (19) and (20). Finally, the electric field equations were as follows

$$\nabla^* \cdot \boldsymbol{E}^* = C_0(p^* - n^*) \tag{22}$$

$$\boldsymbol{E}^* = -\nabla^* \phi^* \tag{23}$$

From the above equations, we see that C_0 was the essential dimensionless parameter for charge transport and electric field distribution. In addition, the mobility ratio M_0 appears as the coefficient of the electric body force term in equation (16). The above non-dimensional equations were solved numerically in [19] in order to determine the velocity field and pressure generation in a thin film of liquid. The numerical domain is given in Figure 3.

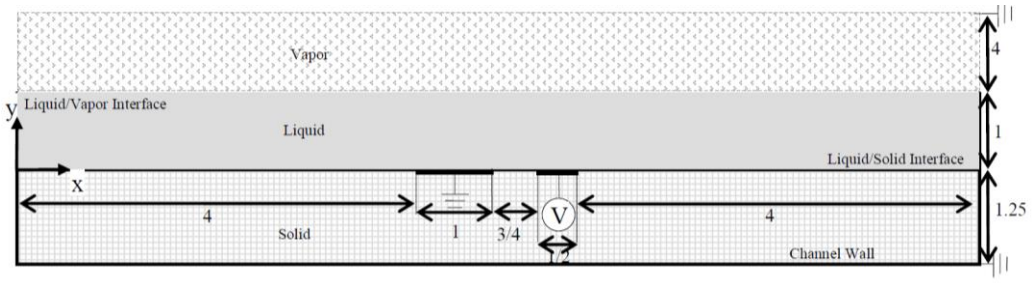

Figure 3: Numerical domain for solution of governing equations in EHD conduction model by Yazdani and Seyed-Yagoobi [19]

The flow was assumed to be steady, laminar and isothermal. The numerical domain was two-dimensional and the channel wall was assumed to be an insulator. The liquid-vapor interface was assumed to be flat and the vapor phase had properties of a vacuum (motionless with no volumetric electric charge). Charge injection was absent. Details of the boundary conditions can be found in [19]. The transport equations were solved using Finite Difference discretization scheme with second order accuracy and the numerical results from [19] are given in the graphs that follow. They show that the net flow generated was solely due to EHD conduction pumping. The properties of refrigerant HCFC-123 were used in the nondimensionalization. Figure 4 shows the electric field distribution in the form of streamlines and contours of electric field magnitude. As can be seen in the figure, the direction of the electric field is from the high potential surface (shown as the red high voltage electrode) to the low potential surface (shown as the blue ground electrode).

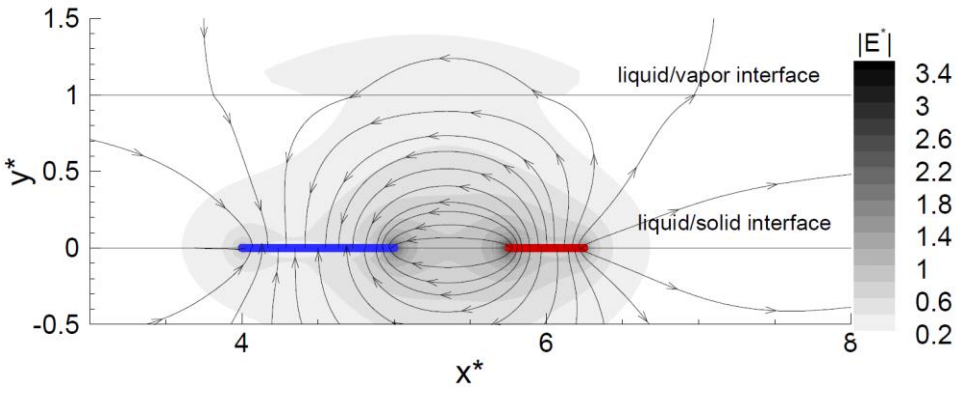

Figure 4: Numerical results for electric field magnitude in [19]

The electric body force distribution is shown in Figure 5. The inter-electrode region is the origin for most of the force and it is directed towards both electrodes. However, due to the asymmetry, there is a dominance of negative streamwise electric body force. This results in fluid motion in the negative streamwise direction (i.e. $-x^*$ direction) and the flow is from right to left. In addition to this, the streamlines of the flow also show vortex like circulations, as shown in Figure 6. The results indicate that the majority of electric body forces and fluid motion are in the vicinity of the electrodes.

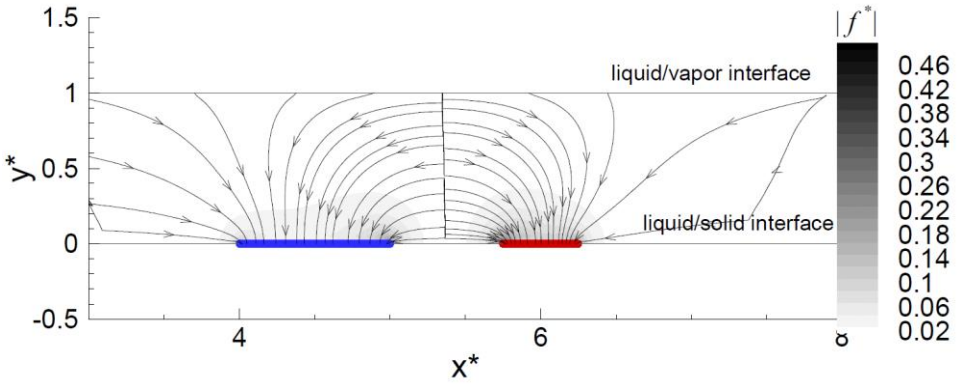

Figure 5: Numerical results for stream traces and contours of electric body force in [19]

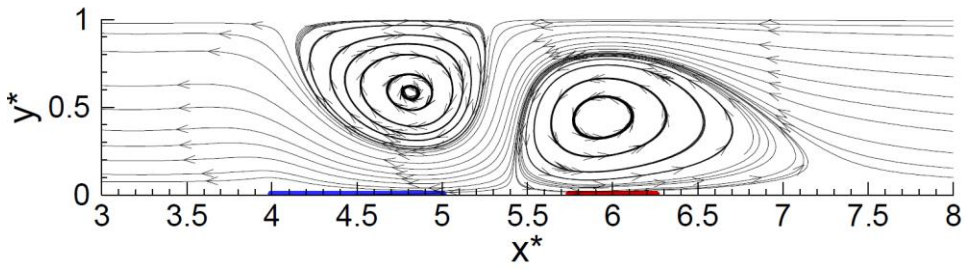

Figure 6: Numerical results for streamlines of fluid flow in [19]

1.1.4 Recent single-phase flow experimental work in EHD conduction

Although the theoretical modelling and numerical simulation of EHD conduction pumping is well-established, it is difficult to incorporate all of the above-mentioned processes at once in the solution of the governing equations. For these reasons, experimental work is necessary in order to make a detailed study of EHD conduction-driven heat transport. Extensive macro-scale experimental research in single-phase EHD conduction pumping has been conducted and select work can be found in [27-30]. However, as mentioned above, the focus of recent research in EHD conduction pumping of dielectric liquids has moved from macro-scale towards meso- and micro-scale. From a practical standpoint, meso- and micro-scale EHD pumps also require lower applied potential to operate (applied potential in macro-scale EHD conduction pumps is typically 10-20 kV, whereas it is 0.5-4 kV for meso- and micro-scale pumps). Pearson and Seyed-Yagoobi [31] investigated a new rectangular channel EHD conduction pump design in both meso- and micro-scale. The pumps were installed into a single-phase loop and pressure generation and flow rate were measured as a function of applied potential to the EHD electrodes. The working fluid was refrigerant HCFC-123. The pump design is shown in Figure 7 and details of dimensions are in Table I.

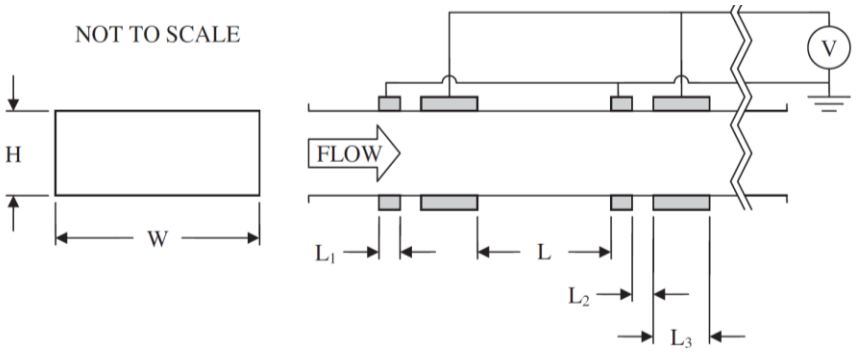

Figure 7: EHD conduction pump design showing flush electrodes embedded into rectangular pumping channel by Pearson and Seyed-Yagoobi [31]

Table I: EHD pump dimensions corresponding to Figure 7

Dimension	Meso-scale Pump	Micro-scale Pump
W (mm)	12.7 ± 0.3	12.7 ± 0.3
H (mm)	1.016 ± 0.051	0.254 ± 0.026
L1 (mm)	0.254 ± 0.013	0.051 ± 0.003
L2 (mm)	0.254 ± 0.026	0.051 ± 0.013
L3 (mm)	0.914 ± 0.102	0.178 ± 0.013
L4 (mm)	3.175 ± 0.254	0.794 ± 0.077
Number of electrode pairs	10	10

The pumps were made of stainless steel disc electrodes and PTFE insulating spacers with rectangular slots cut into them. Electrodes were embedded into the pumping channel and there was no additional resistance to fluid flow. The electrodes and spacers had differing thicknesses which gave a non-uniform electrical field. Electrode and spacer dimensions, as well as optimum spacing between electrode pairs were all determined from numerical simulations in [19]. As shown in Figure 7, all narrow electrodes were connected to ground and all wide electrodes were connected to the high voltage source. For both pumps, 10 pairs of electrodes were combined; the

pressure and flow generation of these combined electrode-pairs was measured. The results for the meso-scale pump performance are shown in Figure 8.

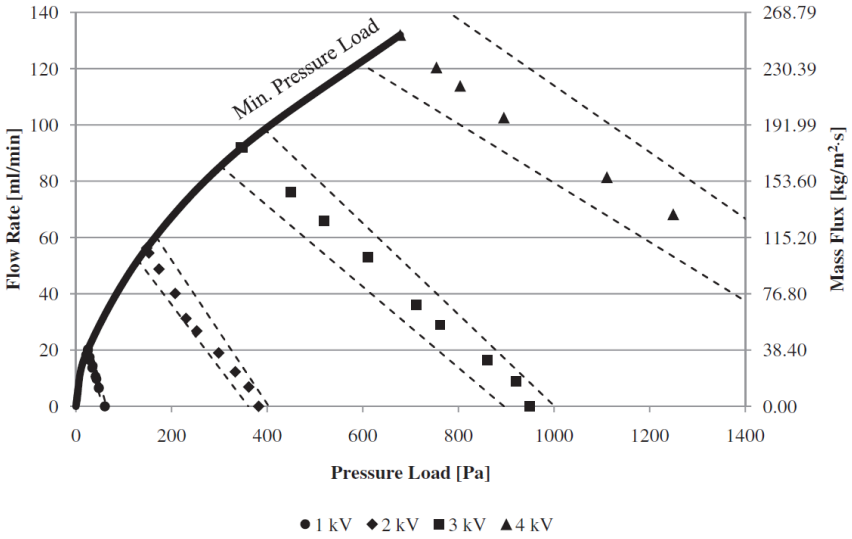

Figure 8: Meso-scale EHD conduction pump performance curves as a function of applied potential in [31]

For a given applied potential, the pressure across the EHD pump was measured. The first measurement was for the pressure at zero flow; these points fell on the horizontal axis in the above figure. Next, a needle valve downstream of the pumping section was opened slightly to allow liquid to circulate in the loop. When the liquid flowed, there was a frictional pressure drop in the tubing of the loop and the EHD pump channel itself. Therefore the net pressure across the EHD pump is what is shown in Figure 8. When data were recorded, the valve was opened further. This process was repeated until the valve was fully open; this was the maximum flow condition. The pressure/flow rate curve was found for four separate applied potentials, as shown above. The power input and current through EHD electrodes was also measured and this is given in Figure 9. Although the maximum applied potential was 4 kV, the current was 0.225 mA which resulted in a maximum power input of 0.9 W.

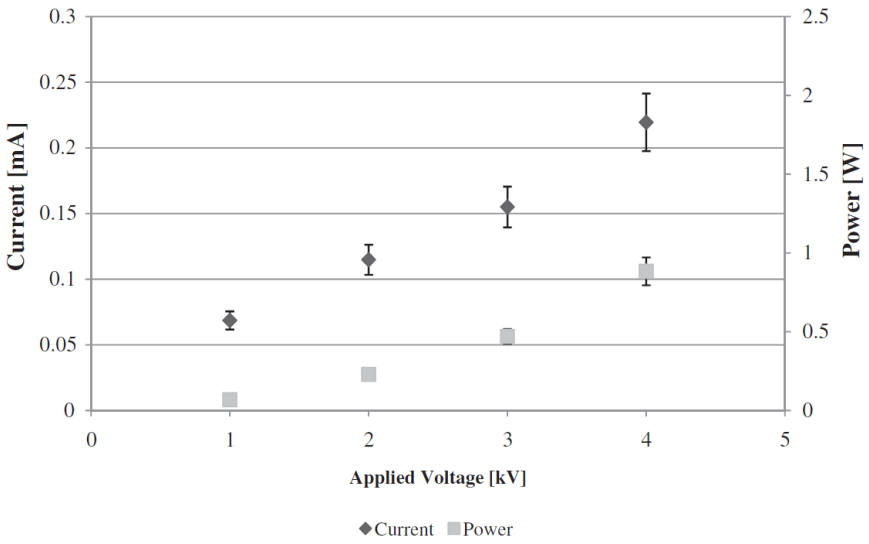

Figure 9: Power input and current through EHD electrodes for meso-scale pump as a function of applied potential in [31]

The performance of micro-scale pump was markedly different. As expected, the net pressure and corresponding flow rate were lower than the meso-scale pump as shown in Figure 10.

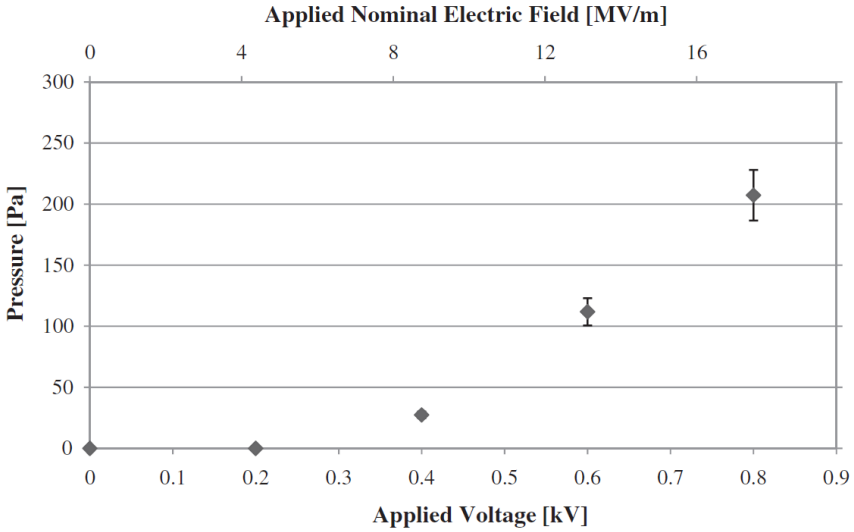

Figure 10: Pressure generation at zero flow for micro-scale EHD conduction pump as a function of applied potential [31]

The performance of the micro-scale pump could not be characterized in the same way as the meso-scale pump. The reason was that the intermediate conditions between zero flow and maximum flow (or minimum pressure) could not be measured accurately. Therefore only the end cases were recorded as a function of applied potential and Figure 10 shows net EHD pressure at zero flow. The maximum applied potential was 800V, compared to 4 kV in the meso-scale pump. These potentials were not exceeded as they caused arcing between electrodes and could have been damaging to their respective EHD pumps. The power input and current for the micro-scale pump were also measured. The current was found to be 3-5 times lower than that of the meso-scale pump, as shown in Figure 11.

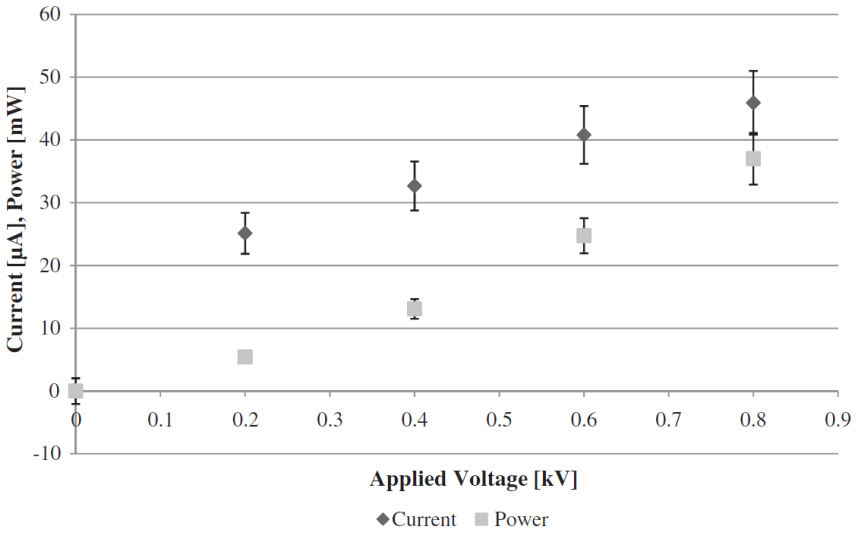

Figure 11: Power input and current through EHD electrodes for micro-scale pump as a function of applied potential in [31]

The power consumption was also reduced by a factor of 20-25 for a given electrical field intensity, compared to the meso-scale pump due to a combination of reduced voltage and current. However, at the same time the heat transport capacity was also reduced because of the lower flow rate generation for the micro-scale pump. In order to improve the performance, additional

electrode pairs could be added. However, there would be a tradeoff, as this would increase the pumping channel length and hence pressure drop. The results of these tests demonstrated that EHD conduction pumps could be fabricated and tested successfully in small scales and laid the foundation for future electrically driven micro-scale heat transport devices.

Additional experimental research in single-phase EHD conduction pumping has been done by Mahmoudi et al. [32]. They have developed a single-stage axisymmetric conduction micro-pump in a vertical configuration. Electrodes were patterned on commercial LCP substrates with 30 μm copper cladding and final spacing between electrodes was 286 μm. The overall size of their device was 50 x 70 x 5 mm. Static pressure generation was measured for 3 dielectric liquids: 10-GBN Nynas and Shell Diala AX transformer oils and N-hexane. The applied voltage ranged from 300-1500VDC, and a maximum of 100 Pa pressure generation was achieved at 1500 V. Along with the experimental measurement, a numerical simulation was also conducted in the same manner as described in the previous section. A comparison between numerical and experimental results showed good agreement. A schematic of the micro-pump is shown below in Figure 12, along with a sample of results in Figure 13.

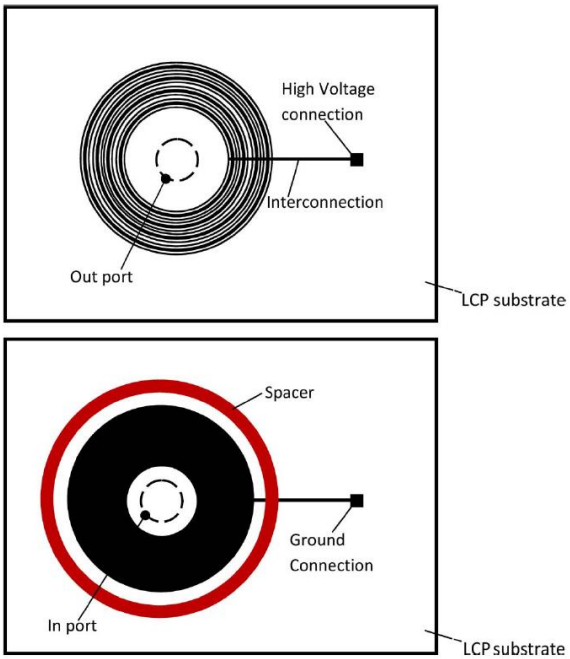

Figure 12: EHD conduction micro-pump design of Mahmoudi et al. [32]

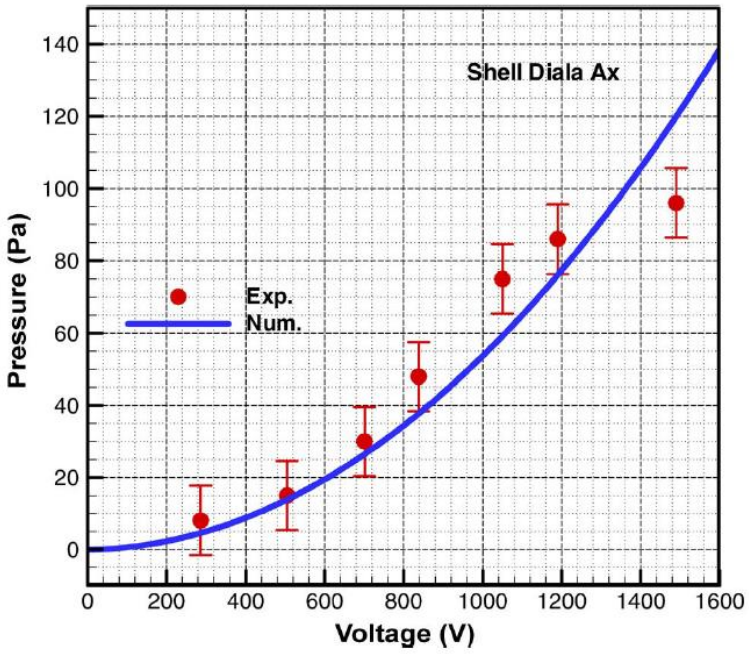

Figure 13: Comparison between numerical and experimental results of pressure generation for Mahmoudi et al. [32]

The important result obtained was that the minimum voltage required for initiating EHD conduction was 300V for this micro-pump design which was one order of magnitude lower than typical macro-scale pumps previously developed. Numerical prediction was accurate except at the highest voltage and this was believed to be caused by the reversed pressure generation due to the initiation of the direct ion injection at the corresponding field strength threshold predicted by the theory.

Although there is ongoing research in single-phase EHD conduction pumping with a wealth of measurement data such as pressure and flow rate, efforts to understand underlying fluid physics are also being pursued, such as the work of Gharraei et al. [33] and Hemayatkhah et al. [34]. In particular, the latter involved flow visualization of flush electrode design EHD conduction pump in macro-scale. The objective was to use visualization to understand the hydrodynamic behavior of such pumps. The design was similar to the numerical domain shown in Figure 3 with a narrow ground electrode and adjacent wide high voltage electrode. Various electrode dimensions and spacings were investigated (both symmetric and asymmetric) with width ratios between electrodes ranging from 1-5. The working fluid was silicon oil with electrical conductivity of 14×10^{-13} S/m and dielectric constant of 2.76. They identified two major factors that affected the pump functionality and these were the ion mobility (which was different for the positive and negative ions) and the electrode configuration. The results of the visualization study for six electrode pairs with 12 kV applied potential are shown in Figure 14.

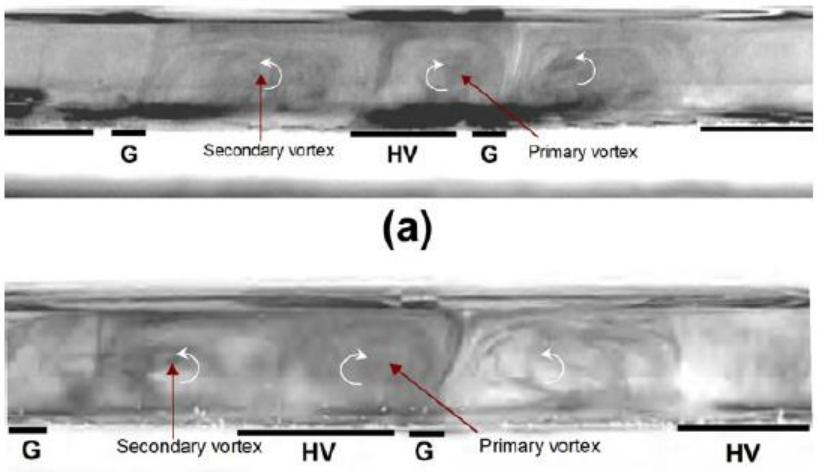

Figure 14: Flow pattern for six asymmetric electrode pairs by Hemayatkhah et al. [34]

The results show that for one set of electrodes, a primary vortex was generated which arrived from the rotational part of the Coulomb force. For more than one pair, secondary vortices were formed from the primary vortex. The results are interesting as they compare well to the numerical predictions described above in [19], even though the working fluid is different.

Other experimental research in single-phase EHD conduction pumping has also been performed by Hanaoka et al. [35-37] and references therein. In the more recent work in [37], they studied a macro-scale EHD conduction pump with a combination of rod-to-rod and meshy parallel plate electrode assemblies arranged in series. The working fluid was dihydrodecafluoropenten HFC43-10. The primary objective of the study was to describe the performance of the EHD pump through measurement of pressure head, current, power consumption and flow rate. In addition to this, they also determined flow patterns with the laser-schlieren technique. A maximum of 9 pairs of rod-to-rod and meshy parallel plate electrode assemblies were used. One of the most important aspects of the study was measurement of the potential distribution between electrodes, shown in Figure 15.

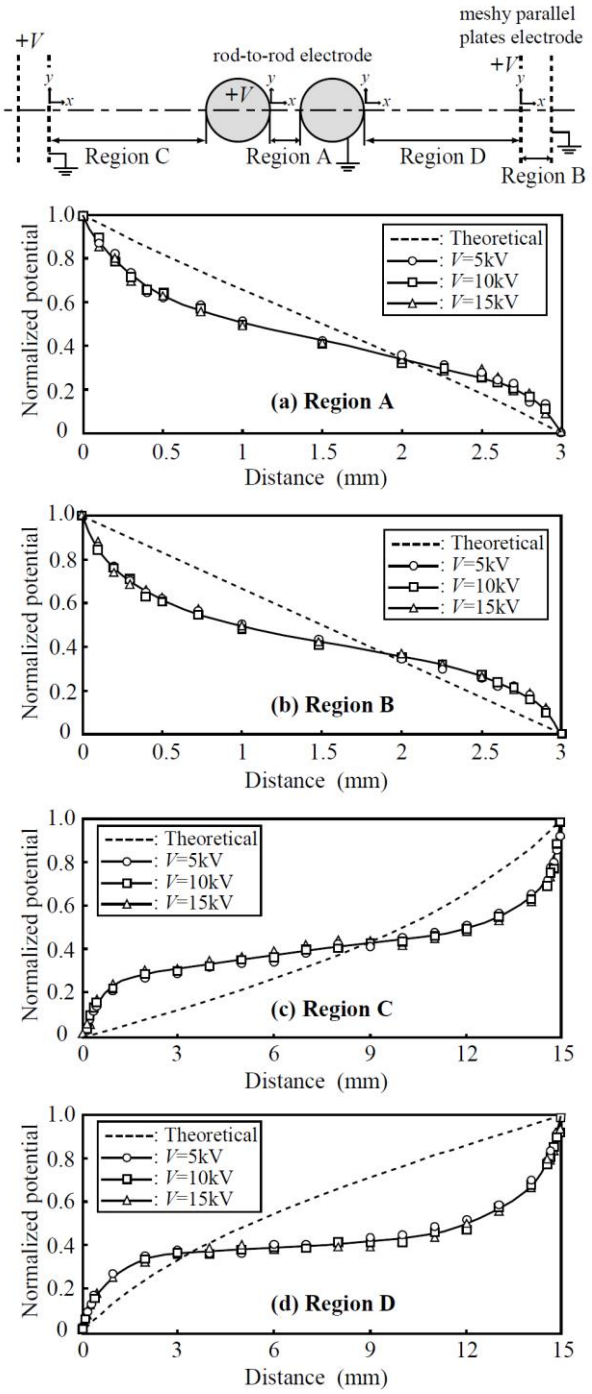

Figure 15: Potential distributions measured between EHD pump electrodes and comparison to theory by Hanaoka et al. [37]

The reason was that the electric field was distorted by the presence of the heterocharge layers in the vicinity of electrodes. Measurement of the potential distribution using a point sensor

(electrostatic probe) and surface potential meter showed that it broke from well-known distributions with symmetric or uniform shapes because of the space charge effect, as shown in Figure 15. Hanaoka et al. noticed the significant reinforcement of the electric field around the anode. They suggested that the imbalance of potential distribution near the anode and cathode was due to a mismatch of mobility between positive and negative ions. They determined that the working fluid (and halogenated liquids in general) contained molecules with a tendency to easily form negative ions and ionic species with different masses. If the negative ions had a larger mobility compared to the positive ions, they would gather in the vicinity of the anode more readily to produce the predominant space charge.

As mentioned above, pressure head and flow rate were also measured. The maximum pressure generated was 23.5 kPa at applied potential of 18 kV and power consumption of 7.2W. The maximum flow rate at this applied potential was 5.5 L/min and the pump efficiency was 32%. The time-dependent pressure generation and flow rate were also found in order to distinguish the results between the two electrode configurations (rod-to-rod vs. meshy parallel plate electrode assembly), along with typical EHD flow patterns in the form of a jet and fountain. These details are in [37].

1.1.5 Recent flow boiling experimental work in EHD conduction

Macro-scale experimental research in two-phase flow (flow boiling) heat transport systems driven by EHD conduction pumping has been previously conducted and select work can be found in [38-41]. More recently, as with the single-phase experiments, the focus has shifted from macro-scale to meso- and micro-scale. Following the results in [31], Pearson and Seyed-Yagoobi extended that work to include liquid-vapor phase change as a means to significantly enhance the heat transport capability of the system [42]. They studied flow boiling of HCFC-123

in rectangular micro-channels with EHD electrodes embedded into the channel walls. For a given flow rate, two-phase flow generally has higher heat transfer coefficients than single-phase liquid flow. However, heat transfer coefficient, dominant heat transfer mechanism and two-phase flow pressure drop are extremely difficult to predict via analytical or numerical solution. Although correlations exist for macro-scale flow boiling, they cannot often be applied in micro-scale without large errors. For these reasons, experiments were conducted to gain an understanding of these phenomena when an EHD conduction pump was used as a driving mechanism for the heat transport system. The reverse effect that two-phase flow had on EHD conduction pump performance was also quantified. Two pumps were studied: an adiabatic pump which was used to drive liquid in the loop and a downstream diabatic pump which was integrated together with the evaporator. The diabatic pump/evaporator was followed by a condenser which fed into the inlet of the adiabatic pump, completing the loop. The rectangular channel design and electrode dimensions are given in Figure 16 and Table II, respectively.

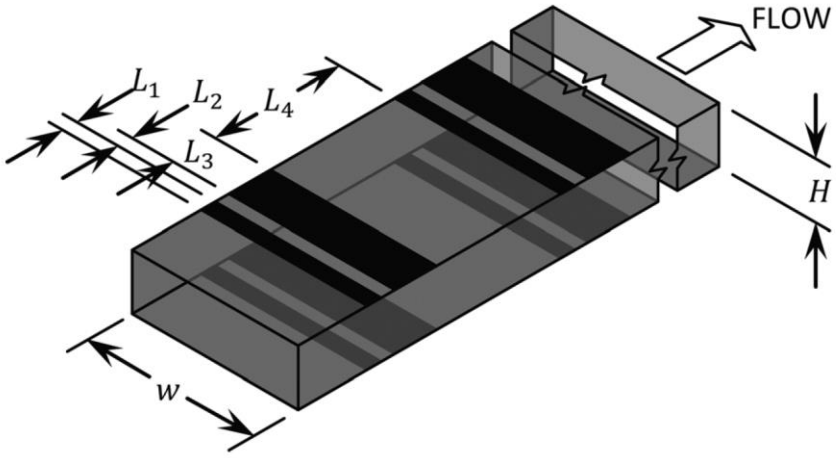

Figure 16: EHD conduction pump design showing flush electrodes embedded into rectangular pumping channel by Pearson and Seyed-Yagoobi [42]

Table II: EHD pump dimensions corresponding to Figure 16

Dimension	Short, diabatic design	Long, adiabatic design
w (mm)	12.7	12.7
H (μm)	508	508
L_1 (μm)	127	127
L_2 (μm)	127	127
L_3 (μm)	381	381
L_4 (mm)	1.27	1.27
Inlet/outlet center-to-center distance, L_{cc} (mm)	28.6	45.3
Heated length, L_h (mm)	22.2	39.0
Number of Electrode Pairs	13	21

For these experiments, new materials were used with a thick-film fabrication technique to make the EHD conduction pumps as compact as possible. The EHD electrodes (Pd-Ag was used as the electrode trace material) were printed onto a ceramic substrate along with an electric resistance heater and thermistors for surface temperature measurement. The heaters, insulating layers and thermistors were all printed using special resistive ink. Two substrates were sandwiched together with a PTFE gasket to form the rectangular flow channel with inlet/outlet holes.

The pumps were installed into a two-phase loop to study their performance. A fixed potential was applied to the EHD electrodes in the adiabatic pump which resulted in liquid flow through the loop. The heater on the diabatic pump was then activated and heat flux was incremented, which caused flow boiling to occur in the diabatic pump channel. This meant that

there was a liquid/vapor mixture in the channel. Tests were run with and without applied potential to the diabatic pump EHD electrodes and these are labeled as “Baseline” and “EHD Enhanced” in the results that follow. As the heat flux was increased, the rate of boiling increased, which caused more of the diabatic pump channel to fill with vapor rather than liquid. EHD conduction was only effective at pumping the liquid-phase which meant that the flow regime and void fraction played an important role in the performance of the diabatic EHD pump. Figure 17 shows the effect of the applied heat flux on the flow rate of the two-phase loop and the influence of EHD conduction in the diabatic pump.

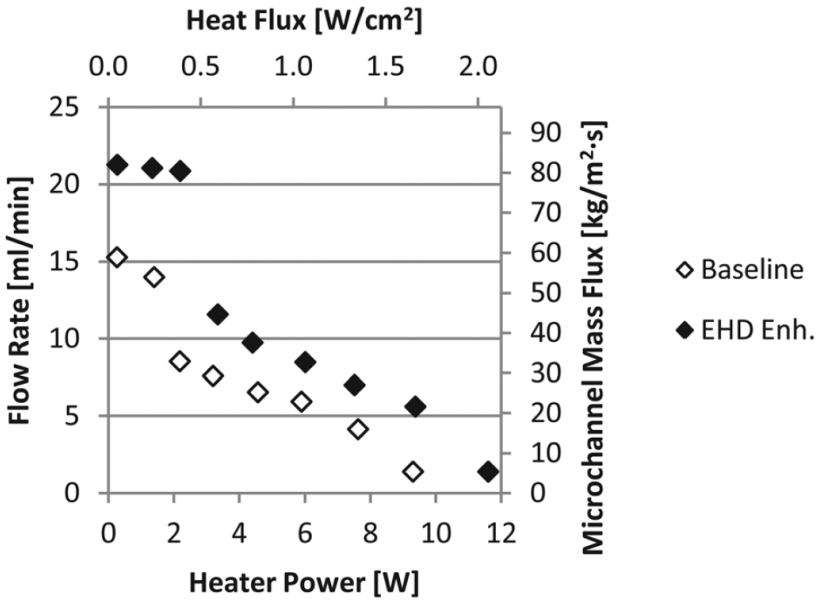

Figure 17: Effect of heat flux on flow rate in two-phase loop at fixed applied potential to EHD electrodes (750V) in [42]

From the above figure we see that there was a 40% increase in the flow rate at low heat fluxes when potential was applied to the EHD electrodes in the diabatic pump. The reason was that the pressure being generated by EHD conduction phenomenon balanced the two-phase flow pressure losses occurring in the evaporator. However, there was a sudden drop when boiling was

initiated and this can be seen clearly in the figure. As stated above, boiling proceeded and void fraction increased which meant that a large fraction of the volume in the pump channel contained vapor. The EHD conduction pump could not function as effectively as it would have with 100% liquid and the performance was degraded. This was also apparent in the evaporator pressure drop measurement, shown in Figure 18.

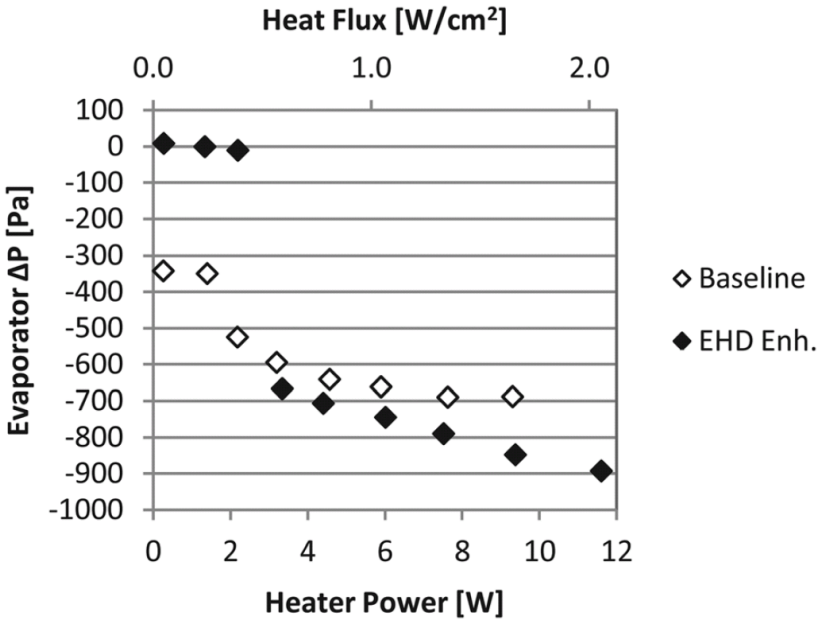

Figure 18: Effect of heat flux on evaporator pressure drop in two-phase loop at fixed applied potential to EHD electrodes (750V) in [42]

We see that the evaporator pressure drop measurements were coupled with flow rate measurements in Figure 17. These results were important because they showed that at low heat fluxes, the EHD conduction mechanism was able to enhance two-phase flow heat transport. However, as heat flux increased the effect was severely diminished, because the technique was only suitable for pumping of liquid. The experimental work demonstrated that many factors must be accounted for in an EHD conduction-driven micro-scale two-phase flow system.

1.2 Enhancement of boiling heat transfer using electrohydrodynamic conduction pumping

1.2.1 Pool boiling and liquid film flow boiling

In addition to flow boiling, pool boiling is another important heat transfer technique. In pool boiling, the working fluid is kept in a chamber with a heat source at the bottom. The heater surface is directly wet by the liquid. Nucleate boiling occurs above a certain heat flux when vapor bubbles form on the heater surface and depart into the pool of liquid due to buoyancy forces. The motion of bubbles and liquid above the heater surface both result in very effective heat transport. As heat flux is increased, the rate of vapor bubble formation becomes very high and liquid from the heater surroundings is unable to wet the surface. At this point the heater surface dries out and heat transfer is severely diminished; the surface temperature rises rapidly as a result. This is known as the Critical Heat Flux (CHF) condition and represents the limit of pool boiling heat transfer.

On the other hand, liquid film flow boiling is a heat transfer technique which is similar to pool boiling, with the following two major differences: (a.) the height of the liquid-vapor interface above the heater surface is significantly reduced (on the order of 2 mm in most of the experiments conducted here) in liquid film flow boiling, compared to pool boiling and (b.) the liquid film is pumped toward the heated surface. It should not be confused with so-called film boiling, which refers to vapor blanket formation over the heater surface at very high heat flux levels exceeding the critical heat flux during pool boiling. In the presence of gravity, liquid film flow boiling is facilitated by the hydrostatic pressure of the liquid. Conservation of mass requires that as liquid film vaporizes on the heater surface, fresh liquid from the surroundings is forced to take its place. Hydrostatic pressure results due to the difference in height between the liquid film at the periphery of the heater and the center, which causes fluid motion toward the center.

The liquid film flow boiling process results in much higher heat transfer coefficients compared to heat transfer only by natural convection above the heater surface. Although natural convection is initially the dominant heat transfer mechanism at low heat flux levels, nucleate boiling begins soon thereafter, as heat flux is increased. Vapor bubbles form at various sites on the heater surface and are driven upward from the horizontal surface by buoyancy forces. As the frequency of bubble formation and departure increases with increasing heat flux, upward motion of bubbles causes a corresponding downward motion of liquid. This violent mixing process dramatically increases the heat transfer coefficient.

As will be described in later chapters, the liquid film boiling experiment developed in the current work was made of a disc with a heat source at its center. Lithographically printed electrodes on the disc surface made up the conduction pump. When a voltage was applied to the electrodes, the film of liquid was pumped toward the center. As the liquid boiled off the heater surface, the vapor moved toward the outer periphery of the disc where it condensed. The freshly condensed liquid was pumped toward the heater, completing the loop. This created a compact radial heat transport device, with the boiler, adiabatic and condenser sections occupying a small physical space, as shown below in Figure 19. In the absence of gravity, the pumped liquid film also acted to repel bubbles formed on the heater surface. The liquid film inertia generated by the EHD conduction pumping was at least an order of magnitude higher than the force required to repel the bubbles away from the heated surface in the absence of gravity.

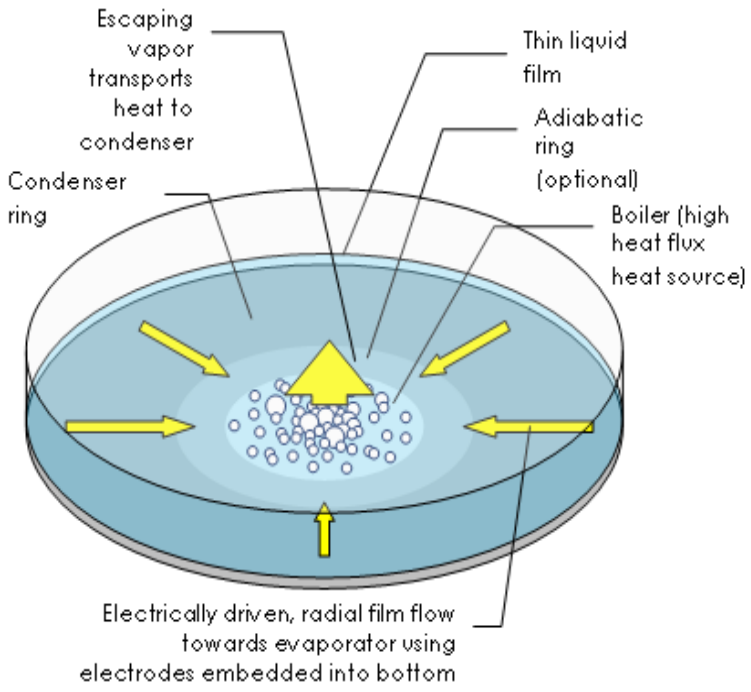

Figure 19: EHD-driven liquid film boiling conceptual schematic

For a film of liquid, the hydrostatic pressure is found by $\Delta P=\rho gh$, where ρ is liquid density, g is gravitational acceleration and h is the height of liquid film. For the 2.0 mm liquid film in this work and with the liquid density of the working fluid considered, the hydrostatic pressure is on the order of 30 Pa. Using a simple energy balance and thermodynamic properties of the fluid, the mass flow rate necessary for heat removal can also be found using

$$\dot{m} = \frac{q_{total}}{h_{fg}} \tag{24}$$

where $\dot{m}$ is the mass flow rate, q_{total} is the total heat removal and h_{fg} is the latent heat of vaporization for the working fluid. Typical values of heat removal are on the order of 25W for the systems considered in this work. Using the latent heat value of the working fluid, the required mass flow rate for this work is approximately 0.15 g/s. Therefore, during the liquid film boiling

process, the above flow rate must be maintained by only the hydrostatic pressure present in the liquid film.

As mentioned above, the critical heat flux is an undesirable condition. The heater surface dryout phenomenon occurs, as illustrated below in Figure 20 and efforts to delay or extend it in liquid film flow boiling must be made.

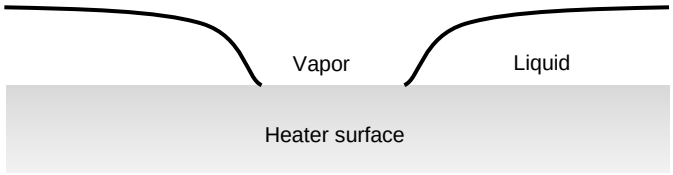

Figure 20: Heater dryout at critical heat flux during liquid film flow boiling

Heater surface dryout leads to very high surface temperatures and failure of the system being cooled, as the thermal management system can no longer adequately transport heat. It is important for any system to be able to extend or delay the CHF condition in order to continue operation. Enhancing heat transfer in order to delay CHF or reduce wall superheat is a very important area of research. One of the most unique and innovative ways to achieve this is by using EHD conduction pumping and this is discussed next.

1.2.2 Terrestrial work in pool boiling and liquid film flow boiling

Pearson and Seyed-Yagoobi [43] studied EHD conduction pumping as a possible technique to re-wet the heater surface during pool boiling by pumping liquid from the surroundings at heat fluxes close to CHF. They did this by embedding EHD electrodes directly into the heater surface and applying potential to them; the introduction of fresh cool liquid from the surroundings allowed the heat transfer coefficient to remain high and this extended the

maximum heat flux. In order to determine the effect of the applied electrical field on the complex boiling phenomena, two heaters were designed with EHD electrodes lithographically printed onto the boiling surface. The dimensions of the electrodes were based on numerical simulations. The driving factor was the minimum liquid flow rate that would be required via EHD conduction pumping to re-wet the heater surface at the maximum heat flux. This had to match the expected rate of vaporization. The electrodes were designed accordingly and details are shown in Figure 21 and Table III. Design A had larger electrode sizes and spacing which meant that less electrode pairs could be fitted on the 25.4 x 25.4 mm heater surface. The electrode dimensions for design B were the smallest that were possible with the thick-film fabrication technique used.

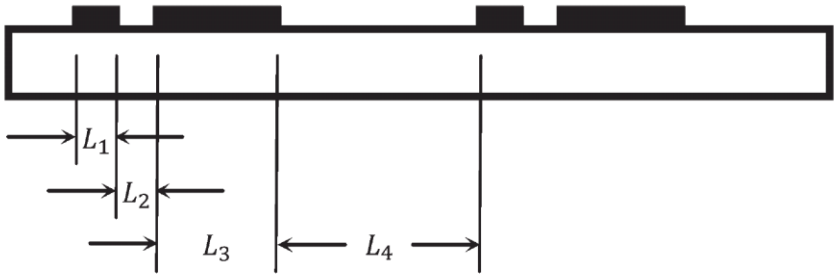

Figure 21: Pool boiling surface with embedded EHD electrodes by Pearson and Seyed-Yagoobi [43]

Table III: EHD electrode design dimensions corresponding to Figure 21

Dimension	Design A	Design B
L1 (μm)	254	127
L2 (μm)	254	127
L3 (μm)	762	381
L4 (mm)	2.268	1.143
Number of electrode pairs	7	14

The heaters were placed into a specially designed boiling chamber that allowed the process to be visually observed. The experiments were begun at ambient conditions and heat flux was applied to the heater. Heater surface temperature and saturation temperature were measured as the heat flux was increased and boiling was initiated. Data were recorded at fixed intervals when steady-state conditions were reached. The heat flux was incremented until CHF was reached (this point was marked by a sudden and rapid increase in the heater temperature with only a small increase in the applied heat flux). The entire test was repeated with a potential applied to the EHD electrodes, to quantify the effect of EHD conduction pumping on pool boiling heat transfer. The pool boiling results for design A and design B are shown in Figure 22 and Figure 23, respectively. The surface superheat was simply the difference between the heater surface temperature and the saturation temperature being measured directly above the liquid pool.

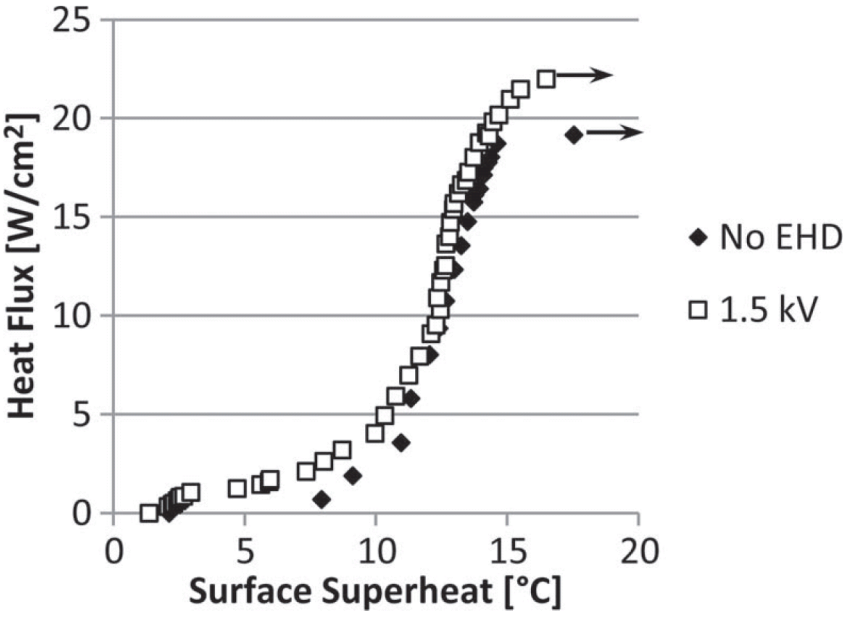

Figure 22: Pool boiling curve for heater design A in [43]

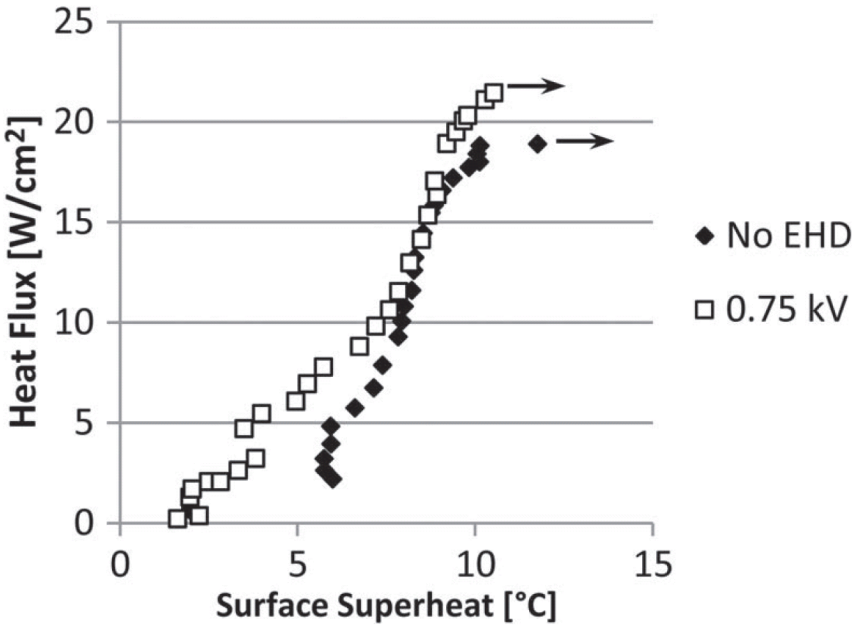

Figure 23: Pool boiling curve for heater design B in [43]

As we see from both figures above, the application of potential to the EHD electrodes in designs A and B resulted in approximately 15% increase in the maximum heat flux. The maximum potential applied to design A was 1.5 kV and for design B it was 0.75 kV. These were the safest applied potentials; there was a risk of ion injection or dielectric breakdown of either the HCFC-123 liquid or ceramic substrate if these potentials were exceeded.

At low heat flux we see that there was reduction in the surface superheat for both cases. Nucleate boiling had not yet been initiated at this point and natural convection was the dominant heat transfer mechanism in the no-EHD cases. Therefore the application of potential to EHD electrodes causes forced convection which improved heat transfer and lowered the heater surface temperature in the EHD cases. This effect was diminished as heat flux was increased because the formation of bubbles began. Liquid motion caused by bubble departure during nucleate boiling was much stronger than convective effects solely due to EHD conduction. However, as heat flux

was increased further, EHD conduction played a bigger role by helping to enhance wetting of the heater surface and as a result the CHF condition was delayed, as shown above.

In addition to the experimental work done, a brief analysis was also conducted. Hydrodynamic stability criteria have been used by many researchers to predict pool boiling critical heat flux. They considered jets of vapor perpendicular to a heater surface and determined that the instability of the liquid-vapor interface of these jets was often triggered at the same time the CHF condition was reached. The goal in [43] was to extend the classical stability analysis to account for the influence of an electrical body force term in the governing differential equations. A two-dimensional flow was considered. In a real conduction pumping system, the spatial variation of the electric body force is large, and at various positions, the force will have components in both the x- and z-directions. However, in this case since the net flow generation of the pump was in a direction parallel to the heated surface, only the x-direction of this force was considered, and the z-component was neglected. Furthermore, to simplify the analysis, the electric body force was considered to be a function only of z. The procedure followed a standard linear instability analysis, identical to that for deriving the Rayleigh–Taylor or Kelvin–Helmholtz instabilities, but with an additional term in the inviscid Euler equations for electric body force, $f_e(z)$.

For a nonzero EHD body force and interphase velocity (i.e. liquid or vapor phase is in motion), an expression was found for the most dangerous wavenumber in terms of the fluid properties and an unknown quantity $F_0(\alpha)/A$, where A was a constant and F_0 was dependent on the perturbed electric body force $f_e(z)$. An expression for $f_e(z)$ could not be determined from the governing equations of the instability analysis because the governing equations for the electric body force were not included. However, Pearson and Seyed-Yagoobi were still able to determine

the following influence, shown in Figure 24, of $F_0(\alpha)/A$ on the critical heat flux, based on assumed operating conditions. Based on the results below, they were able to conclude from an analytical standpoint that the electric body force did play an important role in enhancing CHF in pool boiling.

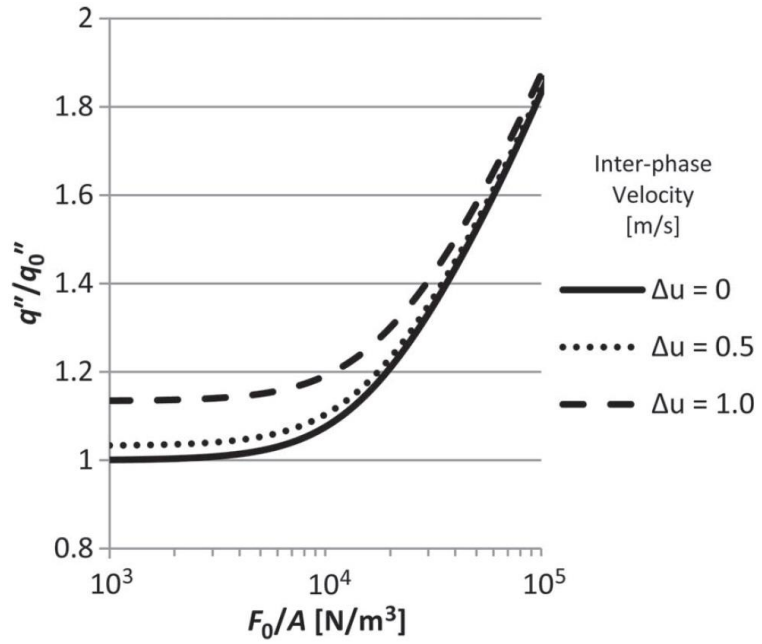

Figure 24: Influence of electric body force on critical heat flux – Result of hydrodynamic stability analysis in [43]

The study of EHD conduction-enhanced pool boiling led to further investigation of related phenomenon by Pearson and Seyed-Yagoobi, where they studied liquid film boiling of HCFC-123 in a radial heat transport device [44]. The objective remained to re-wet the heater surface using EHD conduction pumping to study the entire liquid film flow boiling regime and extend or delay CHF. However, in this case, the effects of applied potential and variation in liquid film thickness were studied, to quantify the influence of EHD conduction pumping on

liquid film boiling heat transfer. A high liquid flow rate was expected compared to the pool boiling experiments discussed above, since the EHD electrodes were printed on the surrounding condenser surface rather than the heater surface itself. As in the previous experiments, two electrode designs were fabricated. Only design A was used for the liquid film flow boiling experiments in [44]. However, since multiple electrode discs were fabricated and the design was robust, they were also used for all the liquid film flow boiling experiments presented in the current work as well. Design A was used for the combined EHD conduction and dielectrophoretic experiments of chapter 5 and Design B was used in the terrestrial and microgravity experiments of chapter 4. The design is shown in Figure 25 and dimensions are in Table IV.

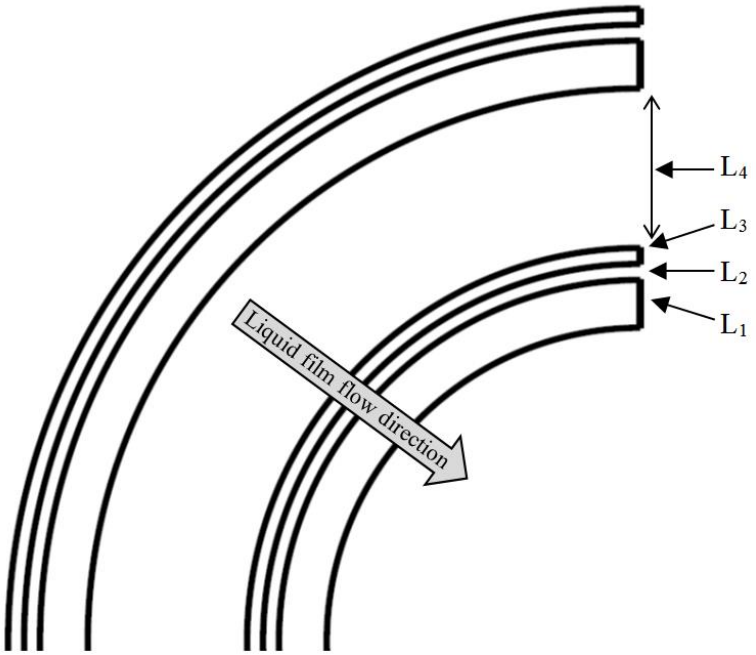

Figure 25: Condenser surface in liquid film flow boiling experiment with embedded EHD electrodes designed by Pearson and Seyed-Yagoobi [44]

Table IV: EHD electrode design dimensions corresponding to Figure 25

Dimension	Design A	Design B
L_1 (μm)	1520	762
L_2 (μm)	508	254
L_3 (μm)	508	254
L_4 (mm)	5.08	2.54
Number of electrode pairs	7	14

The heat transport disc was installed into a chamber which was sealed. Cooling water circulated through the bottom compartment of the chamber underneath the condenser and this was also used to maintain constant saturation conditions. The experiments began with a 2.0 mm liquid film at ambient conditions (2.0 mm was the optimum film thickness based on electrode dimensions from numerical simulation). The heat flux was incremented gradually and boiling was initiated on the heater surface. The heater surface temperature and saturation temperature were recorded at each heat flux level. The heat flux was increased until the CHF condition where a small increase caused the surface superheat or ΔT ($\Delta T = T_{heater\_surface} - T_{saturation}$) to increase rapidly. The entire test was repeated with an applied potential of 2 kV to the EHD electrodes. Tests with a liquid film thickness of 0.75 mm were also conducted with and without applied potential to the EHD electrodes and all results are given in Figure 26.

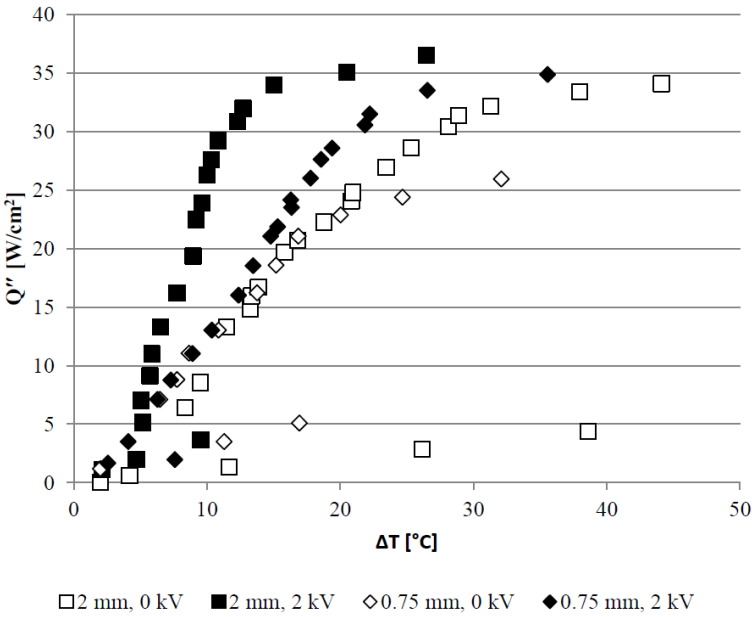

Figure 26: Results for liquid film boiling: effect of EHD conduction pumping on boiling curve for two film thicknesses in [44]

For the results of liquid film thickness of 2.0 mm, we see that although there was a modest enhancement in CHF (~7%), there was significant enhancement in ΔT (the temperature was reduced up to a factor of 2.5) when the EHD conduction pump was activated. This was attributed to local EHD-generated liquid circulation in the vicinity of the heater which allowed for cooler operation. The effect was diminished for the 0.75 mm liquid film thickness because dryout of the heater occurred prior to CHF and local instabilities prevented wetting of the surface with fresh liquid. However, the application of potential to the EHD electrodes still increased the maximum heat flux from 26 W/cm^2 to 35 W/cm^2 which was even higher than the no-EHD 2.0 mm liquid film thickness case. The experimental results demonstrated that EHD conduction pumping was able to enhance liquid film boiling heat transport and that the unique and innovate radial heat transport device was well-suited for future application in thermal control where space and power savings were a major design factor.

1.3 Enhancement of boiling heat transfer using dielectrophoresis

1.3.1 Dielectrophoresis

As described in the previous section, the normal ebullition cycle for pool boiling and liquid film flow boiling involves liquid heating, nucleation, bubble growth and release. This is a central mechanism of heat transfer driven primarily by buoyancy in earth gravity. However, the buoyancy forces are absent in microgravity and boiling processes cannot be used effectively for thermal management systems. One of the ways to overcome this limitation, as described above, is to introduce electrical force to overcome interfacial tension and facilitate bubble departure. While the method of EHD conduction-driven liquid film flow boiling has already been introduced, this section describes the use of the so-called dielectrophoretic (DEP) force (as indicated in Eq. (1)) for enhancement of boiling heat transfer. Dielectrophoresis is translational motion of neutral matter caused by polarization effects in a non-uniform electric field [45]. On the other hand, electrophoresis is motion caused by response to free charge on a body in a uniform or non-uniform electric field. The use of DEP to influence particle motion is well-known in life science research, where it is commonly used for separation or manipulation of cells etc. It can be also be used to exert forces on neutral particles or bubbles suspended in a liquid medium [46], which makes it especially suitable for boiling heat transfer enhancement. It is most readily observed for size range of 1-1000 μm which is the appropriate range of bubble diameters in the liquid film flow boiling experiments performed in these studies. When the bubbles or particles are in a strong non-uniform electric field, field-induced polarization occurs. This causes surface charge to be redistributed on opposite ends of the bubble or particle, as illustrated in Figure 27 [47]. In an AC field, when a neutral body is polarized, it is attracted to the strongest electric field, since force is proportional to electric field (as will be shown below). When the

field changes direction, the polarized body does not reverse direction, as shown in Figure 28 [47].

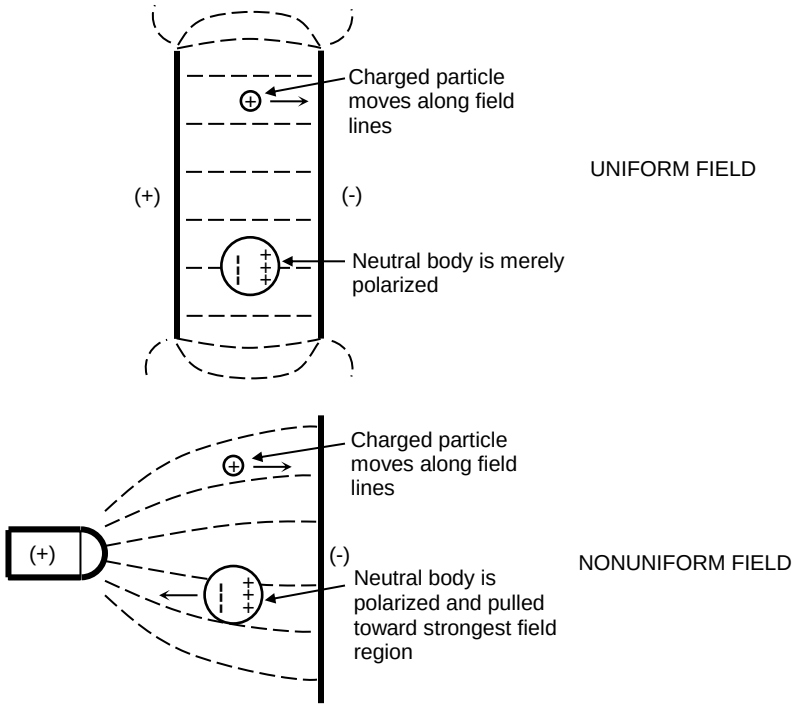

Figure 27: Electrophoresis and dielectrophoresis in uniform and non-uniform DC electric field

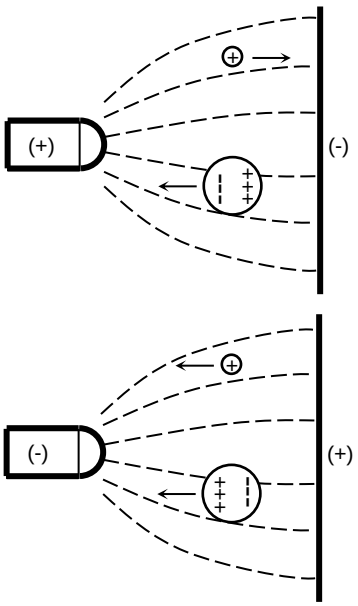

Figure 28: Electrophoresis and dielectrophoresis in non-uniform AC electric field

Before going further, a distinction must be made between ideal and real dielectrics. Ideal dielectrics have finite dielectric constant and infinite resistivity, while real dielectrics exhibit both polarization and conduction. To determine the dielectrophoretic force in ideal dielectrics, we consider the net electric force on a small body in an external electric field, $\boldsymbol{E_e}$. In this case, the small body is a dipole, which is a pair of positive and negative charges, q^+ and q^-, separated by distance $\boldsymbol{d}$. The location of the dipole is determined by the position vector $\boldsymbol{r}$.

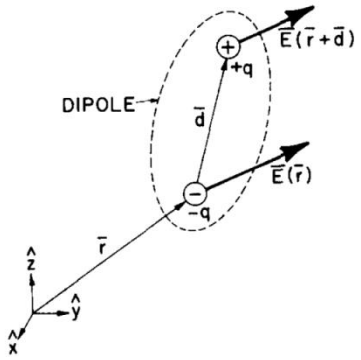

Figure 29: Forces acting on a dipole

In the figure above, the net electric force on the dipole is given by Eq. (25).

$$\boldsymbol{F} = q\boldsymbol{E}_e(\boldsymbol{r}+\boldsymbol{d}) - q\boldsymbol{E_e}(\boldsymbol{r}) \tag{25}$$

If we use a Taylor series expansion for the electric field and neglect higher order terms, we get

$$\boldsymbol{E}_e(\boldsymbol{r}+\boldsymbol{d}) = \boldsymbol{E}_e(\boldsymbol{r}) + \boldsymbol{d}\cdot\boldsymbol{\nabla}\boldsymbol{E}_e(\boldsymbol{r}) + \cdots \tag{26}$$

In addition to this, the dipole moment is defined as

$$\boldsymbol{p} = q\boldsymbol{d} \tag{27}$$

The dipole moment is the measure of the separation of the positive and negative charges. When we substitute Eqs. (26) and (27) into Eq. (25) the following expression is found

$$\boldsymbol{F} = (\boldsymbol{p} \cdot \boldsymbol{\nabla})\boldsymbol{E}_e \tag{28}$$

In addition to the dipole moment, the polarization density, $\boldsymbol{P}$, is also a useful quantity. It is the vector field that expresses the average dipole moment per unit volume, V and is given by $\boldsymbol{P}=\boldsymbol{p}/V$. In order to proceed, we need a relationship between the polarization density and external electric field. This is done by analyzing the relationship between the internal charge arrangement and charge on the electrodes in a dielectric. When matter interacts with an electric field, conduction and polarization occur. Conduction occurs when free charges move within the material, whereas polarization occurs when the motion of charges is blocked or bound in some way. Therefore the total charge is made up of free and bound charge. One way to understand these effects is to consider a parallel plate capacitor, as shown in Figure 30 [48].

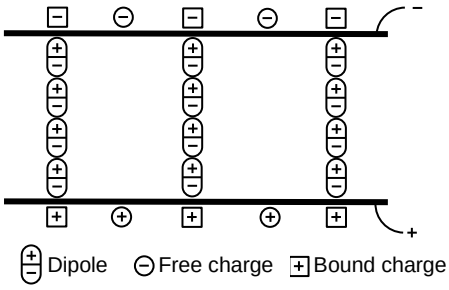

Figure 30: Free and bound charges in a parallel plate capacitor

If there is a vacuum between the plate electrodes, only the free charge comes into play (because the dipoles shown in the above figure would not be present). If any other material (dielectric) is added in the inter-electrode region, the existence of dipoles (whether induced or permanent) results in additional bound charges, which change the total charge at the electrodes. The effect of the bound charges are lumped together and defined as the polarization effects. For many

dielectric materials, there is a linear relationship between the external electric field and the polarization density [49]

$$\boldsymbol{P} = \varepsilon_0(\kappa - 1)\boldsymbol{E_e} \tag{29}$$

where κ is the dielectric constant of the material and ε_0 is the permittivity of a vacuum. To determine the net electric force on a spherical particle, for example, we first need to consider the case of an insulating sphere of radius a, placed in a uniform field in a dielectric liquid. The permittivity of the liquid is ε_1 and permittivity of the sphere is ε_2. Laplace's equation is solved for the potential inside and outside the sphere and the electric field can be found everywhere as a result, using Eq. (11). This is a classical solution and is widely available in any electrostatics textbook. From the solution, the electric field strength in the interior of the sphere, $\boldsymbol{E_i}$ is

$$\boldsymbol{E}_i = \frac{3\varepsilon_1}{\varepsilon_2 + 2\varepsilon_1}\boldsymbol{E_e} \tag{30}$$

For $\varepsilon_2 < \varepsilon_1$, it is smaller than the external electric field by

$$\boldsymbol{E_e} - \boldsymbol{E}_i = \frac{\varepsilon_2 - \varepsilon_1}{\varepsilon_2 + 2\varepsilon_1}\boldsymbol{E_e} \tag{31}$$

If we apply Eq. (29) to this particular case, the polarization density in the sphere can be found as a function of the internal electric field

$$\boldsymbol{P} = (\varepsilon_2 - \varepsilon_1)\boldsymbol{E_i} = (\varepsilon_2 - \varepsilon_1)\frac{3\varepsilon_1}{\varepsilon_2 + 2\varepsilon_1}\boldsymbol{E_e} \tag{32}$$

However, since this is the dipole moment per unit volume, the sphere acts to the outside with a dipole moment of

$$\boldsymbol{p} = V\boldsymbol{P} = \frac{4}{3}\pi a^3\boldsymbol{P} = 4\pi a^3\varepsilon_1\frac{\varepsilon_2 - \varepsilon_1}{\varepsilon_2 + 2\varepsilon_1}\boldsymbol{E_e} \tag{33}$$

Substituting Eq. (33) into Eq. (28) gives the net dielectrophoretic force [45]

$$\boldsymbol{F_{DEP}} = 2\pi a^3 \varepsilon_1 \left(\frac{\varepsilon_2 - \varepsilon_1}{\varepsilon_2 + 2\varepsilon_1}\right) \boldsymbol{\nabla} |\boldsymbol{E}_e|^2 \tag{34}$$

From the above equation, positive dielectrophoresis occurs when particles are attracted to regions of stronger electrical field when their permittivity exceeds that of suspension medium, $\varepsilon_2 > \varepsilon_1$ and negative dielectrophoresis occurs when particles are repelled from regions of stronger electrical fields when their permittivity is less than that of suspension medium, $\varepsilon_2 < \varepsilon_1$.

It is important to mention that in addition to bubble motion, the applied electric field can also deform liquid droplets or bubbles into prolate spheroids or elongate them in the direction of the electric field [46]. This changes the dipole moment given in Eq. (33) and as a result the net DEP force is changed as well. This also has a reciprocal effect of changing the electric field around the bubble. If the deformation is small, the motion of bubbles can be predicted with reasonable accuracy. However, if bubble deformation is significant, the effects must be included in the analysis. A pertinent example from the literature of previous studies in bubble deformation in a dielectric fluid in the presence of a non-uniform electric field is by Pearson and Seyed-Yagoobi [50]. They carried out a three-dimensional numerical study that modeled bubble deformation and calculated the net dielectrophoretic force exerted by the electric field on the bubble. They found that deformation can be significant especially within small-scale devices where bubble size is on the order of channel size or electrode spacing.

1.3.2 Terrestrial work in DEP-enhanced pool boiling

There are a variety of motivations for studying dielectrophoresis and its relationship to bubble motion and behavior. Although the main focus in the current work is DEP-enhanced nucleate boiling heat transfer, another area of importance is in superconductivity. Cryogenic

liquids such as liquid nitrogen (LN_2) are often used as coolants for superconductivity applications where they function as both the coolant and electrical insulator. However, bubbles can easily form in the liquid which can negatively affect electrical insulation level. For this reason, Wang et al. [51] studied bubbles in liquid nitrogen under a non-uniform electric field, in order to determine the influence on bubble motion and behavior. Liquid nitrogen has no appreciable free charges and the Coulomb force in Eq. (1) can be neglected. Since only free bubbles are considered, the electrostriction term in Eq. (1) is also neglected. This means that the dielectrophoresis term is the only important electric body force term. Wang et al. combined an experimental study of bubble motion (quantified using high-speed imaging) in a rod-plane gap with an analytical model that was also developed alongside. Figure 31 shows the rod-plane electrode configuration along with the forces acting on a given bubble that were analyzed. The rod electrode was made of copper and had a diameter of 1.5 mm and length of 270 mm. The plane electrode was a 2 mm thick sheet of aluminum with height of 270 mm and width of 72 mm. The spacing between electrodes, L, was 16 mm. Applied potentials in experiments ranged from -50 kV to +50 kV. A low-power heater beneath the rod-plane gap was used to produce a successive stream of bubbles at location x_i.

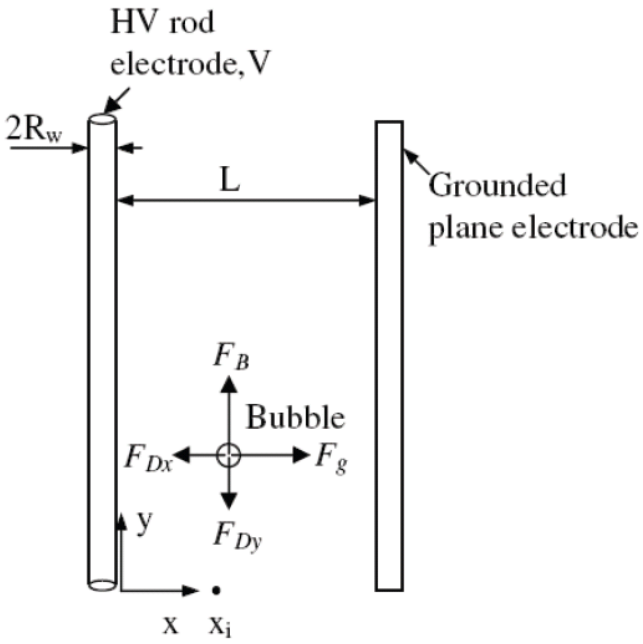

Figure 31: Electrode configuration and forces acting on a single bubble for experiments of Wang et al. [51]

The analytical model consisted of analyzing the bubble equation of motion to determine trajectory under the influence of the non-uniform electric field. Deformation of the bubble (which affects the DEP force) was neglected. From the figure above, $\boldsymbol{F_B}$ represents the buoyancy force acting on the bubble, $\boldsymbol{F_D}$ is the drag force and $\boldsymbol{F_g}$ is the electric gradient force, or in this case, simply the dielectrophoretic force given above in Eq. (34). The equation of bubble motion is given as

$$m_{eff}\dot{\boldsymbol{v}} = \boldsymbol{F_{DEP}} + \boldsymbol{F_{drag}} + \boldsymbol{F_{bouyancy}} \tag{35}$$

where m_{eff} is the effective mass of the bubble and $\dot{\boldsymbol{v}}$ is the acceleration of the bubble. The effective mass of the bubble is

$$m_{eff} = \frac{4}{3}\pi a^3 \left(\rho_v + \frac{\rho_l}{2}\right) \tag{36}$$

where a is the bubble radius, ρ_v is the vapor density and ρ_l is the liquid density. If the viscosity of the vapor phase is neglected, the drag force is given as

$$\boldsymbol{F_{drag}} = 4\pi\mu_l a\boldsymbol{v} \tag{37}$$

Finally, the buoyancy force is given as

$$\boldsymbol{F_{bouyancy}} = \frac{4}{3}\pi a^3(\rho_l - \rho_v)\boldsymbol{g} \tag{38}$$

where $\boldsymbol{g}$ is the acceleration due to gravity. From the above equations, the electric field intensity must be known to solve the equation of motion. For this rod-plane electrode configuration, Wang et al were able to determine the electric field intensity, E_e, as a function of the spatial variables, x and y. Taking the square and finding the gradient gave the $\nabla|\boldsymbol{E_e}|^2$ term in Eq. (34). Substituting this, along with Eqs. (36), (37) and (38) into Eq. (35) gave two equations of motion for the bubble in the x and y directions. Solving the corresponding differential equations resulted in the bubble trajectories which could be compared with the experimental results. A method to quantitatively study the effect of electric field on bubble motion was developed using an area map between the rod and plane electrode. Thus, the location on the plane electrode where the bubble collided (minimum collision height) could be pinpointed using the high-speed imaging during experiments and compared to the analytical prediction, as shown in Figure 32. The results showed that bubbles tended to move closer to the lower field region irrespective of electric field direction.

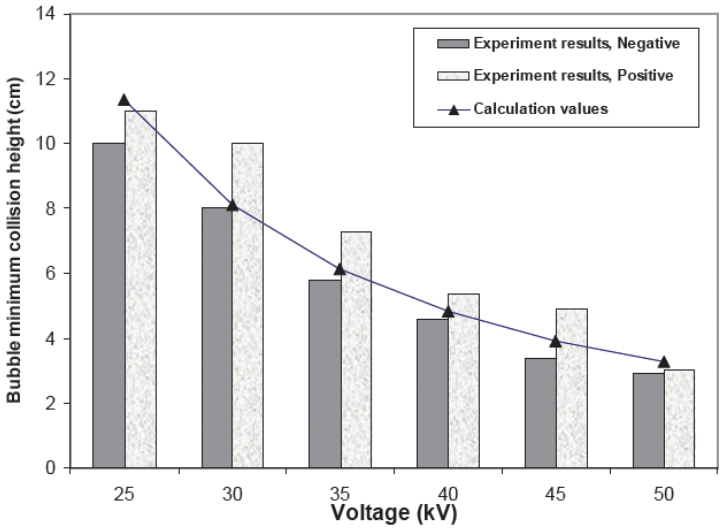

Figure 32: Comparison of minimum bubble collision height for theoretical and experimental results (x_i=5 mm for theory calculation) for Wang et al. [51]

The conclusions of the study were that the DC non-uniform electric field had an obvious effect on bubble behavior. The measured bubble trajectories were in reasonable agreement with predictions from the above model. The non-uniform field of negative polarity had a larger effect on bubble motion than one of positive polarity, possibly due to space charge formation in the liquid nitrogen as a result of charge injection from the electrodes. This in turn caused the electric field distribution to be distorted, increasing the local gradient force acting on adjacent bubbles.

The above work was one of many that clearly demonstrated the effect of a strong non-uniform electric field on bubble dynamics in a dielectric liquid. For this reason, the use of DEP forces to enhance pool boiling heat transfer has been studied for some time, including earlier efforts by Seyed-Yagoobi et al. [52, 53]. More recently, Kweon and Kim [54] studied the use of a non-uniform electric field to enhance nucleate boiling heat transfer. In their experimental study of saturated pool boiling in the presence of a non-uniform DC electric field, a plate-wire electrode configuration was used with Freon-113 as the working fluid. High speed imaging was used to measure boiling parameters. The results showed that there was a shift in the boiling curve

and a delay in the onset of nucleate boiling (ONB) and critical heat flux (CHF) to higher values, as shown in Figure 33.

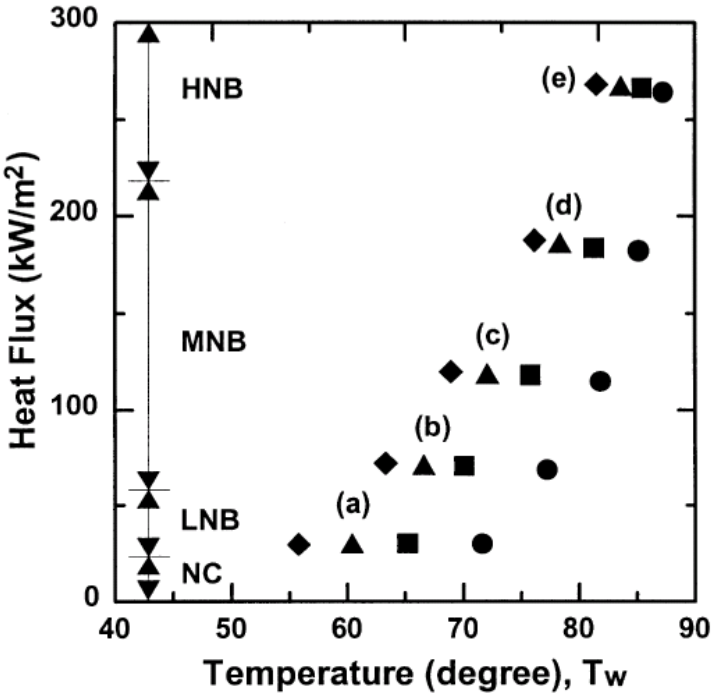

Figure 33: EHD pool boiling curves of a wire in a non-uniform dc electric field by Kweon and Kim [54] (● 0 kV, ■ 5 kV, ▲ 10 kV, ♦ 15 kV)

NC was the natural convection regime. LNB, MNB and HNB were the low, moderate and high nucleate boiling regimes, respectively. For a given heat flux, the relative heat transfer coefficient increased with increasing applied voltage. For example, At 15 kV DC voltage, the heat transfer coefficient was enhanced about 215% for (a.) 29 kW/m^2, 127% for (b.) 69 kW/m^2, 81% for (c.) 115 kW/m^2, 54% for (d.) 183 kW/m^2 and 32% for (e.) 265 kW/m^2. The sensitivity of nucleate boiling heat transfer to an electric field was more effective at lower heat fluxes.

In addition to enhancement in the pool boiling curve, Kweon and Kim also confirmed that the mechanism of EHD nucleate boiling was closely connected to the dynamic behavior of bubbles, such as bubble velocity, frequency and diameter. They found that, for example, At 20

kV DC voltage, the average bubble velocity increased about 5 times greater than that of the zero field case and the average bubble frequency increased about 14 times. Velocities of bubbles departing on the wire were faster than bubbles in the bulk liquid due to the strong electric field concentration near the wire. It was found that bubble departure away from the lower side of the wire stopped at a certain distance which increased with increasing the applied voltage. The bubble diameter at the moment of detachment was predicted by considering a balance between buoyancy, surface tension and electric forces acting on the bubble (similar to the previous study). These were compared to experimental measurements and showed generally good agreement. They found that bubble diameter decreased as the applied voltage increased because the electric force acting on bubbles increased (by increasing the electric field). The overall conclusions of the study were that the non-uniform electric field strongly affected bubble dynamics and was responsible for enhanced heat transfer. The relative contribution of latent heat to boiling heat transfer in electric field was also introduced and they found that at very high voltage, the amount of latent heat transported by the bubbles nearly corresponded to the total heat flux.

Further research in the use of non-uniform electric fields for nucleate boiling and critical heat flux enhancement was conducted by Hristov et al. [55]. An experimental and theoretical study was performed in pool boiling of HCFC-123 on a horizontal surface with two electrode designs (parallel rods and wire mesh). Experimental data were compared to similar results by other researchers with differences in heater surface finishes and electrode design. The data indicated that heat transfer coefficient and critical heat flux were enhanced by the DC electric field. The parallel rod electrodes created a more non-uniform electric field while the mesh electrodes created a uniform electric field but obstructed vapor bubbles during nucleate boiling. At the highest electric field strength of 5 MV/m, there was a large non-linear increase in the heat

transfer coefficient for the rod electrode design and this was attributed to greater density in small nucleation sites on the smooth heater surface.

A hydrodynamic model was developed to predict the critical heat flux with electric field enhancement. The extended model was not successful in reconciling the differences between experimental data from two studies. Some of the issues warranted further investigation, such as the effect of the detached bubbles on the distortion of the electric field at the heated wall by the bubbles themselves and variation in electrical properties of the working fluids due to impurities. A theoretical model was also developed for the growth of a single vapor bubble on a superheated wall in an electric field. It included matching of models for micro- and macro- regions, conduction in the wall, distortion of electric field inside and outside the bubble, temperature dependence on electrical properties and free charge generation. The model development led to a numerical simulation based on the level-set method. The results of the numerical simulation provided preliminary solutions for bubble detachment and evolution of dry spots on the heater surface with and without the electric field.

More recently, Kano et al. [56] have studied nucleate boiling enhanced by a local non-uniform electric field. The working fluid was HFE-7100 and the heater surface was made of copper. The micro-scale electrode was designed to allow for liquid convection and inflow (via EHD conduction) at low superheat values, and attraction of bubbles (via dielectrophoresis) at high superheat values. The pool boiling experiments were conducted for electrode heights of 100, 200 and 300 μm above the heater surface. The maximum critical heat flux value of all experiments was 47 W/cm^2 at electric field strength of -5 kV/mm and occurred at electrode height of 300 μm. The heat transfer coefficient was 14 $kW/m^2 \cdot K$ at these operating conditions. The CHF value was three times higher than the maximum CHF for the no-electric field case.

In addition to the pool boiling curves, bubble behavior was also observed above the electrode and heater surface using a transparent Indium Tin Oxide (ITO) -coated electrode. The imaging results suggested that the electric field effects induced Kelvin-Helmholz type instabilities which divided larger bubbles into smaller ones. The visualizations were also used to make the argument that the increased heat fluxes were due to periodic thin film creation by the electric field at the bubble lower interfaces which strongly enhanced the heat transfer. In addition to the experimental work, Kano et al. also considered the classical Kelvin-Helmholz instability analysis on the liquid-vapor inteface by modifying it to include EHD effects. The ratio of critical heat flux with and without electric field was predicted by the frequency ratio of the thin film in the gap between the boiling surface and electrode; details of the analysis are in [56].

1.3.3 Microgravity work in DEP-enhanced pool boiling

Although extensive terrestrial studies have been conducted, there has also been substantial work in micro-gravity pool boiling using the DEP force (it is important to mention that this is different than electro-wetting of the heater surface during liquid film flow boiling in microgravity described above, which as far as the author is aware, has not been investigated in the literature). Micro-gravity conditions can be achieved by different means, such as drop towers, sounding rockets, parabolic flights, unmanned orbital flights and in orbiting labs such as the International Space Station (ISS). Drop towers have low cost but only offer a few seconds of micro-gravity. Sounding rockets can provide up to 5 min of low quality micro-gravity but are not suitable, for example, if a large number of tests must be conducted. Orbital testing provides consistent, high-quality micro-gravity but is the costliest option. Parabolic flights are suitable compromise, with up to 25 seconds of micro-gravity per parabola (typically up to 40 parabolas

per flight) with relatively low cost. Limited research in the use of electrical fields to influence boiling behavior in micro-gravity has been conducted and a sampling of these is discussed next.

The motivation behind previous studies was that heat transport could be improved in micro-gravity if the local non-uniform electrical field was used to move vapor bubbles away from the heater surface where they formed during nucleate boiling. To demonstrate this and also determine the effect of an electric field on bubble dynamics in a micro-gravity environment, Herman et al. [57] conducted parabolic flight experiments which included high-speed visualization of bubble departure, detachment characteristics and volume measurement. This was part of a comprehensive study of heat transfer in pool boiling under the influence of an electric field. However, due to the complexity of direct studies in nucleate boiling, bubbles were generated by injecting air into the working fluid (PF5052 dielectric liquid) through an orifice in a plane surface. The plane surface also acted as a ground electrode, and an additional high-voltage electrode was mounted above. In the micro-gravity environment in the absence of electric field, a variety of bubble behaviors were observed such as gas-liquid interface instability on the surface of the bubble, bubbles which remained attached to the surface (and had increased volume) and also regular detachment. When the electric field was activated, they observed that bubble detachment occurred easily. The volume was decreased at detachment and bubbles were also elongated in the direction of the field.

Similar observations of bubble dynamics were also made in two separate nucleate boiling experiments in continuous micro-gravity environment on board the ISS, in recent investigations by Dhir et al. [58] and Raj et al. [59] (influence of electric field was not studied in either experiment). Both groups used the same apparatus (Boiling eXperiment Facility or BXF) and working fluid (Perfluoro-n-hexane) but utilized different heater configurations. Dhir et al.

studied single and multiple bubbles during nucleate boiling of FC-72 from a circular flat heater with etched artificial cavities. They found that single bubbles tended not to depart from the surface and lateral merger of small bubbles led to growth of a single large bubble at low wall superheat. This was also observed at higher superheat during nucleate boiling, where the large bubble lifted off but hovered and remained directly above the surface. They used the experimental results to support the development of a mechanistic model for nucleate boiling heat transfer in a micro-gravity environment. On the other hand, Raj et al. used two flat, semitransparent micro-heater arrays for their experiments. The arrays were made up of 96 individually controlled platinum resistance heaters, which allowed the heater size to be varied. The effects of gravity, heater size, superheat, subcooling, and pressure on pool boiling heat transfer were studied. This culminated in the development of a unified framework that scaled microgravity pool boiling heat flux with gravity level and heater size. The robust scaling framework was used to explain important trends in the boiling literature.

Additional research in the influence of an electrical field on pool boiling heat transfer in micro-gravity was done by, among others, Snyder and Chung [60]. They performed pool boiling experiments of FC-72 from a 25.4 x 25.4 mm square heater surface in a drop tower. The boiling chamber and attachments (sensors, high-speed camera) were released in the drop tower which provided 2.1 seconds of micro-gravity. They coupled temperature/heat flux measurements with high-speed visualization (which was used to measure average bubble diameter). They also tested three DEP electrode geometries above the heater surface (flat plate, diverging plate and pin electrode) with varying applied potential. The heater surface was grounded and potential was applied to the electrode mounted directly above, resulting in a non-uniform electrical field in the vicinity of the boiling surface. At a heat flux of 3.9 W/cm2 with no electrical field, vapor bubbles

from the heater coalesced into a large bubble with an average diameter of 73 mm in micro-gravity. At the same heat flux with an applied potential of 16 kV to the pin electrode, the average bubble diameter was reduced to 1.3 mm and the superheat (i.e. ΔT between heater surface and bulk liquid) decreased by 10°C. For the diverging plate electrode, also at the same heat flux and applied potential, the average bubble diameter was 0.95 mm and the superheat decreased by 15°C. Thus, they were able to conclude that specific electrode geometries may be developed in order to maximize the effectiveness of the electric field in micro-gravity.

More recently, Di Marco and Grassi [61] conducted experiments in micro-gravity on board the unmanned orbital Foton-M2 spacecraft organized by the European Space Agency. They also studied the effect of DEP force during pool boiling of FC-72 from a 20 x 20 mm square heater surface. Five equally spaced parallel rod electrodes (made of stainless steel, 1 mm in diameter and 5 mm above the heater surface) were used. The highest applied potential to the electrodes was 10 kV. They were able to vary heat flux and saturation temperature during micro-gravity pool boiling and compare the results to terrestrial experiments. They found that the electrical field had no appreciable effect on the boiling curve in terrestrial tests but in micro-gravity it improved vapor bubble removal from the surface and reduced degradation in heat transfer. They suggested that this was because of generation of smaller and faster bubbles (imaging was used to support this) which decreased void fraction above the heater surface. The maximum heat flux could not be extended to terrestrial levels, however, even at the highest applied potential. As mentioned above, these studies were in pool boiling in micro-gravity, where expansion of vapor in the boiling chamber was compensated by bellows and it was hard-filled with liquid initially. They focused on using the DEP force to enhance vapor bubble removal.

1.4 Objectives of current study

The objectives of this work are:

1. To study the interaction between electrical fields and flow fields in the presence and absence of liquid-vapor phase change, and presence and absence of gravity in meso- and micro-scale systems.
2. To use to the fundamental knowledge gained from analytical and experimental studies as a basis for heat transfer enhancement and thermal control in a variety of scales, applications and environments.

Chapter 2 presents the experimental development of a meso-scale EHD conduction pump with a circular channel of diameter 1.0 mm, which is used to drive a single-phase flow heat transport system in terrestrial and micro-gravity environments. Electrodes are flush with the channel wall so that the entire pumping channel does not have any obstructions to the flow. The pump is installed into a loop configuration with an evaporator, condenser and manifold. The above objectives are met by studying the effects of presence and absence of gravity on measurements such as pressure generation, flow rate and current in the pump in these environments.

In chapter 3, the study is extended to include the effects of liquid-vapor phase change by activating the evaporator and condenser downstream of the EHD pump. Since the pump has a flush-electrode design and circular configuration, the net pressure generation is a function of the pump geometry and downstream conditions such as two-phase pressure drop. Measurement of these parameters during evaporation and condensation allows for a better understanding of the relationship between meso-scale EHD conduction pump performance and downstream conditions. In addition to the above, the ability to use the meso-scale EHD conduction pump to

recover from evaporator dryout condition during two-phase flow is also investigated. Long-term (+100 hour) experiments are also conducted with the meso-scale EHD conduction pump as the sole driving mechanism of the two-phase flow heat transport system which support potential long-term applications.

In chapter 4 the focus is changed from meso-scale in-tube flow to liquid film flow driven by a micro-scale EHD conduction pump. Liquid film flow boiling is studied on a horizontal heater surface in a radial heat transport experiment. The entire liquid film flow boiling regime is studied in the presence and absence of an electric field and the presence and absence of gravity. The effect of heater surface characteristics in EHD conduction-driven liquid film flow boiling are also experimentally studied using copper-plated nanofiber-enhanced surfaces.

Chapter 5 extends the liquid film flow boiling studies by including the effect of an additional electrohydrodynamic force, namely the dielectrophoretic (DEP) force. Rather than using only the liquid film pumping via EHD conduction, a localized non-uniform electric field above the heater surface is used to generate a dielectrophoretic force for improved vapor bubble extraction during the nucleate boiling regime. The effect of liquid film height and applied potential are studied as a function of heater superheat and heat flux. The study considers the sole and combined effect of DEP with EHD conduction pumping. A brief analytical study is also used to estimate the expected dielectrophoretic force and explain the results. All of the above studies are also used to quantify the expected enhancement in heat transfer that can be achieved when heat transport systems are driven or augmented by electrohydrodynamic phenomena.

CHAPTER 2 – MESO-SCALE EHD CONDUCTION PUMPING OF DIELECTRIC LIQUID: SINGLE-PHASE FLOW STUDIES[1]

2.1 Introduction

Single-phase heat transport in meso-scale is currently a widely studied area of heat transfer with many fundamental and applied paths of research. Single-phase flow cooling loops are used in heat transfer applications such as electronics cooling where traditional passive techniques (such as fins or other extended surfaces) or fans for air cooling are incapable of removing the heat being generated in the system. While most of these have been extensively developed in macro-scale, there is an interest to develop meso- and micro-scale systems, since reduction in size results in a more compact thermal management system that is more efficient and practical than a larger macro-scale system. In this context, meso-scale refers to the length scale of the pump geometry only and not the fluid physics, i.e. possible changes in fundamental physical process that occur with such a change in the length scale are not investigated.

This shift from macro-scale to meso- and micro-scale has also occurred concurrently in EHD conduction pumping research, as outlined in the literature review. Recent work has focused in small scale systems as improved manufacturing and fabrication techniques have permitted their development. From a practical standpoint, as the spacing between electrodes approaches the order of several hundred microns (as opposed to several millimeters in macro-scale EHD pumps), the electric field strength becomes intense at lower voltages than those applied in a macro-scale pump. This is advantageous since voltages are reduced from several kilovolts to several hundred volts. In addition to the above, the effect of absence of gravity on conduction driven flows has not been explored at all. The effects of gravity cannot be eliminated under

[1] The work in this chapter has been published in [62].

terrestrial (1-g laboratory) testing. To eliminate the effects of gravity, well designed experiments need to be conducted in a microgravity environment. These experiments will enable researchers to develop an understanding of the importance of gravitational acceleration in single- and two-phase heat transfer and mass transport in EHD conduction driven flows.

The meso-pump described in this chapter has a unique disc-electrode design which ensures that the electrodes are integrated directly into the pumping channel. This prevents any obstructions which may hinder flow generation and reduce the flow rate. The present work extends the study of heat transport devices by Pearson and Seyed-Yagoobi [31] by moving from rectangular meso and micro-scale channel flow to circular tube flow and will allow examination of differences in electric field, flow field and heat transfer that result from this change in geometry. It will also pave the way for a full meso-thermal management system driven by EHD conduction as is currently developed in [42]. From an application perspective, the research and development effort and understanding of microgravity environment effects will provide technological advances that will meet the inevitable need for high heat flux thermal control for spacecraft. However, while the primary focus of this research is heat transfer enhancement and the experiment was designed accordingly, the results presented in the chapter are purely for single-phase pressure and flow generation. As such, heat transfer results are left for Chapter 3.

2.2 Terrestrial single-phase flow study

2.2.1 Meso-scale EHD conduction pump design

The electrodes in the EHD pump were designed to produce an asymmetric electric field, resulting in a net electric force and onset of fluid flow in a desired direction. For the experiments in this work, the EHD pump was fabricated from stainless steel disc-electrodes with a central hole of 1 mm diameter. There were two types of electrodes: A thick high voltage electrode and a

thinner ground electrode. The thicknesses and thickness-ratios of these electrodes and spacers were derived from numerical simulations of EHD conduction pumping. The original disc-electrode design was created by Pearson and Seyed-Yagoobi [31] for a rectangular channel. The pump was built by stacking 20 pairs of electrodes, each with PTFE Teflon spacers in between. Figure 34 shows the electrodes, along with Teflon spacers which made up a single electrode pair and the assembled EHD pump with 20 electrode pairs. At the bottom of Figure 34, from left to right, are the wide electrode, narrow spacer, narrow electrode and wide spacer.

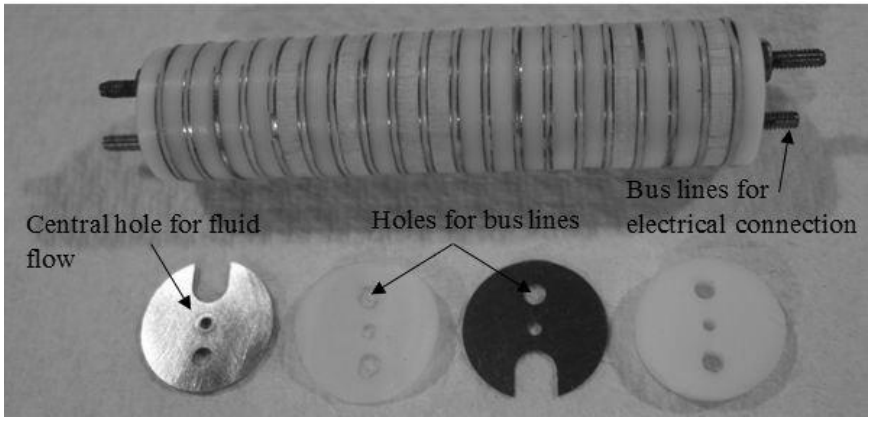

Figure 34: Assembled EHD pump with 20 pairs of electrodes (top) and individual electrodes and spacers (bottom)

The wide spacer was used to separate consecutive electrode pairs and was twelve times thicker than the space between two electrodes of a given pair. The narrow and wide electrodes were connected to the ground and high voltage lines, respectively. It has been shown both numerically and experimentally that the flow is always generated from the narrow electrode to the wide electrode, regardless of the polarity. The electrode and spacer arrangements in a single electrode pair are shown in Figure 35 and dimensions are given in Table V. The total length of the EHD pump with 20 electrode pairs is 48 mm.

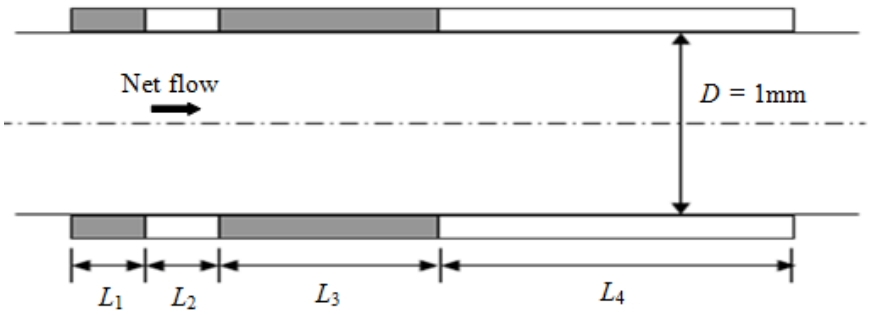

Figure 35: Single-pair electrode and spacer arrangement

Table V: Component dimensions for Figure 35

Component	Thickness
Narrow electrode	L1: 0.127 mm
Narrow spacer	L2: 0.127 mm
Wide electrode	L3: 0.381 mm
Wide spacer	L4: 1.588 mm

2.2.2 Experimental setup and procedure

The EHD pump was installed in the two-phase loop shown in Figure 36, prior to a copper evaporator tube of 1.5 mm inner diameter. The evaporator and condenser were not used in the single-phase flow experiments in this chapter and their details are given in the next chapter where two-phase flow experimental results are presented. A differential pressure transducer was installed across the EHD pumping section to measure the net pressure generated by the EHD pump. A second pressure transducer measured the pressure drop across the evaporator.

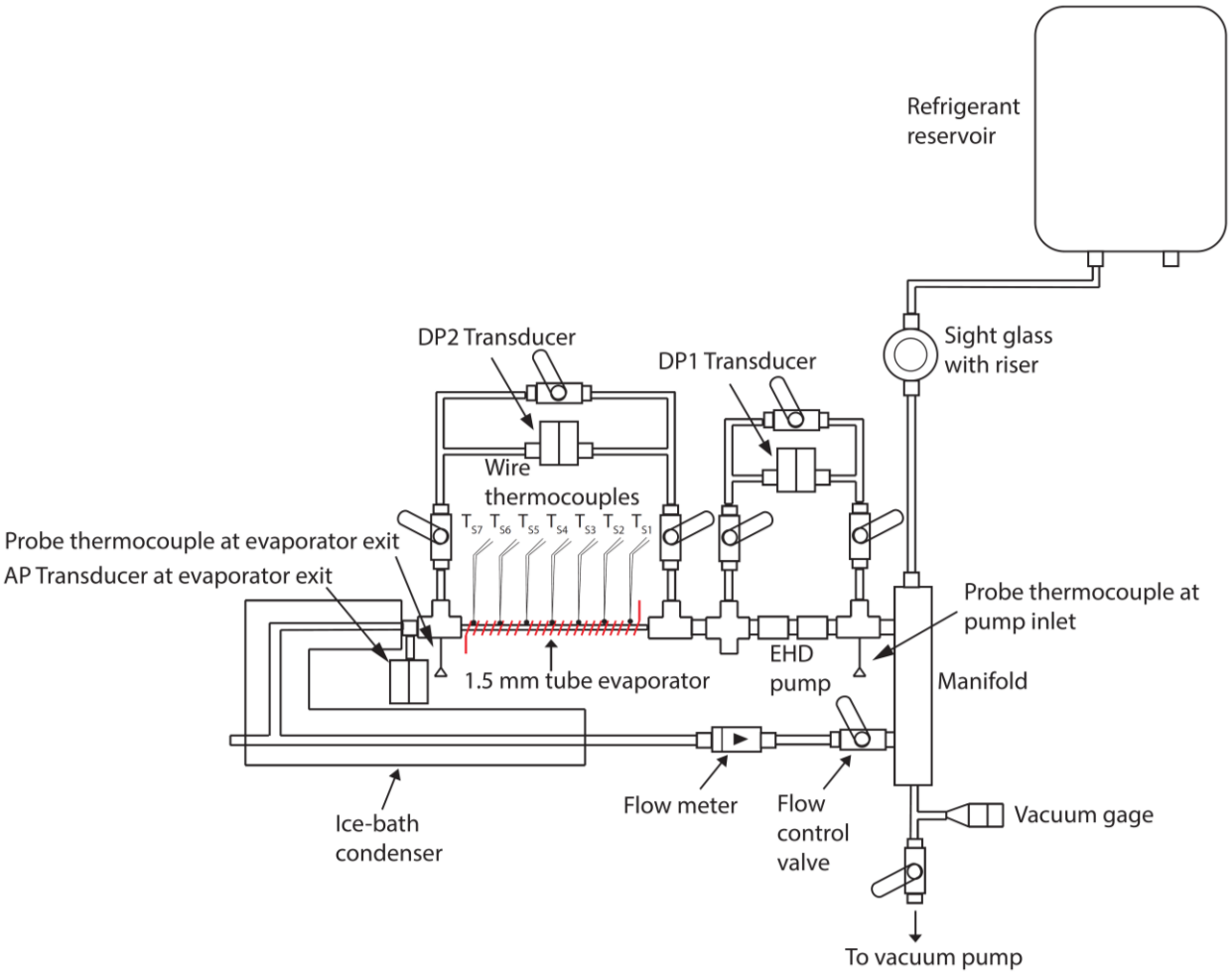

Figure 36: Experimental setup for both single- and two-phase flow terrestrial tests

The evaporator was followed by a copper-tube condenser which was in an open L-shaped box made of Plexiglas. The condenser was followed by a liquid flow sensor which measured flow rate of the liquid in the loop. The flow meter fed into a manifold which was connected to the inlet of the EHD pump, completing the loop. A sight glass with a vertical pipe was also connected to the manifold to monitor the liquid level and also allowed for any sudden vapor expansion in the system. This was sufficiently large for the small volume of liquid that the loop was charged with. The working fluid was refrigerant HCFC-123 and its properties are given in

Table VI [63, 64].The entire experiment was evacuated to 250 mTorr over a period of several hours prior to charging of the loop with the working fluid.

Table VI: Fluid properties of HCFC-123 at 25°C and 1 atm [63]

Property	Value
Liquid Dynamic Viscosity, μ_l (Pa·s)	456×10^{-6}
Liquid Density, ρ_l (kg/m^3)	1463
Sat. Vapor Density, ρ_v (kg/m^3)	6.47
Heat of Vaporization, h_{fg} (kJ/kg)	170
Liquid Specific Heat, c_p (kJ/kg)	0.965
Liquid Thermal Conductivity, k_l (W/m·K)	0.081
Surface Tension, σ (mN/m)*	15.4
Electrical Conductivity, σ_e (S/m)†	4.7×10^{-11}
Electrical Permittivity, ε (F/m)†	42.43×10^{-12}

* Surface tension is given in [65]
† Electrical conductivity and permittivity are given in [66]

The systematic errors inherent in all measurement devices were provided in manufacturer specification sheets. These values are given in Table VII. The high voltage power supply was used in the range of 0-1.5 kV with an accuracy of ±1% of the full scale range plus ±1% of the voltage setting and repeatability of ±0.1% of the full scale range. The current was in the range 0-1 mA with accuracy and repeatability in the same percentage values as voltage. The mass flow meter had a range of 0-52 ml/min with an accuracy of ±10% of the measured value and repeatability of ±1.5% of the measured value. The error for the mass flow rate is given in terms of the mass flux (mass flow rate divided by evaporator cross-sectional area) since all results in this work are presented as mass flux and not mass flow rate. The differential pressure transducers had a range of 0-750 Pa with accuracy of ±0.25% of the full scale range and the absolute pressure transducer had a range of 0-140 kPa with the same accuracy.

Table VII: Maximum systematic error of various measurement devices for chapter 2

Measurement	Maximum systematic error
Applied voltage to EHD electrodes	±30 V
Current measured through EHD electrodes	±20 μA
Mass flux*	±3.1 kg/m^2·s
Differential pressure	±10 Pa
Absolute pressure	±350 Pa

* Unlike other quantities, mass flux error is based on maximum measured value during the experiment and not the full scale range of the device.

2.2.3 Results and discussion

As mentioned above, in all single-phase flow measurements, the evaporator and condenser were not activated and the temperature throughout the loop was constant. The EHD pump was run for a period of 100 seconds before the applied voltage was increased. The net EHD pump pressure generation is shown with applied EHD voltage in Figure 37 and the pump performance is very stable. The measurement shown in Figure 37 is for the net pressure generated minus the pressure drop within the pumping section (the 1 mm diameter channel of the pump itself). The net pressure generated by the pump is mainly consumed by the evaporator section (which has an inner diameter of 1.5 mm) since all the remaining components of the loop have much larger inner diameters (> 5 mm). It should be noted that while the pressure generation is relatively low, the purpose of the experiment was to confirm the functionality of the EHD pump, rather than to provide optimum performance. Higher flow rate generation can be achieved by simply increasing the number of EHD pump electrode pairs.

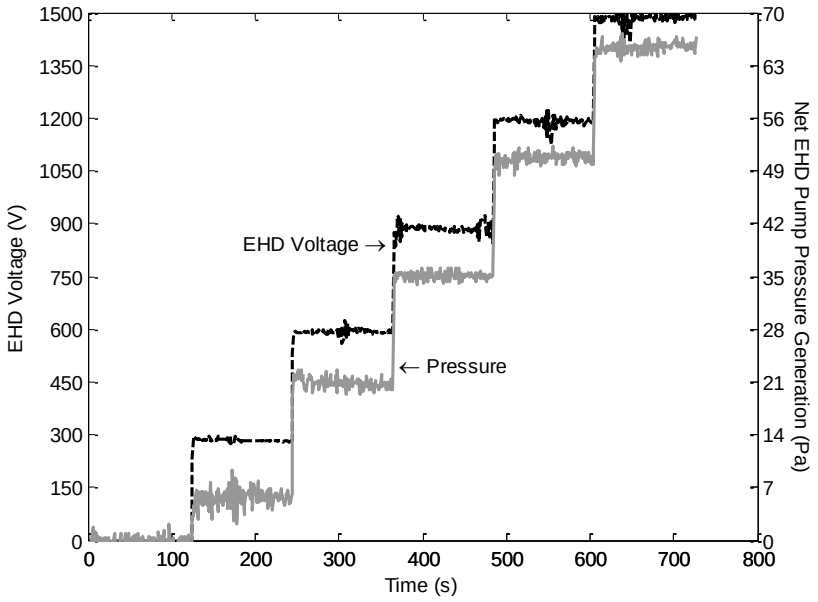

Figure 37: Net EHD pump pressure generation vs. applied EHD voltage for single-phase liquid flow

Figure 38 illustrates the flow generation capability of the EHD pump with varying applied voltage. The flow rate is shown as mass flux, i.e., the flow rate divided by the evaporator cross-sectional area. The evaporator area is used in this case since the two-phase flow results in the next chapter are also presented in terms of mass flux through the evaporator. The flow rates are relatively small due to the large pressure drop in the small 1.5 mm evaporator tube. The maximum volumetric flow rate is 2.4 ml/min at 1500V applied EHD voltage, which corresponds to a mass flux 31.5 kg/m^2·s as shown in Figure 38. The current in the EHD pump (not shown) is between 7-10 μA even at an applied voltage of 1500V since the electrical conductivity of the fluid, given in Table VI, is very low. This results in a power requirement of only 0.015W for the EHD pump.

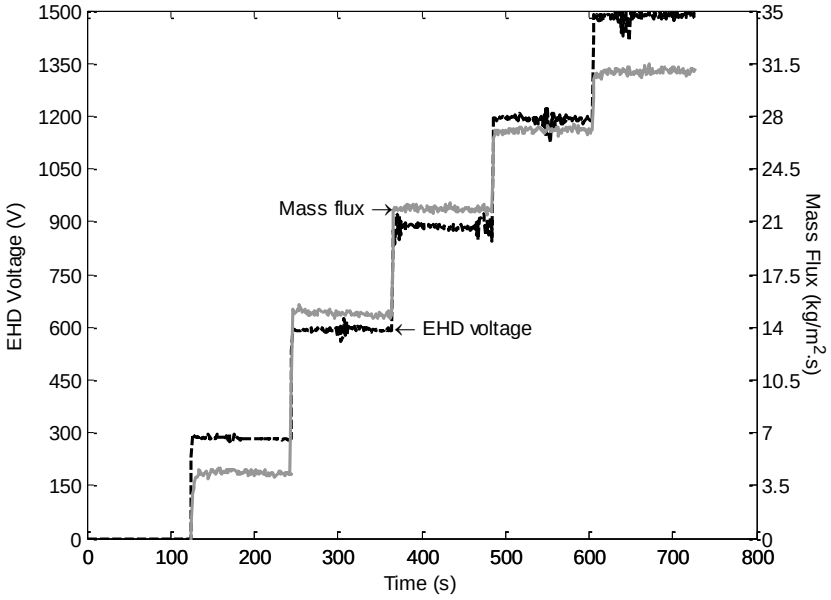

Figure 38: Mass flux vs. applied EHD voltage for single-phase liquid flow

There are some concerns about Joule heating when operating in meso- or micro-scale and these are addressed here. For an isolated pump with no fluid flow, Joule heating can cause the fluid to heat up or even vaporize, especially if the pump is well insulated and there is no heat loss to the surroundings. With the peak EHD power of 0.015W, the temperature increase rate can be up to 0.38°C/s if there is no net fluid flow for the EHD pump considered in this study. If the fluid is in a saturated state it would take approximately 8 minutes to completely vaporize all the liquid. Vaporization of liquid or bubble formation in the EHD pump channel can adversely affect pump performance so all these factors must be taken into account during experiments. For the results shown here, since the flow rate and pressure drop measurements in Figure 37 and Figure 38 are very consistent and stable during the experiments, the minute Joule heating is dissipated effectively by the net fluid flow, as it does not adversely affect the pump performance. For the lowest measured flow rate in Figure 38, the maximum expected rise in fluid temperature between the inlet and outlet of the EHD pump is 0.25°C, if all energy from Joule heating is transferred

only to the fluid (as opposed to being dissipated through the body of the pump to the environment). However, this is the worst case scenario.

2.3 Micro-gravity single-phase flow study

2.3.1 Experimental setup and parabolic flight rack design

For the parabolic flight experiments, the loop described in Figure 36 was modified to fit into a specially designed vertical equipment flight rack. The same EHD conduction pump described in the previous section (and shown in Figure 34) was installed into the heat transfer loop, which also included a preheater, evaporator, condenser and reservoir. A schematic of the modified experimental setup is shown below in Figure 39. The preheater, evaporator and condenser were not actively controlled for the parabolic flight experiments. The reservoir housed a wick structure, which – when heat was added to the liquid in the bottom of the reservoir – separated the liquid and generated vapor, allowing the saturation pressure of the liquid in the loop to be controlled based on the temperature set point of the reservoir heater. The wick was required to maintain the vapor-liquid separation during microgravity. The reservoir heater was relay-controlled to 28°C (4-6°C above ambient temperature), which corresponded to a saturation pressure of 102.3 kPa (14.84 psia) for the working fluid HCFC-123 [64].

During testing, the saturation pressure ranged from 102.0 to 105.5 kPa. Thus, the fluid in the loop was always sub-cooled because the pressure of the liquid in the loop (set by the reservoir) was greater than the corresponding saturation pressure based on temperature of the fluid in the loop (22-24°C). The following measurements were recorded during testing: absolute pressure of the fluid at the pump inlet (Druck PDCR 4361, ± 710 Pa), differential pressure across the pump (Honeywell FP2000, ± 6 Pa), liquid flow rate (Sensirion SLQ-HC60, ± 0.35 cm^3/min), acceleration due to gravity (Honeywell MA312, ± 0.02 g), applied EHD pump voltage (Trek

677B, ± 2 Vdc) and pump current (Trek 677B, ± 5 μA). Data was acquired using the Agilent 34970A data acquisition unit, two Agilent 34901A 20-channel multiplexer cards and one Agilent 34903A 20-channel general purpose switch card. A National Instruments (NI) GPIB-USB-HS controller connected to a notebook computer running NI LabVIEW virtual instrument software allowed users to control the loop.

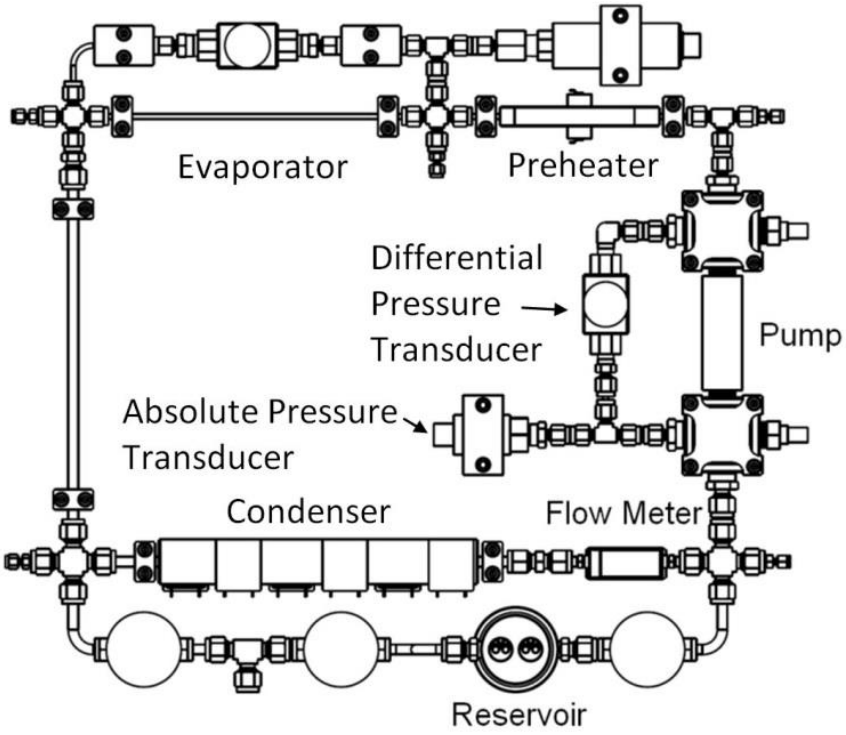

Figure 39: Modified experimental setup for single-phase flow micro-gravity tests

The experiment was flown aboard the Zero Gravity Corporation's modified Boeing 727 aircraft. The experiment was installed in a specially designed rack with all instrumentation and data acquisition systems fixed in place. The rack was then mounted in the aircraft, shown in Figure 40.

Figure 40: Vertical equipment rack installed in aircraft for micro-gravity tests

As shown in Figure 40 the experiment was located on the second shelf from the top, with the top shelf reserved for a laptop computer for data acquisition. Power supplies and other data acquisition systems were installed in the shelves below.

2.3.2 Experiment procedure during parabolic maneuver

The aircraft achieved variable gravity by performing parabolic maneuvers. The parabolic maneuvers began with a 1.8-g pull-in, followed by approximately 20 seconds of 0-g, and terminated with a 1.8-g pull-out, as shown in Figure 41 [67]. The parabolas were flown in four sets of 10 per flight in general and four flights were flown in total, over a period of four days.

The acceleration due to gravity was monitored using an accelerometer (described previously) attached to the experiment base plate where the fluid loop was also located.

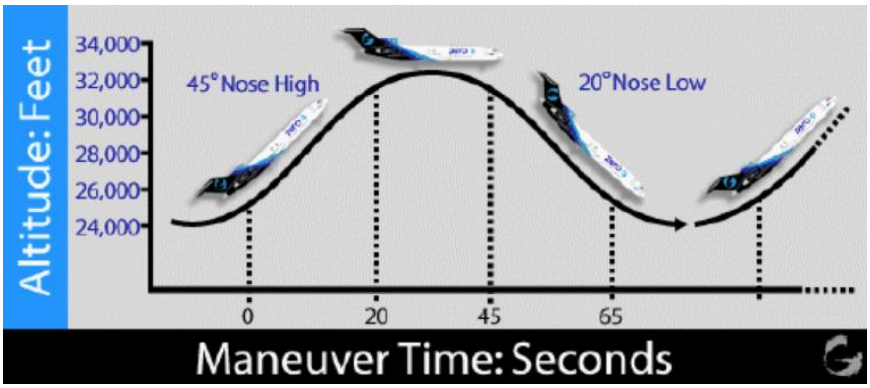

Figure 41: Parabolic flight maneuver

2.3.3 Results and discussion

Single-phase data were acquired in ground-based tests and in the microgravity environment. All data were continuously acquired by the data acquisition system even during the 1.8-g portions of the flight. The data presented in the graphs that follow are for both the high gravity and microgravity conditions and represent values averaged over the time for which the condition lasted. This information was available from the accelerometer readout. Data from ground based tests were averaged over similar periods of time in order to maintain consistency despite random uncertainties. The ground based tests were conducted immediately after the flight tests. Figure 42 shows pressure generation of the EHD pump and current as a function of applied EHD voltage in both terrestrial and variable gravity tests.

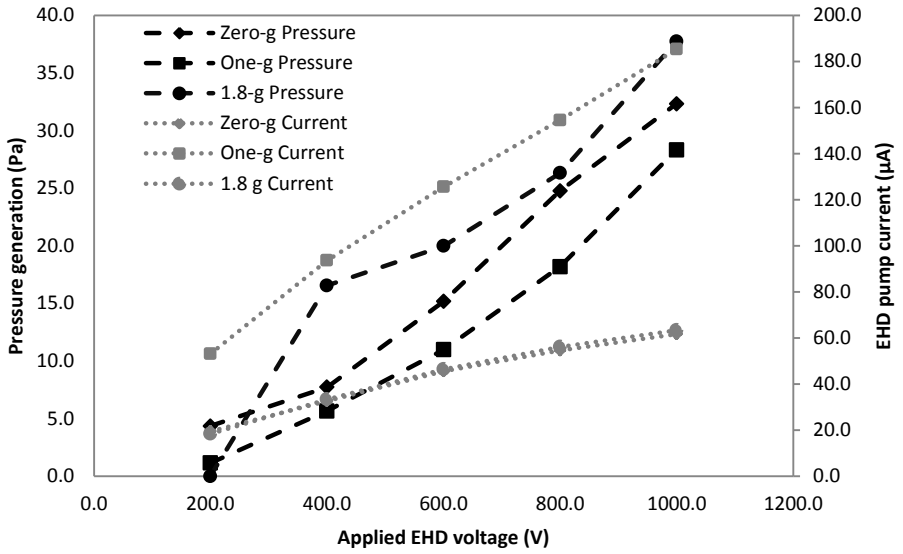

Figure 42: EHD pump pressure generation and current vs. applied EHD voltage

Whatever pressure the pump generated minus the internal pressure loss through the 1 mm diameter channel of the pump itself was consumed in the bends and tubing that made up the remainder of the loop. It should be noted that while the pressure generation was relatively low, the purpose of the experiment was to confirm the functionality of the EHD pump in microgravity, rather than to provide optimum performance. As can be seen, the pressure generation in microgravity was higher than in terrestrial tests. However, the current in terrestrial tests was significantly higher which was attributed to changes in the saturation temperature and pressure when each test was conducted. The flow rate and flow velocity generated by the EHD pump are presented in Figure 43. The flow velocity was calculated based on the cross-sectional area of the EHD pump through which the fluid flowed (i.e. the 1 mm diameter hole). As with the pressure generation, flow rate generation also showed an increase in microgravity.

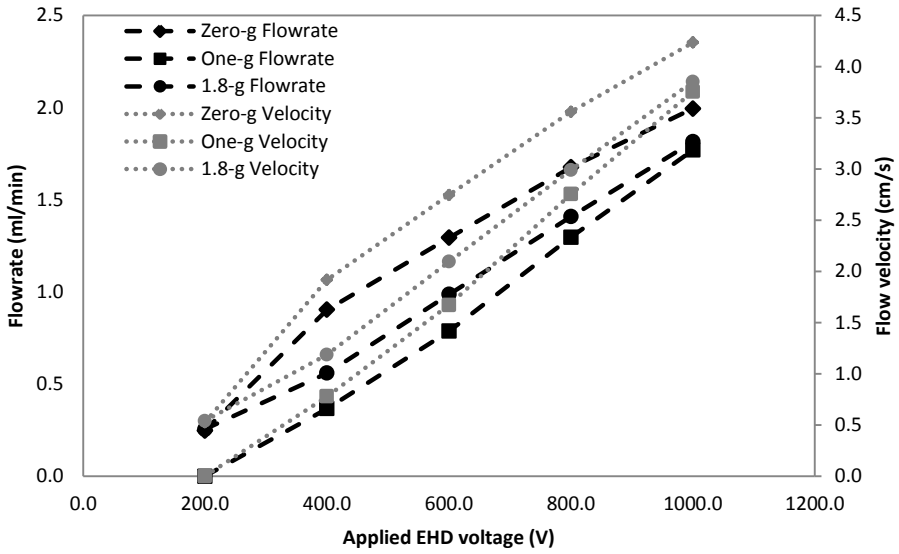

Figure 43: EHD pump flow rate and flow velocity vs. applied EHD voltage

For single-phase liquid flow in a loop, it was expected that there should have been no effect of the absence of gravity on the performance of the pump. However, from the preceding figures it can be seen that although the results were similar, there were some differences partially attributed to the above-mentioned differences in the conditions of experiments. The EHD power, calculated from the EHD voltage and current is shown in Figure 44 as a function of the applied EHD voltage.

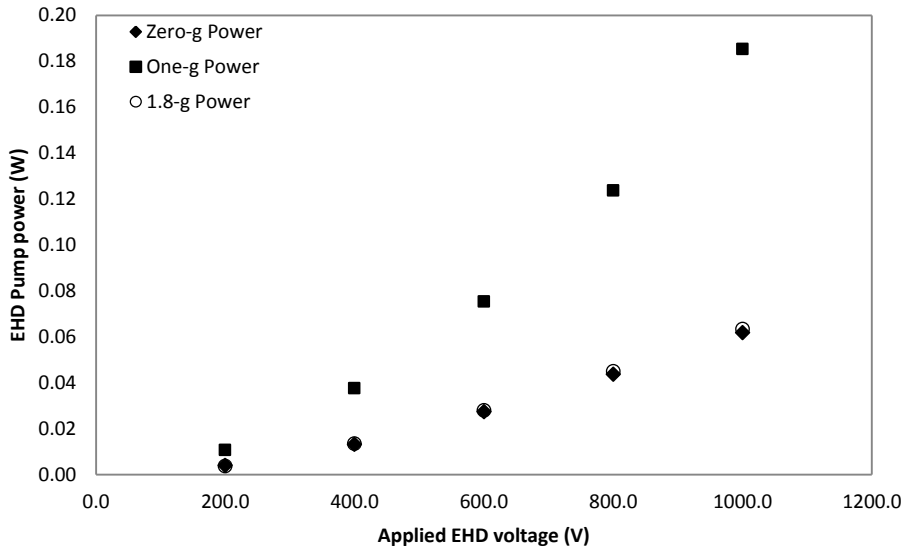

Figure 44: EHD pump power consumption vs. applied EHD voltage

The power consumption was much higher for terrestrial tests, due to the high current shown in Figure 42. From the above results, the pumping efficiencies were on the order of 0.1 % which is typical for EHD pumps in general. The efficiency depends on the flow motion, working fluid, applied potential and electrode gap. Mechanical pumps of equivalent size (meso- or micro-scale) include peristaltic or piezoelectric pumps but comparisons in efficiency are difficult. However, from [31], a more appropriate comparison is between the potential heat transport capacity and the power required and here the performance of the EHD pump was significantly more favorable since maximum power consumption was still much below 1W. This made the potential benefit of using EHD conduction pumping for various applications even greater.

2.4 Conclusions

The use of EHD conduction pumping as a liquid flow generation technique at the meso-scale was investigated. Flow and pressure generation data were acquired for the EHD pump. These data indicate that a mass flux level of 30 kg/m^2·s could be generated by the pump in 1 mm

diameter tubes at an applied voltage of 1500V. The power consumption did not exceed 0.2 W during the course of the experiment. Successful generation of these flow rates supported subsequent research into small-scale EHD conduction-driven heat transport systems.

The use of EHD conduction pumping in both terrestrial and micro-gravity environments was confirmed. Single-phase pressure and flow data indicate that the device functioned well and can be used in subsequent two-phase flow testing. While there were differences in flow and pressure generation, preliminary single-phase data show that the absence of gravity did not affect performance of EHD pumps based on conduction mechanism.

CHAPTER 3 – MESO-SCALE EHD CONDUCTION PUMPING OF DIELECTRIC LIQUID: TWO-PHASE FLOW STUDIES[2]

3.1 Introduction

As mentioned in the introduction, EHD conduction pumping has been previously well studied theoretically, numerically and experimentally. In addition to the preliminary research presented above, experimental work in macro-scale EHD conduction-assisted loop heat pipes has also been done by Bryan and Seyed-Yagoobi [38]. Loop heat pipes are commonly used in spacecraft cooling in microgravity environments as two-phase flow heat transport devices where the working fluid is driven through an evaporator and condenser by a wick structure [70]. They are reliable because they do not have any moving parts, but cannot respond to or recover from excessive pressure drops which can cause fluid flow to stop, resulting in rapid temperature rise and failure. Bryan and Seyed-Yagoobi [38] were able to successfully demonstrate EHD-assisted evaporator dryout recovery in macro-scale and first highlighted the active nature of EHD conduction pumping for use in heat transport devices. More recent efforts have shifted toward experimental work in meso- and micro-scale EHD conduction pumping for both single- and two-phase flow. Therefore, EHD conduction is at an appropriate stage of development to be used as the sole driving mechanism for a meso-scale, two-phase flow heat transport system in the presence and absence of gravity.

Heat transport for devices that operate in meso- or micro-scale is a challenging problem that is receiving much attention due to recent advances in microchip technology that are used in a variety of applications, such as aerospace components, aircraft avionics and even hybrid vehicle power electronics [71]. Aerospace components in satellites have the added challenge of

[2]The work in this chapter has been published in [68] and [69].

operating in a microgravity environment with high fluctuations in temperature. Therefore, there is a strong motivation to develop an active meso- or micro-scale, two-phase flow heat transport system that can function well both in terrestrial and microgravity applications. There is a focus on two-phase flow because it can result in higher heat transfer coefficients with much less flow rate compared to single-phase flow, since it capitalizes on latent energy of the working fluid rather than only the sensible energy. At the same time, scaling geometry down from macro-scale to meso- or micro-scale results in increasingly compact thermal management systems. This combination of actively controlled meso- or micro-scale two-phase flow is especially useful in microelectronics, which have localized hot spots that cannot be cooled efficiently by macro-scale systems. Although the overall heat removal may be moderate, cooling of hot spots in microelectronics can extend their operating power and avoid failure [72].

There are four main motivations for the work in this chapter. The first is an extension of the work already done in macro-scale by Bryan and Seyed-Yagoobi [38]. In the present work, the system is scaled down in size by several orders of magnitude to meso-scale. The EHD pump is the only driving mechanism for the flow through the heat transport device and capillary pressure head from a wick is not present. However, the EHD pump is effectively used to drive the two-phase flow heat transport system and evaporator dryout recovery is still achieved in the same manner as in [38], demonstrating the scalability of the technique. This is presented in section 3.4.

The second motivation of this work concerns gaining new insights into EHD-driven two-phase flow systems. Although the EHD pump utilized in this study is adiabatic, two-phase flow pressure drop and flow regimes in the evaporator downstream play an important role in upstream EHD pressure generation. Thus, via this current work, an important fundamental understanding

of EHD conduction pumping performance in a two-phase system has been observed. This two-phase flow system is different from traditional mechanically-driven systems since it has an open channel and does not have impellers or vanes. This new understanding is presented in section 3.5.

The third motivation of this work focuses on determination of low mass flux boiling heat transfer coefficients in a meso-scale circular tube evaporator where the flow is driven by an upstream EHD pump. Flow boiling in meso- and micro-channels of various geometries and moderate to high mass fluxes has been studied in great detail and selected works are in [73-76]. However, previous work in this area, summarized and tabulated by Qu & Mudawar [73] and Bertsch et al [74], clearly show a need for flow boiling heat transfer data in the low mass flux regime. The low mass fluxes generated by the meso-scale EHD pumping in the current work facilitate the determination of flow boiling heat transfer coefficients. The experimental results are compared to known correlations as well. This is presented in section 3.6.

The final motivation of the work in this chapter concerns long-term performance evaluation of the meso-scale EHD conduction-driven heat transport system. As previously mentioned, there are many terrestrial applications of EHD technology but the non-mechanical nature of the EHD pumps makes them especially suitable for aerospace applications, where they can be used in heat transport systems for thermal management of satellites and other spacecraft. Unlike other methods of EHD pumping such as ion-drag or induction, EHD conduction is a relatively mature technology which is at Technology Readiness Level (TRL) 5, as outlined by various agencies such as NASA [77]. The pressure and flow rate generation is sufficient for EHD conduction pumps to be successfully implemented in heat transport systems and an EHD conduction-driven system has even been tested in a reduced gravity environment as outlined in

the previous chapter. However, the next step in the development of EHD conduction is the long-term performance evaluation of a meso-scale pump. This is an extremely important step as it demonstrates the viability of using a stand-alone EHD-driven system in various applications. Long-duration spacecraft missions can take months or even years and thus long-term pump performance for thermal control is a valuable metric. To the authors' knowledge, data for such long-term tests in EHD conduction pumping-driven two-phase flow are not found in the current literature so this research also fills a gap in that area. This is presented in section 3.7.

3.2 Experimental setup

The same EHD pump (shown in Figure 34) and experimental setup (shown in Figure 36) described in the previous chapter was used for the two-phase flow experiments. As mentioned above, the evaporator was made of a copper tube with an inner diameter of 1.5 mm. The evaporator length was based on the required heating length necessary for full phase change from liquid to vapor of the working fluid at the maximum flow rate. Seven T-Type, fine gage wire thermocouples were soldered to the evaporator outer surface for wall temperature measurements and these are labeled in as T_{S1}-T_{S7} in Figure 36. The evaporator tube wall thickness was 0.5 mm and the thermal conductivity of the copper was 401W/m·K. At the highest heat flux of 1W/cm^2 the outer wall temperature of the evaporator was 30°C and a one-dimensional radial conduction analysis determined the inner wall temperature to be 29.99°C. Thus, the outer wall surface temperatures were approximated as the inner wall surface temperatures to calculate the heat transfer coefficients. The evaporator was wrapped with low-resistance Nichrome heater wire to generate a uniform heat flux. Voltage and resistance measurements were used to compute the electrical power generated by the heater wire. The heater power was divided by the evaporator tube inner surface area to determine the heat flux. The voltage to the heater wire was controlled

accurately by using a programmable power supply that was connected to an analog output signal from the data acquisition system. The evaporator was well insulated to prevent heat loss to the surroundings. This was confirmed by insulation outer surface temperature measurement using a fine gage wire thermocouple. For the duration of all experiments this value did not exceed the ambient temperature (also measured) by more than 0.2°C, which corresponded to approximately 0.03W of heat loss to the surroundings. T-Type probe thermocouples were used to measure bulk fluid temperature at the pump inlet and evaporator exit.

An absolute pressure transducer also measured pressure at the exit of the evaporator. As shown in Figure 36, this was coupled with the probe thermocouple to determine the thermodynamic state of the fluid exiting the evaporator. The evaporator was followed by a copper-tube condenser which sat in an open L-shaped box made of Plexiglas. Crushed ice was placed in the box to condense the vapor and this produced sub-cooled liquid at the condenser exit. During all experiments the probe thermocouple at the EHD pump inlet was used to confirm that the bulk fluid temperature was ~1°C below the saturation temperature, indicating that sub-cooled liquid always entered the pump and evaporator.

The systematic errors inherent in all measurement devices are provided in manufacturer specification sheets. These values are given in Table VIII, along with uncertainty analysis for derived quantities. Thermocouples were T-type with Special Limits of Error (SLE) and met Tolerance Class EN 60584-2. They were confirmed using a NIST Standard Thermometer to an accuracy of ±0.05°C to show consistency. The high voltage power supply was used in the range of 0-1.5 kV with an accuracy of ±1% of the full scale range plus ±1% of the voltage setting and repeatability of ±0.1% of the full scale range. The current was in the range 0-1 mA with accuracy and repeatability in the same percentage values as voltage. The evaporator power supply had a

range of 0-120 VDC and an accuracy of ±0.05% of the full scale range, with 5 mV ripple. The mass flow meter had a range of 0-52 ml/min with an accuracy of ±10% of the measured value and repeatability of ±1.5% of the measured value. The error for the mass flow rate is given in terms of the mass flux (mass flow rate divided by evaporator cross-sectional area) since all results in this work are presented as mass flux and not mass flow rate. The differential pressure transducers had a range of 0-750 Pa with accuracy of ±1.33% of the full scale range and the absolute pressure transducer had a range of 0-140 kPa with the same accuracy. The random errors arising from repeated measurements are shown directly in the graphs for heat transfer coefficient in the next section in terms of standard deviation. The standard deviations are shown as error bars with one standard deviation above and below the mean values.

Table VIII: Maximum systematic error of various measurement devices and experimental uncertainty for chapter 3

Measurement	Maximum systematic error
Temperature difference	±0.5°C
Applied voltage to EHD electrodes	±30 V
Current measured through EHD electrodes	±20 μA
Applied voltage to evaporator	±0.06 V
Resistance of evaporator wire	±0.05 Ω
Mass flux*	±3.1 kg/m^2·s
Differential pressure	±10 Pa
Absolute pressure	±350 Pa
Derived quantity	**Maximum Uncertainty**
Heat flux, q''	±1.7%
Vapor quality, x	±10.2%
Heat transfer coefficient, h	At ΔT = 2.3°C: ±22% At ΔT = 2.8°C: ±18% At ΔT = 5.1°C: ±10%

* Unlike other quantities, mass flux error is based on maximum measured value during the experiment and not the full scale range of the device.

3.3 Experimental method to determine flow boiling heat transfer coefficients and vapor quality

The flow boiling heat transfer coefficients were determined as a function of the vapor quality along the evaporator tube length. The experiment began with a fixed applied EHD potential of 900V which generated a steady, single-phase flow. The wall temperatures rose in a steady manner as well during the initial stages and only sensible heating was taking place with liquid forced convection. Next, the heat flux was incremented slowly until the working fluid

completely changed phase from liquid to vapor in the evaporator. This was done for every experiment. Performing an energy balance between heat applied and heat transported ensured that the fluid was exiting the evaporator at a vapor quality as close to 100% as possible. The required phase change heat was determined from the real-time measurement of mass flow rate and the latent heat of vaporization from thermodynamic tables for HCFC-123 in [64]. The bulk inlet temperature to the evaporator remained constant throughout the experiment which indicated that the condenser effectively dissipated heat from the loop.

The exit condition of the fluid was determined from saturation temperature and pressure measurement and location of these measurements are indicated in the experimental setup in Figure 36. The measurements were matched to the saturation temperature and pressure in the thermodynamic tables for HCFC-123. The vapor quality, x_i, at each thermocouple station along the evaporator length was found according to the above-mentioned energy balance (the index *i* represents the points along the evaporator tube where the wall surface temperature was measured, as shown in Figure 36) using Eq. (39).

$$x_i = \frac{q}{\dot{m} h_{fg}} \cdot \frac{l_i}{L} \tag{39}$$

In Eq. (39), l_i is the distance from the evaporator inlet to each thermocouple station, *i*. The applied heat and temperature difference, ΔT (i.e., difference between evaporator wall surface temperature at thermocouple station *i* and evaporator exit saturation temperature), were used to determine the local flow boiling heat transfer coefficient in Eq. (40). The use of evaporator exit saturation temperature as a reference for local heat transfer coefficient calculation is justified as follows: the two-phase flow pressure drop measurements in the evaporator (shown below) do not exceed 200 Pa for all heat transport experiments. From thermodynamic property

tables for HCFC-123, at these operating conditions, a decrease of 200 Pa in saturation pressure would cause the saturation temperature to decrease by 0.06°C. A change of 0.06°C in ΔT in the denominator of Eq. (40) results in a maximum change of 101 W/m^2·K in the local flow boiling heat transfer coefficient for the given operating conditions. From Figure 47, the minimum value of h_i is 1950 W/m^2·K so this represents a deviation of only 5.2%. Therefore, the assumption is justified.

$$h_i = \frac{q''}{\Delta T} = \frac{q''}{\left(T_{S,i} - T_{sat,exit}\right)} \tag{40}$$

During phase change experiments, temperature, pressure drop and flow rate oscillated about a mean value. Steady state was defined as the condition where the mean wall/saturation temperature, pressure drop and flow rate did not change by more than 0.1°C, 10 Pa and 0.4 ml/min, respectively, for 10 minutes. The data were recorded once steady state was achieved for each parameter. For each experiment 10 minutes of data were recorded at one sample per second, resulting in a total of 600 data points which were averaged for the final value of heat transfer coefficient and quality. The standard deviation was also calculated and error bars show one standard deviation above and one standard deviation below a particular data point. The mass flux was varied by changing the applied voltage to the EHD pump and the experiment was repeated for three different mass fluxes.

3.4 Two-phase flow experimental results: EHD-driven evaporator dryout recovery

The experimental results of the EHD-driven two-phase flow heat transport and dryout recovery experiment are shown in Figure 45 and Figure 46. Here the effects of phase-change give vastly different results compared to single-phase flow presented in the previous chapter. The same experimental method described above for determining boiling heat transfer coefficient was

used. In order to reach the dryout condition, the heat flux to the evaporator was incremented and the evaporator wall temperatures near the outlet were closely monitored. When the temperatures suddenly increased with only a small increase in the heat flux, this was assumed to be the onset of dryout condition. This was also confirmed by the evaporator exit saturation pressure measurement, which indicated that significantly superheated vapor was exiting the evaporator and only vapor forced convection was taking place near the outlet. Figure 45 shows the two wall temperature measurements near the evaporator exit (labeled as T_{S6} and T_{S7} in Figure 36) and heater power during the experiment. The points at which the applied EHD voltage was changed are also labeled in the figure.

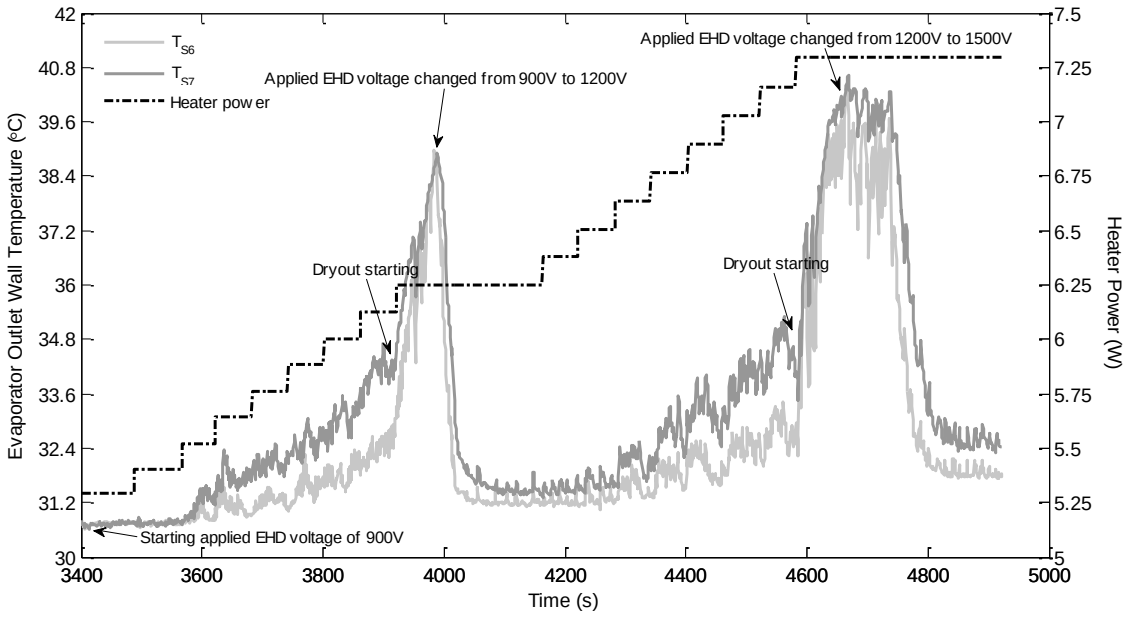

Figure 45: Evaporator temperature and heater power variation during heat transport and dryout recovery experiments of EHD-driven two-phase flow device

The upper limit of the applied voltage to the EHD pump for both single- and two-phase tests was 1500V and this determined the maximum flow rate. Exceeding this voltage led to

potential dielectric breakdown and failure of the EHD pump, so all experiments were run with a maximum of 1500V. The temperature was only allowed to increase for a few seconds once dryout started before increasing the applied EHD voltage. However, the time taken for actual dryout recovery was much longer at higher heat fluxes. Figure 45 shows that the wall temperatures dropped down to steady-state condition ~90 seconds after the applied EHD potential was changed from 1200V to 1500V. The reason the temperatures dropped was that the higher EHD pressure generation resulted in flooding of the evaporator with fresh cool liquid and allowed dryout recovery. The process was repeated for a higher heat flux to demonstrate the adaptability of the system to an increase in the heat transport requirement.

Figure 46 shows the net EHD pressure generation and evaporator two-phase flow pressure drop during the heat transport and dryout recovery experiment. The points at which the applied EHD voltage is increased coincide with higher pressure generation. The two-phase pressure drop and mass flow rate measurements indicate that the flow oscillated significantly about a mean value. The plots of pressure in the figure are averages of the instantaneous measurements.

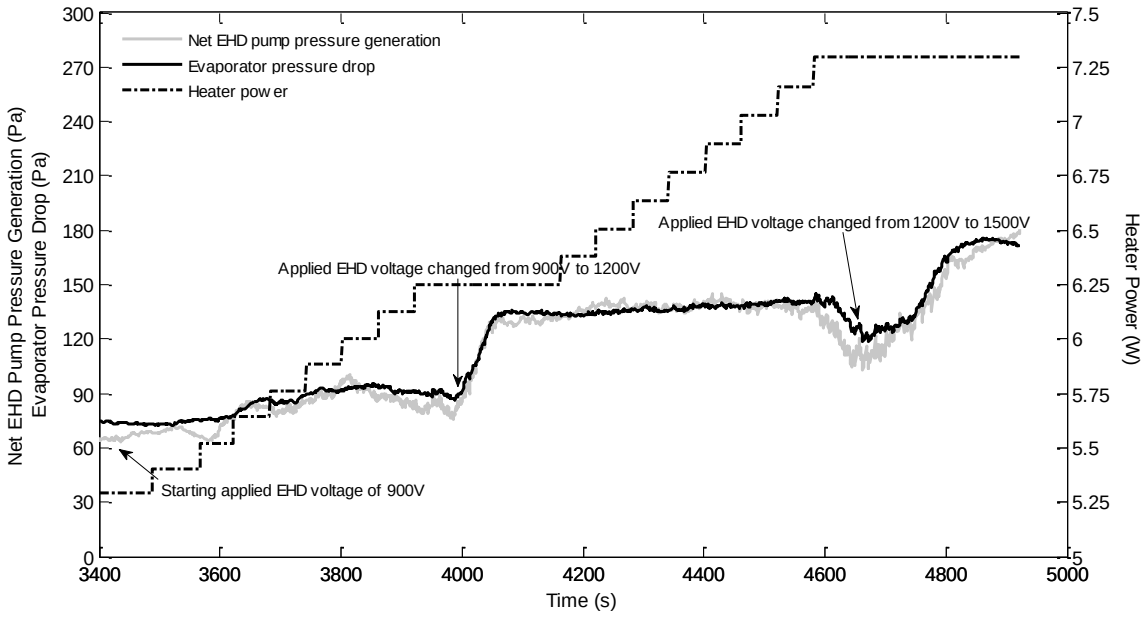

Figure 46: Net EHD pump pressure generation and evaporator pressure drop during heat transport and dryout recovery experiments of EHD-driven two-phase flow device

The changing downstream conditions in the evaporator and condenser also affected the pressure drop across the EHD pump. As illustrated above, the net EHD pump pressure generation closely matches the evaporator pressure drop. Although there were losses in other parts of the loop, the data indicate that the dominant pressure drop occurred in the evaporator during two-phase flow. As stated previously, the inner diameters of the EHD pump, evaporator and condenser are 1 mm, 1.5 mm and 5.33 mm, respectively (connecting lines had inner diameters equal to or larger than the condenser). Since frictional pressure drop in a circular pipe scales with diameter to the fifth power for a given mass flow rate, the pressure drop in the condenser and the rest of the loop is bound to be negligible compared to the evaporator. The small inconsistencies where evaporator pressure drop appears to exceed the net EHD pump pressure generation are simply due to uncertainty in the pressure measurement.

3.5 Fundamental observation of EHD pump net pressure generation

When the net EHD pump pressure generation for single- and two-phase flow (in Figure 37 and Figure 46, respectively) is compared, an important effect is observed. The data indicate that at a fixed applied EHD voltage, the net pressure generation by the EHD pump is higher for two-phase flow than for single-phase flow in the loop (note that in either case the fluid inside the EHD pump is a single-phase liquid). The reason for this interesting observation is as follows. Despite an increase in the EHD pump pressure generation with two-phase flow in the loop, the corresponding flow rates are lower than those of single-phase fluid flow in the loop (e.g. for the two-phase flow experiments in Figure 46, the mass flux was 17.02 $kg/m^2 \cdot s$ at 1500V applied EHD voltage; for single-phase experiments in Figure 37, the mass flux was 31.5 $kg/m^2 \cdot s$ at the same applied EHD voltage). This reduction in the flow rate is expected due to large pressure drops associated with the phase-change in the evaporator and the condenser (the corresponding pressure drop can be neglected in the condenser due to its much larger diameter). Therefore, for the EHD pump an increased downstream pressure drop decreases the flow rate resulting in an increase in the residence time of the fluid inside the pumping section. This, in turn, enables the convection of charged particles. The convection is not dominated by the flow and this allows for more gradual formation of heterocharge layers in the vicinity of the electrodes. This increases the net pressure generation of the pump. Indeed, when there is no net flow (by closing the flow channel with a valve, for example) EHD pressure generation is highest. This type of effect is the result of the electrostatic nature of operation. The results add some new experimental data since there is very limited information for the relationship between EHD-driven flow and pressure drop in circular geometry in meso-scale. The existing results in the literature, e.g. [31, 42], for a particular configuration or geometry cannot necessarily be utilized for all others, since EHD

pump pressure generation strongly depends on these factors. In addition, the pump has an open channel (it does not contain an impeller or vanes) and pressure generation is affected by downstream conditions, which is demonstrated through these results.

The above experimental results can be used to compare to operation of existing technology such as standard loop heat pipes which have capillary pressure head developed through the wick structure. The maximum heat transfer attainable is achieved when this balances with pressure losses along the vapor-liquid path [70]. The heat pipe cannot operate properly when the losses become too high and in this regard the EHD-driven heat transport device provides a significant advantage, as illustrated in the figures above. The input power required to generate sufficient pressure to successfully operate the device in this work is very minimal, compared to the heat transport achieved. As stated previously, in the highest mass flux case shown in Figure 45, the maximum measured input electric power to the EHD pump was only 0.015W for the heat transport of 7.3W, i.e. only 0.21% of the total heat transported by the system was used to power the EHD pump. This is an inconsequential power requirement considering the active control nature of an EHD-driven two-phase flow heat transport device when compared to a conventional wick heat pipe. Although efficiency of EHD conduction pumps is low (<5%) compared to mechanical pumps, the comparison between input power and heat transport capacity provides a more appropriate measure of performance.

3.6 Two-phase flow experimental results: Low mass flux boiling heat transfer coefficients

The local flow boiling heat transfer coefficients in the 1.5 mm inner diameter evaporator tube were found according to the experimental method described above. Figure 47 shows heat transfer coefficient plotted as a function of vapor quality at three levels of mass flux. The

additional line plots in Figure 47 are the results of flow boiling correlations and will be discussed in the section that follows.

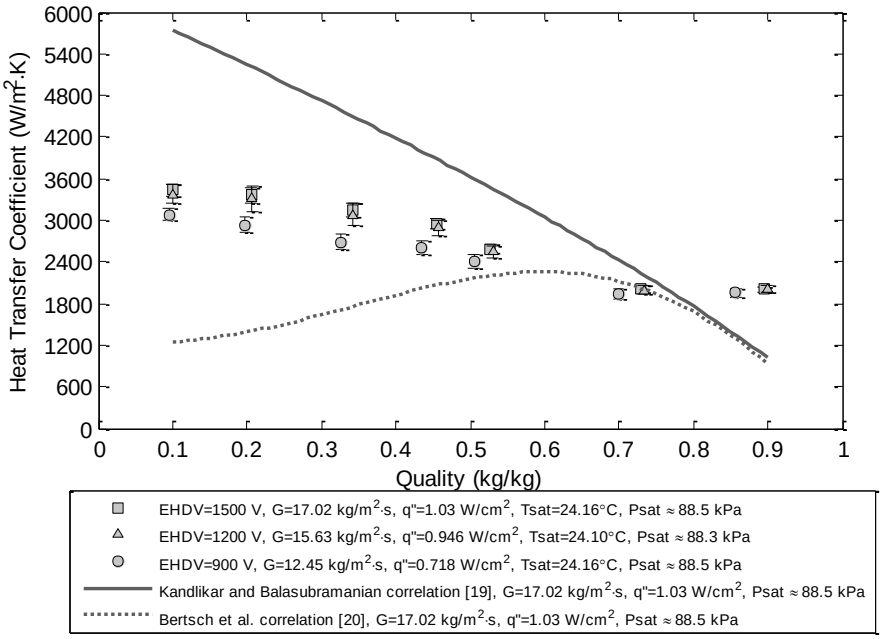

Figure 47: Flow boiling heat transfer coefficient of HCFC-123 vs. quality for circular copper tube (D=1.5 mm), with comparison to two correlations

The applied EHD voltages are provided in the legend because flow rate generation directly depends on the applied EHD voltage. However, for the purpose of comparison to correlations, the heat transfer coefficient data are independent of the flow generation technique, i.e. they would be the same if the flow was generated using any other type of pump (mechanical or otherwise) if the same mass flux could be reproduced by said pump.

The results in Figure 47 show that for this mass flux range, the internal flow convective boiling heat transfer coefficient decreases with increasing quality. At higher vapor quality the data for varying mass flux appear to converge. Even though the mass flux changes are small, the influence of the mass flux on heat transfer coefficient is apparent, i.e. as mass flux increases so

does the heat transfer coefficient. The trends of local internal flow boiling heat transfer coefficient vs. vapor quality in micro- and meso-channels have been discussed extensively in the literature. A recent critical review of micro-channel flow boiling heat transfer by Kandlikar [76] indicates this particular trend of heat transfer coefficient decreasing with increasing vapor quality has been observed experimentally by many researchers. The reason for this trend is as follows. At the inlet of the evaporator there is single-phase liquid flow with forced convection. The flow goes through various regimes in the entrance region of the evaporator and nucleate boiling occurs. The heat transfer rate is high in this region and wall temperatures are low, resulting in the largest values of local heat transfer coefficient at low quality. Nucleate boiling transitions into annular flow with a liquid film at the tube wall and a vapor core. The heat transfer rate is reduced in this region as wall temperatures become higher. Eventually, dryout of the liquid film at higher qualities results in a further drop in heat transfer and significant increase in wall temperature. The flow reaches single-phase vapor toward the exit of the evaporator tube with the lowest local heat transfer coefficients. A pertinent example from the review in [76] is the work done by Yen et al. [78] , where flow boiling of HCFC-123 was studied in stainless steel circular tubes with 0.19, 0.3 and 0.51 mm inner diameter. Typical experiments conducted in the 0.51 mm tube at a mass flux of 145 $kg/m^2 \cdot s$ and heat flux of 1.2 W/cm^2 resulted in the same trend in Figure 47 whereby the heat transfer coefficient gradually decreased as the vapor quality was increased (it is important to note that a mechanical pump was used for those experiments). The maximum heat transfer coefficient was on the order of 10 $kW/m^2 \cdot K$, compared to a maximum of 3.4 $kW/m^2 \cdot K$ in our work. The reasons for the difference are the significantly higher mass flux and the smaller tube diameter in their experiments. They also reported that increasing the mass flux from 145 $kg/m^2 \cdot s$ to 295 $kg/m^2 \cdot s$ while maintaining a constant heat flux did not change the heat transfer

coefficient significantly, which suggests that the mass flux influence is only important below a certain value and at low vapor qualities.

In order to determine whether the same trend (of heat transfer coefficient as a function of vapor quality) would result using known micro- and meso-scale flow boiling correlations, the experimental data in Figure 47 were compared to two correlations. This emphasizes the value of the current experimental data reported in Figure 47 as general meso- and micro-scale correlations currently available are only suitable for higher ranges of heat and mass fluxes. The first correlation was by Kandlikar and Balasubramanian [79] and it was chosen because it was extended to account for deep laminar flows (i.e. for all-liquid Reynolds number, $Re_{LO} \leq 100$) in channels with a hydraulic diameter, $D_h < 3$ mm. It was based on experimental data for ten fluids including water and several refrigerants. The correlation consisted of a convective boiling term and a nucleate boiling term. The all-liquid Reynolds number delineated which term dominated over the other. For the deep laminar regime, the nucleate boiling component dominated and the convective boiling component could be neglected. In the current work, the all-liquid Reynolds number range was $42 \leq Re_{LO} \leq 58$ for the evaporator tube inner diameter of 1.5 mm. The Kandlikar and Balasubramanian [79] correlation is given below in Eq. (41), where $h_{FB,NBD}$ is the flow boiling heat transfer coefficient for nucleate boiling-dominant flow.

$$h_{FB,NBD} = 0.6683Co^{-0.2}(1-x)^{0.8}h_{LO} + 1058.0Bo^{0.7}(1-x)^{0.8}F_{Fl}h_{LO} \quad (41)$$

The single-phase, laminar, all-liquid flow heat transfer coefficient, h_{LO}, was a constant for the whole tube. It was calculated using Nu = 4.36, corresponding to a constant surface heat flux. The Boiling number, Bo, was dependent on the heat flux and mass flux, while the Convection number, Co, was dependent on the vapor quality and liquid/vapor density ratio. As the heat and mass fluxes were increased, the Boiling number increased and as the quality increased, the

Convection number decreased. The fluid-surface parameter F_{Fl} was found in [79] and taken to be equal to 1.3. This value was not available for HCFC-123 so F_{Fl} for CFC-11 was chosen as an alternative. This was justified because HCFC-123 was originally created as an environmentally-safe substitute for CFC-11 and there is a maximum 9% difference between their respective values of viscosity, specific heat, thermal conductivity and density at a given temperature [63]. Equation (41) was used to calculate the flow boiling heat transfer coefficient and the result is plotted in Figure 47 along with the current experimental data. The correlation did not yield any difference in results for the three different mass fluxes (and corresponding heat fluxes) considered in the experiment.

The second micro- and meso-scale flow boiling heat transfer correlation was by Bertsch et al. [80] which was developed from a database of 3899 points covering 12 different fluids including refrigerants, for hydraulic diameters ranging from 0.16 to 2.92 mm. The mass flux ranged from 20 to 3000 kg/m^2·s and heat flux ranged from 0.4 to 115 W/cm^2. Although the mass fluxes for the current experimental data (12.45 kg/m^2·s ≤ G ≤ 17.02 kg/m^2·s) were below the ranges mentioned, the heat flux was within range (0.718 W/cm^2 ≤ q" ≤ 1.03W/cm^2) and so was the evaporator tube diameter (1.5 mm). The correlation had a convective heat transfer and nucleate boiling component but also included the effect of bubble confinement in small channels, in the form of a Confinement number, Cn (not to be confused with the above Convection number). The flow boiling heat transfer coefficient, h_{FB}, is represented as the sum of weighted terms for nucleate boiling and convective heat transfer

$$h_{FB} = h_{NB} \cdot S + h_{conv,tp} \cdot F \tag{42}$$

where S is a suppression factor for the nucleate boiling to account for dryout at higher vapor quality and F is a correction factor for convective heat transfer to account for enhanced

convection at higher flow velocities that occur at increased vapor quality. The determination of both these factors are explained in detail in [80]. Bertsch et al. chose appropriate correlations for the nucleate boiling and convective heat transfer terms based on how well they fit experimental data. The nucleate boiling term is a function of heat flux, reduced pressure and molar mass of the fluid. The suppression factor had a simple linear dependence on vapor quality i.e. as the vapor quality increased, S decreased which caused the nucleate boiling term in Eq. (42) to decrease. This implied that at higher vapor qualities nucleate boiling was diminished and as a result bubble growth stopped. For the convective heat transfer term, the average is found for all-liquid and all-vapor flow and these are related linearly with the vapor quality. The factor F was a function of Confinement number (determined by the surface tension and density difference between liquid and vapor phase) and vapor quality. The vapor quality is a polynomial function and the term involving Cn is an exponentially decaying function. This means that when F is multiplied by the convective heat transfer term, the product of the two quantities first increases with increasing quality and then decreases. The prediction of the Bertsch et al. [80] correlation is shown in Figure 47 with the experimental data. As in the case of Kandlikar and Balasubramanian [79], this correlation did not yield any difference in results for the three mass fluxes (and corresponding heat fluxes) considered.

From Figure 47, it is apparent that our experimental data fall in between the predictions of both correlations. The correlation by Kandlikar and Balasubramanian [79] shows that the flow boiling heat transfer coefficient decreases steadily with increasing vapor quality and this trend is consistent with our experimental data. However, it also over-predicts the heat transfer coefficients at low qualities where the maximum deviation from our experimental data is 60%. At a quality of 0.75, the correlation crosses the experimental data and under-predicts the flow

boiling heat transfer coefficient at the highest quality levels. The over-prediction at low quality suggests that nucleate boiling is not necessarily dominant throughout the evaporator. The results of the second correlation by Bertsch et al. [80] show that the heat transfer coefficient first increases with vapor quality and then decreases. The prediction is in general disagreement with our experimental data at lower qualities, with a maximum deviation of 37%. However, it is interesting to note that as with the first correlation, the prediction from the second correlation also coincides with our experimental data at a quality of 0.75. After this point, both correlations predict the same trend and appear to converge. The correlation by Bertsch et al. also indicates that the suppression of nucleate boiling occurs at a quality of ~0.65. Again, this is contrary to the argument that nucleate boiling dominates throughout the tube. In the downstream region of the evaporator, where quality approaches 1, heat transfer to the fluid is severely diminished. For this reason, the axial conduction through the evaporator tube was quantified. Results of a numerical simulation (described in Appendix B.1, Figure 84 and Figure 85) showed that axial conduction accounted for up to 10% of heat load compared to radial conduction, effectively decreasing the heat transfer coefficients at highest vapor quality, shown in Figure 47. If this correction was applied, there would be better overall agreement between experimental data and the predictions of both correlations for vapor quality >0.5. In summary, our experimental data fall in between the two correlations at lower quality and neither correlation shows different results with varying mass fluxes in this particular range. However, it is important to mention that these correlations were not quite applicable in this range of experimental conditions. This highlights the usefulness of the current experimental data for meso-scale flow boiling heat transfer in the low mass flux regime.

3.7 Two-phase flow experimental results: Long-term performance evaluation

The long-term experiments were run for 8 hours every day for a period of 15 days or a total of 120 hours actual operation time. However, initial data were removed from each set as explained below and the results for 105 hours of operation are shown in this paper. The EHD pump was operated at a fixed voltage of 1200V and this was not changed for the duration of the tests. The evaporator heater voltage was adjusted to ensure that full phase-change was taking place inside the evaporator at the given flow rate produced by the EHD pump. The saturation temperature and pressure measurement at the outlet of the evaporator confirmed the thermodynamic state of the fluid. The condenser ice bath was replenished periodically to maintain a constant condenser outlet temperature. Results from a typical 8-hour test are shown next. Figure 48 shows the EHD pressure generation and flow rate and Figure 49 shows the applied EHD voltage and current. Since the EHD pump had an open channel, the pressure generation shown in Figure 48 is actually the net pressure generated by the EHD pump minus the pressure drop in the EHD pump itself and is equal to the pressure drop in all the tubing and bends in the rest of the two-phase flow loop. The gray lines represent all raw data captured every second for the 8-hour experiment; the sample rate was 1 sample/sec. The black lines in all plots are running-averages for 60 seconds, to remove noise from the data.

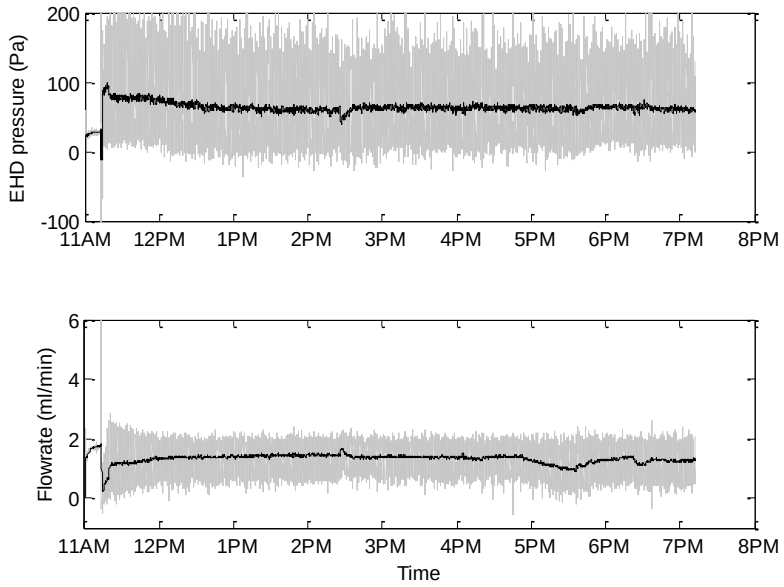

Figure 48: Typical EHD pump pressure generation and flow rate for 8-hour experiment

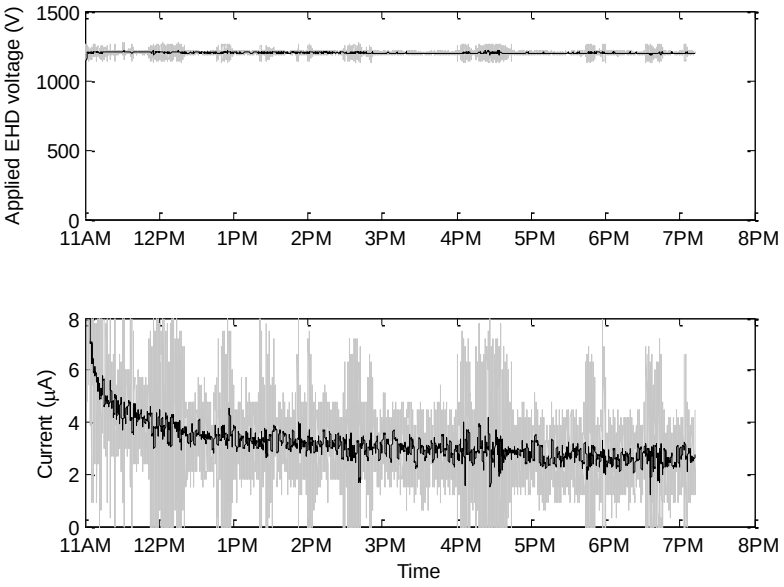

Figure 49: Typical applied EHD voltage and current for 8-hour experiment

The initial variation in the pressure and flow rate indicates the transition from single-phase to two-phase flow, i.e. there is a sudden increase in the pressure load in the evaporator for

two-phase flow and the average flow rate becomes lower as a result. This point can be seen in both Figure 48 and Figure 49. The reason for the higher pressure load is because the density difference between liquid and vapor phases is significant and this results in much higher flow velocity for the vapor. The acceleration of the flow imparts a momentum pressure drop on the system, in addition to the frictional pressure drop due to viscous forces. The overall heat transfer for this fixed applied EHD voltage ranged between 5.5-6.2W as will be shown below. The reason the heat removal varied was due to the changes in the laboratory environment temperature and this is explained in the paragraphs that follow. The heat loss to the environment was estimated from measurement of the experiment insulation surface temperature. This value was 2°C higher than the ambient temperature at its maximum. The temperature difference was used along with the outer surface area of the insulation and an estimate of the natural convection heat transfer coefficient in air to give an approximate environmental heat loss of 0.5W.

The voltage and current measurements were attained from the internal circuitry of the high voltage power supply with high accuracy, as shown in Table VII. The decreasing current was due to the purification of the fluid which is typical of the conduction phenomenon and this trend was seen every day in every 8-hour experiment. The purification is thought to result from gradual precipitation of fine particles in the working fluid. However, this phenomenon needs to be studied further before any definite conclusions can be made about the reasons for its prevalence in EHD conduction pumping.

During these long-term two-phase flow heat transport experiments the laboratory temperature could not be controlled. As the temperature increased, it caused the length required for condensation to change and this affected the pressure drop inside the condenser. Therefore the load on upstream EHD pump changed as well, which in turn affected the flow rate. As a

result there was an overall change in heat transport of the system during the course of the experiment. To estimate the effect of the change in lab ambient temperature on the two-phase flow pressure drop in the condenser, a correlation by Kim and Mudawar [81] was used which was appropriate for the range of mass flux, type of fluid and tube diameter in this experiment. The correlation was used to calculate the frictional two-phase flow pressure drop per unit length of the condenser as a function of the vapor quality. Although the two-phase flow pressure drop also contains an accelerational and gravitational component, these were not considered for the calculations. The accelerational pressure drop for condensation is negative (implying deceleration of the flow) so excluding it from this analysis simply gave a more conservative result. The gravitational component is negligible for flow through meso- and micro-channels.

For a typical two-phase flow heat transport test as shown in the above figures, the EHD pump pressure was ~100 Pa. The evaporator pressure drop was measured (not shown here) to be ~80 Pa, indicating that the highest pressure drop in the loop generally occurred in the evaporator. The inner diameters of the EHD pump, evaporator and condenser were 1 mm, 1.5 mm and 5.33 mm, respectively. Since pressure drop in a circular tube scales with diameter as $\Delta p \sim 1/D^5$, the pressure drop in the condenser and the rest of the loop was assumed to be negligible compared to the evaporator for the most part. However, the correlation calculations in [81] indicate that the two-phase frictional pressure drop in the condenser was found to be as high as 60 Pa if the entire length of the condenser was required. As mentioned above, when the laboratory temperature increased, the condensation length was changed. Using a simple energy balance calculation, this length actually decreased with increasing laboratory temperature, i.e. the condensation rate improved as the lab temperature increased. The reduced length was used to calculate the new pressure drop in the condenser and according to the correlation, it decreased by as much as 50%.

These results were more consistent with the actual measurements of upstream EHD pump pressure and evaporator pressure drop and they support the argument that the condenser conditions had a significant effect on the upstream EHD pump performance. They also explain why the overall heat transport rate was altered by the laboratory ambient temperature (which could not be controlled) during the course of the experiment. It should be noted that there was a definite lower limit of 5W of heat transport capacity for the entire experiment and the heat transport did not fall below this value.

The temperature variation for the 8-hour experiments is shown in Figure 50. The inlet and outlet temperatures are for the fluid bulk and were measured using probes inserted into the flow channel. Wall temperatures were measured using wire thermocouples soldered to the evaporator outer wall surface. In Figure 50 only two out of seven wall temperatures are shown simply to illustrate typical changes. As explained in the experimental setup, due to the small tube wall thickness, low heat flux and high thermal conductivity of the copper tube, the outer wall temperature of the evaporator was assumed to be equal to the inner wall temperature for this experiment.

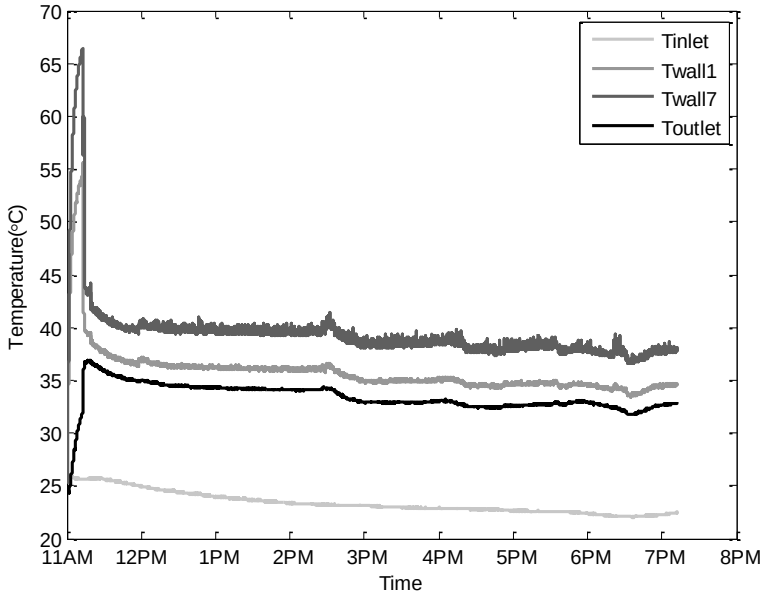

Figure 50: Typical temperature variation for 8-hour experiment

As in the previous plots, the initial cycling of the temperatures in the initial period of the experiment corresponds to the transition between single-phase and two-phase flow. After the first hour, conditions were steady and the energy balance was maintained. The evaporator outlet saturation temperature was 2°C superheated above the saturation temperature corresponding to the measured saturation pressure, indicating that the flow was exiting the evaporator as a slightly superheated vapor. In order to illustrate pump performance over 15 days, averages of each daily 8-hour experiment were combined and these results are shown in Figure 51, Figure 52 and Figure 53. During phase change experiments, temperature, pressure drop and flow rate oscillated about a mean value. Steady state was defined as the condition where the mean wall/saturation temperature, pressure drop and flow rate did not change by more than 0.5°C, 10 Pa and 0.2 ml/min. For this reason, the first hour of data were removed from each day since the system took some time to reach a steady-state condition. Therefore averages of 7 hours of data were taken and the total running time for steady-state, intermittent operation was 105 hours, as stated above.

Figure 51 shows the EHD pressure and flow rate and Figure 52 shows the applied EHD voltage and current.

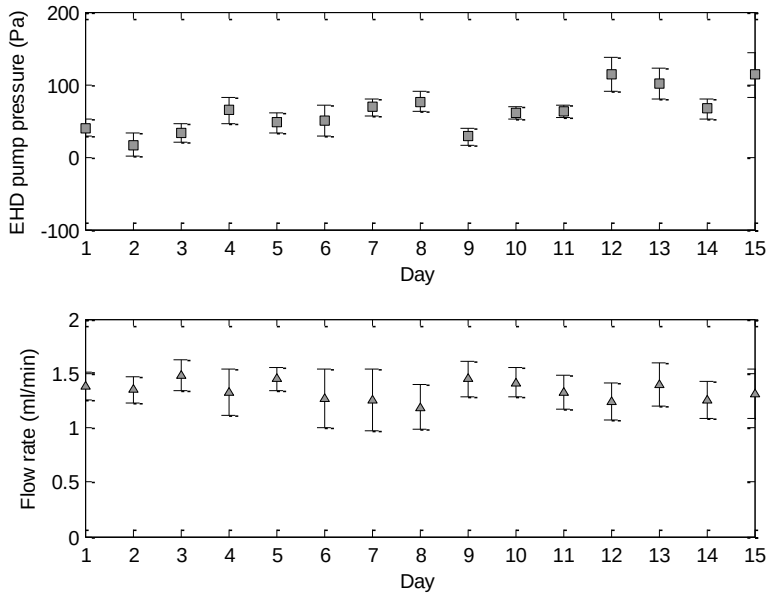

Figure 51: EHD pump pressure and flow rate averaged over 7 hours/day for 15 days

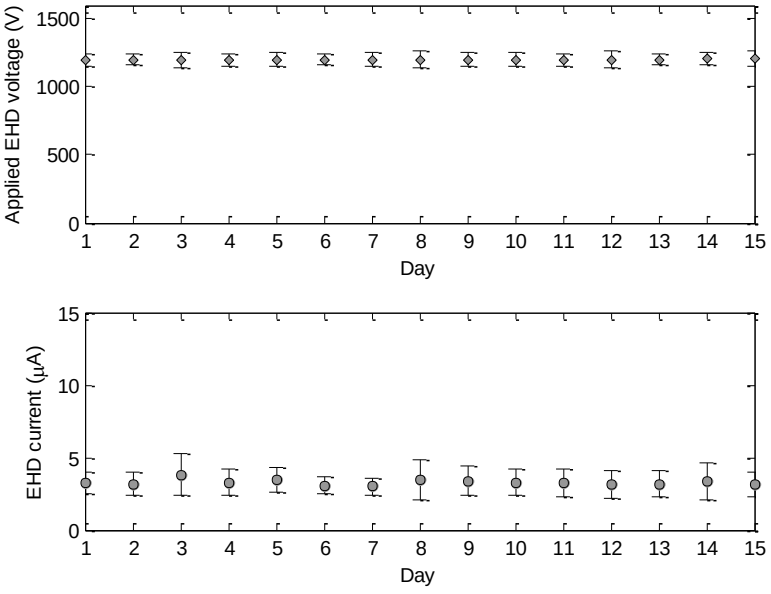

Figure 52: Applied EHD voltage and current averaged over 7 hours/day for 15 days

The results indicate that EHD pressure appeared to change over the course of the experiments and as indicated above, the reason for this was the variation in the downstream condenser pressure drop, which was affected by the laboratory ambient temperature and could not be controlled. Therefore, as the experiment was run for several days with variation in the lab ambient temperature, the net pressure generation in the EHD pump changed accordingly. All other quantities were quite stable and changed very little for the 105 hours of operation. The average volumetric flow rate over 105 hours was 1.36 ml/min which corresponded to a mass flux of 17.5 $kg/m^2 \cdot s$ in the evaporator (i.e. the mass flow rate divided by the evaporator cross-sectional area). From the current and voltage measurements, the EHD pump required approximately 0.0042W of power on average to operate. The system was able to remove a minimum of 5W as stated above which is three orders-of-magnitude higher than the required input power. The average heat removal rate is compared to the average EHD pump input power in Figure 53. The heat removal rate was the product of the measured mass flow rate and latent heat of vaporization value in Table VI. Using this method to measure heat removal was possible because of the confirmation of full-phase change occurring in the evaporator. This was in turn supported by the determination of the precise thermodynamic state of the fluid exiting the evaporator, as mentioned above. It should be noted that the y-axis of the top graph is in units of Watts while the y-axis of the bottom graph is in units of milli-Watts, which highlights the minimal power requirement of this EHD-driven two-phase flow heat transport device.

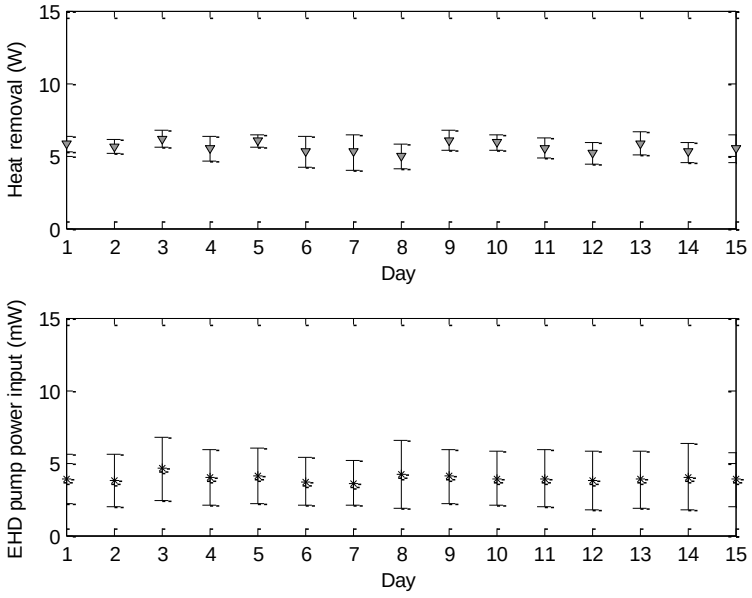

Figure 53: Heat removal rate for full phase change in evaporator and EHD pump input power averaged over 7 hours/day for 15 days

As with the flow rate measurements in Figure 51, the heat transport in Figure 53 was very reliable over 15 days of operation and there was no degradation in performance at all. This also means that the continuous application of the electrical field on the refrigerant HCFC-123 for over 105 hours did not alter its heat transfer characteristics.

3.8 Conclusions

A meso-scale, active two-phase flow heat transport device driven solely by EHD conduction pumping was developed and its heat transport capacity was determined. The 1 mm diameter open-tube EHD pump was able to consistently generate both single- and two-phase flows through a 1.5 mm diameter evaporator tube and maintain the heat transport capability. The system was able to transport 7.3W of heat with just 0.015W power input to the EHD pump (although much higher heat transport and mass flux could be achieved with the addition of

electrode pairs in the EHD pumping section). The system was also able to successfully recover from evaporator dryout and lower the evaporator wall temperatures. This type of recovery was achieved for the first time in meso-scale, for an EHD-driven two-phase flow heat transport system. The single- and two-phase flow pressure drop measurements also led to a new and improved understanding of net EHD pump pressure generation.

The low mass fluxes generated by the EHD pump made it possible to measure the in-tube, local flow boiling heat transfer coefficients as a function of vapor quality along the evaporator length. The experimental data for heat transfer coefficient as a function of vapor quality had a similar trend to other experiments at higher mass fluxes in the literature for meso-scale in-tube flow boiling. This work provided limited but useful data points at very low mass fluxes and a comparison was also made with two correlations for which the operating conditions fell outside their acceptable regions.

In addition to the above results, the EHD conduction-driven two-phase flow heat transport system was tested successfully for 105 hours of intermittent operation. The EHD pump was the sole driving mechanism and allowed the system to function for 15 days without failure, despite the challenges presented by the highly dynamic nature of two-phase flow heat transport. The performance evaluation indicated that a minimum of 5W of heat transport was achieved consistently and the system only consumed 0.0042W of power which was 0.084% of the heat transport capability. The two-phase flow pressure drop in both the evaporator and condenser downstream of the EHD pump played an important role in the heat transport performance. These were quantified using measurements and an appropriate two-phase flow pressure drop correlation and provided valuable information for design of small-scale EHD-driven two-phase flow heat transport systems. The results strongly support the long-term application prospects for

this technology and are a contrast to simple short-term tests which are conducted for purely research purposes in the laboratory.

CHAPTER 4 – ELECTRICALLY DRIVEN LIQUID FILM FLOW BOILING IN THE PRESENCE AND ABSENCE OF GRAVITY[3]

4.1 Introduction

As described in the initial literature review section, liquid film flow boiling is an excellent heat transfer technique which has a great potential for both terrestrial and micro/zero-gravity thermal control applications. However, it cannot be sustained in micro-gravity as the hydrostatic pressure is not present to drive surrounding liquid to re-wet the heater surface. In addition, the buoyancy force that drives bubble motion during the nucleate boiling phase is also absent. Bubbles remain on the surface (this has been demonstrated experimentally for pool boiling as discussed) and cause high levels of superheat at various locations. The heater surface dries out and temperature rise is unbounded, leading to failure of the heat transport system.

While it is impossible to easily reintroduce hydrostatic pressure in micro-gravity to drive liquid film toward the heater surface, an electrical field can be used to pump the dielectric liquid in a relatively simple manner. The studies described in the literature review involved using the so-called dielectrophoretic force to enhance boiling heat transfer in micro-gravity. However, these studies were in pool boiling in micro-gravity, where expansion of vapor in the boiling chamber was compensated by bellows and it was hard-filled with liquid initially. They focused on using the DEP force to enhance vapor bubble removal. On the other hand, the aim of this work is to study EHD conduction-driven liquid film flow boiling with a vapor space above the liquid-vapor interface in micro-gravity via parabolic flight experiments. This electro-wetting approach is a unique concept and the objective of this work is to provide basic and practical understanding of EHD conduction pumping of a liquid film in the presence of boiling in a micro-

[3] The work in this chapter is currently under peer review for journal publication in [82] and [83].

gravity environment. Furthermore, these parabolic flight experiments are to serve as an important stepping-stone toward detailed experimental work in a continuous micro-gravity environment on board the International Space Station. Beyond the scientific understanding of the EHD conduction-driven liquid film flow boiling, the ultimate goal is to develop two-phase heat transport devices for micro/zero-gravity environments based on EHD technologies.

4.2 Terrestrial and micro-gravity EHD-driven liquid film flow boiling study on bare heater surface

4.2.1 EHD pump substrate disc design

The EHD conduction pump was fabricated by lithographically printing electrodes onto a substrate disc to pump liquid film. The original design and fabrication was done by Pearson and Yagoobi [44]. Design B (as shown in Figure 25 and Table IV) was used for the experiments in this chapter. The substrate disc was made of 96% alumina with a diameter of 152.0 mm and thickness of 1.0 mm. Alumina was chosen because it had low electrical conductivity ($<10^{-12}$ S/m) but relatively high thermal conductivity (25.0 W/m·K). Electrode traces were made of Palladium-Silver (Pd-Ag) and printed onto the surface of the substrate in pairs. Each pair consisted of a narrow electrode (connected to ground) and wide electrode (connected to high voltage) with a space in between. A total of 14 electrode pairs were printed on the substrate, with each pair decreasing in diameter near the center of the disc, where a heater was installed. The heater substrate was also made of 96% alumina with a diameter of 22.0 mm and thickness of 1.0 mm. Bus lines for electrical connections to the electrodes were also printed on the disc. The electrode disc and heater are shown in Figure 54 and electrode dimensions are shown in Figure 55. The dimensions and spacing between electrodes and electrode pairs were based on detailed numerical solutions of the governing differential equations for the electrical field, charge

conservation and fluid flow [19]. The EHD conduction pump was designed with 14 electrode pairs in order to provide sufficient liquid flow to the heater at the maximum heat flux.

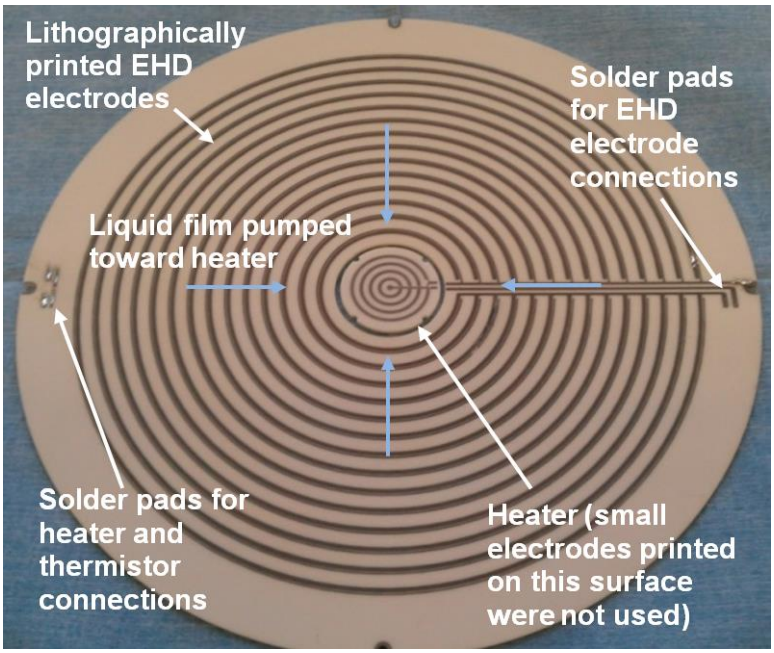

Figure 54: Ceramic substrate electrode disc with lithographically printed electrodes and heater at center

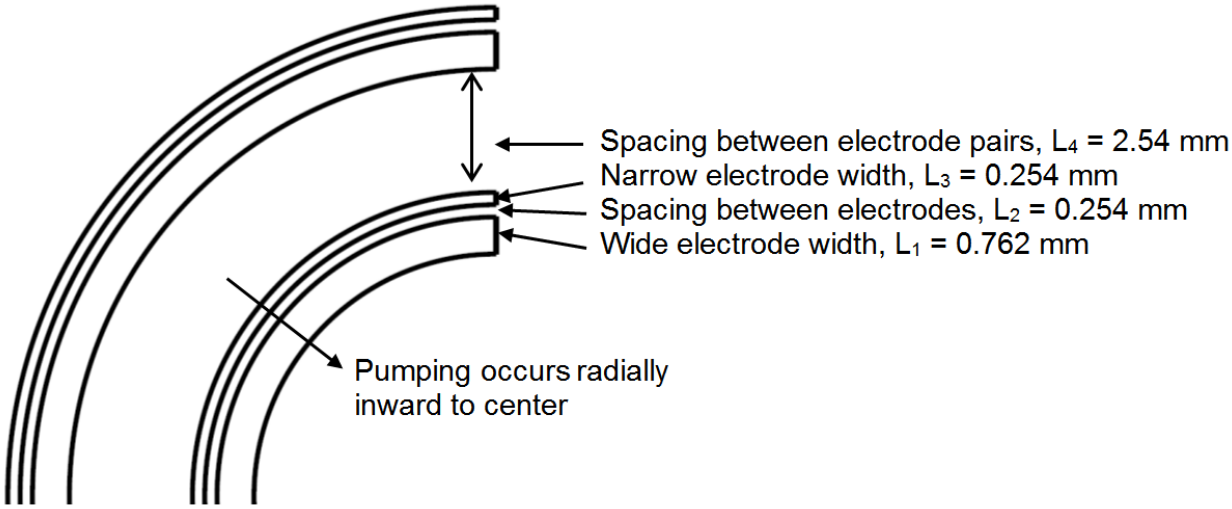

Figure 55: Schematic showing electrode dimensions and spacing between electrode pairs for EHD liquid film pump in chapter 4

The heater was fabricated by printing a 10.0 mm × 10.0 mm, 300 Ω resistor onto the bottom surface of the substrate. A 1.3 mm × 1.3 mm thermistor was printed over the heating resistor (with a 20μm-thick electrical insulation layer in between) for heater surface temperature measurement. The bottom of the heater assembly is shown in Figure 56 with details of the printed heater and thermistor. Since a square printed resistor was used for the heater on the circular ceramic substrate, a numerical simulation was used to obtain the averaged heat flux and temperature on the top surface of the heater in direct contact with the working fluid. This is described in detail in Appendix B.2. Bus lines for the heater and thermistor ran along the bottom surface of the substrate disc to the periphery, and passed through electrical vias to solder pads located on the top surface, to which connecting wires could be soldered. The electrodes, heater, thermistor, insulating layers and associated bus lines were all printed using thick film fabrication methodology.

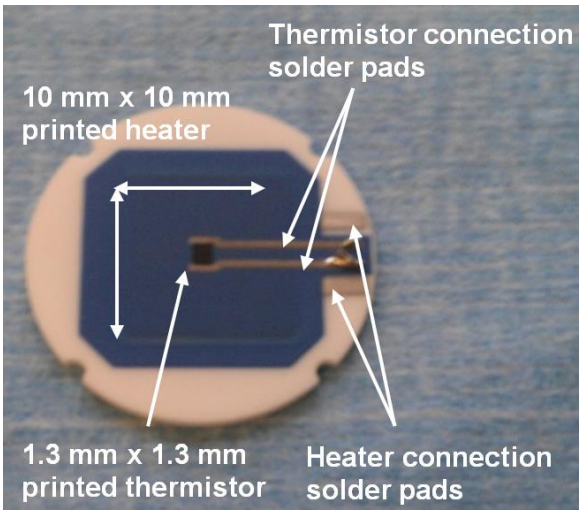

Figure 56: Bottom of heater piece showing printed resistance heater and printed thermistor for heater surface temperature measurement

4.2.2 Experiment housing design and flight rack

The experiment housing was a cylindrical tank made of aluminum, with a high-strength glass lid and two chambers. The chambers were separated by a removable aluminum interface plate which was sealed with O-rings. The electrode disc and heater shown in Figure 54 were epoxied onto the interface plate and installed into the tank. The top chamber contained the working fluid, refrigerant HCFC-123. Its properties are given in Table VI. The working fluid was boiled on the heater surface and condensed on the outer periphery of the electrode disc surface, where EHD conduction pumping was used to drive it toward the heater at the center. Heat was dissipated through the electrode disc and interface plate to the bottom chamber of the tank where cooling water flowed from a recirculating chiller. The working fluid and cooling water never mixed as both chambers were perfectly sealed. In order to ensure that there was no heat loss through the bottom surface of the heater, a Delrin insert was used as a thermal insulator. The thermal conductivity of Delrin is 0.33 W/m·K and at the maximum heat load of 30W the heat loss was estimated to be 1W, corresponding to less than 3% loss of power below the heater.

Various electrical, sensor and fluid connections for the experiment housing are shown in Figure 57. The high voltage and ground feedthroughs were used to connect the electrodes on the disc surface to the high voltage power supply. The wires were soldered onto the pads shown on the right in Figure 54. The high voltage wire was connected to the solder pad and common bus line of the wide electrodes, while the ground wire was connected to the common bus line of the narrow electrodes. The connecting wires for the heater and thermistor were soldered onto the pads shown on the left in Figure 54. High current-carrying wires were used for the heater power connections and this wire pair also had a separate feedthrough. Smaller gage low-voltage wires were used for the thermistor connections. An RTD probe was inserted through a port in the side

wall of the housing to measure vapor temperature of the refrigerant (saturation temperature was elucidated from this) just above the heater surface. The tip of the RTD probe was approximately 12 mm above the heater surface. An absolute pressure transducer was used to measure vapor pressure of the refrigerant via another port in the experiment housing. These two measurements confirmed matching of the saturation pressure and saturation temperature in the vapor phase. Two RTD probes were also inserted prior to the recirculating chiller connections to measure the cooling water temperature at the inlet and outlet.

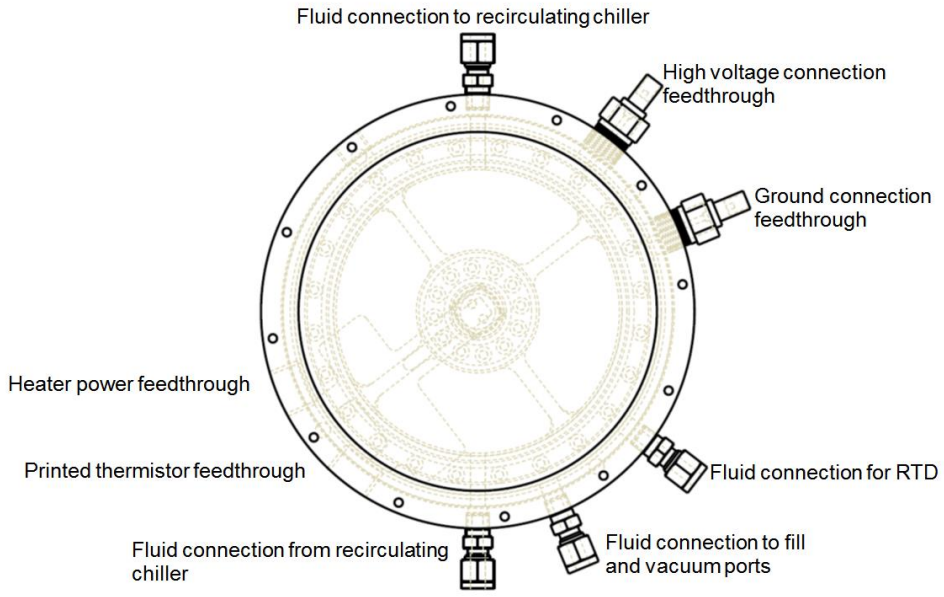

Figure 57: Experiment housing showing fluid, sensor and electrical connections

The layout of the flight experiment was in a vertical configuration within a Vertical Equipment Rack, shown in Figure 58, which housed the experiment base plate and associated hardware (gray, middle), two power supplies (green and red), one data acquisition unit and one notebook computer. The recirculating chiller (blue) was mounted at the bottom of the Vertical Equipment Rack.

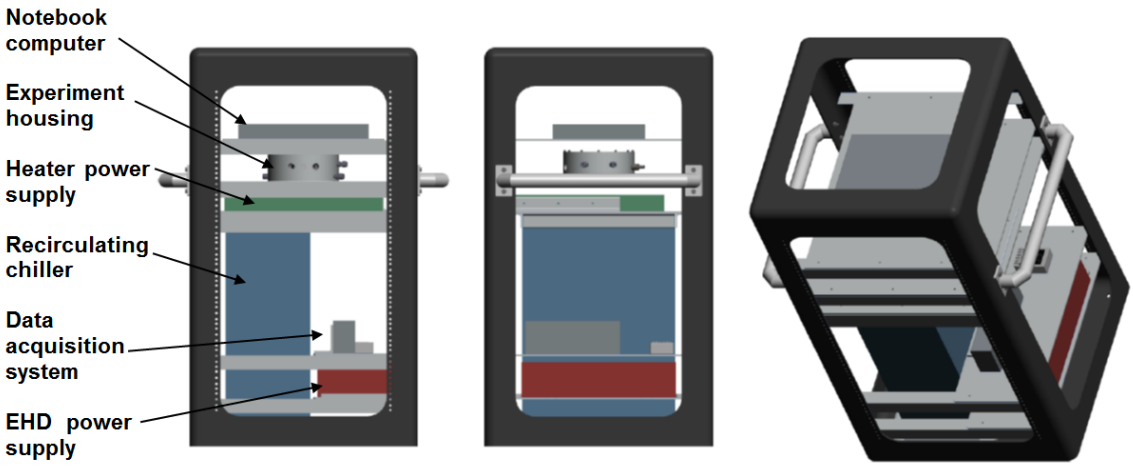

Figure 58: Layout of hardware in Vertical Equipment Rack for variable gravity flight

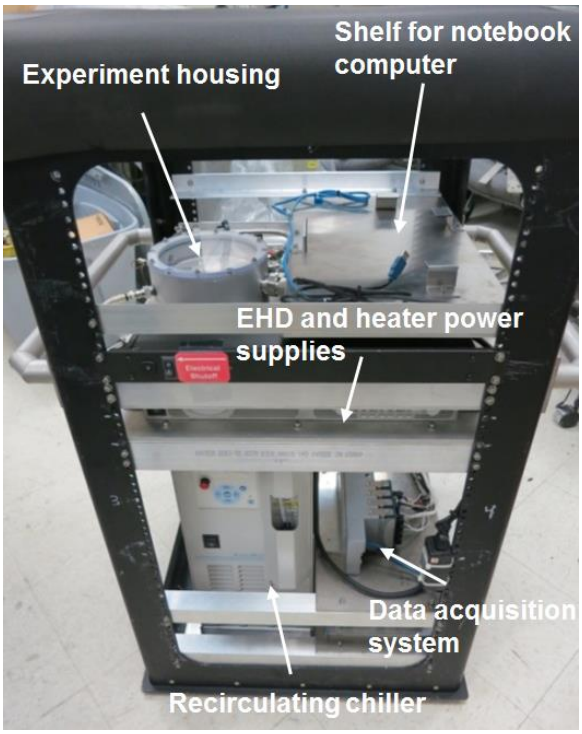

Figure 59: Photograph of completed flight experiment rack

A photo of the completed rack is also shown in Figure 59. The only missing component is the notebook computer for data acquisition which was installed on the top plate above the experiment. The following measurements were recorded during testing: temperature from

thermistors and RTDs, absolute pressure of the fluid (Omegadyne PX19), acceleration due to gravity (NASA PAAMS with NI USB 6259), applied EHD pump voltage and corresponding electric current (Trek 677B). An Accel 250 LC cooling/heating recirculating chiller from Thermo Scientific controlled the condenser temperature of the experiment housing. A TDK Lambda GEN150-10 power supply provided power to the heater located at the center of the electrode disc. Data were acquired using the National Instruments USB Compact DAQ 9188 system. A National Instruments (NI) GPIB-USB-HS controller, connected to the notebook computer running NI LabVIEW virtual instrument software, allowed users to control the loop. The systematic errors in all measurements and maximum uncertainty of derived quantities are given in Table IX.

Table IX: Maximum systematic error of various measurement devices and experimental uncertainty for chapter 4, section 4.2

Measurement	Maximum systematic error
Temperature	±0.3°C
Applied voltage to EHD electrodes	±2 VDC
Current measured through EHD electrodes	±5 μA
Applied voltage to heater	±0.017 V
Current measured through heater	±5 mA
Absolute pressure	±275 Pa
Acceleration due to gravity	±0.02 g
Derived quantity	**Maximum uncertainty**
Superheat, ΔT	±0.42°C
Heat flux, q”	±1.5%

4.2.3 Experiment procedure during flight

The aircraft achieved variable gravity by performing parabolic maneuvers as discussed in the previous chapter. The parabolic maneuvers began with a 1.8-g pull-in, followed by approximately 20 seconds of 0-g, and terminated with a 1.8-g pull-out, as shown in Figure 41. The parabolas were flown in four sets of 10 per flight in general and four flights were flown in total, over a period of four days. The acceleration due to gravity was monitored using an accelerometer.

Prior to the start of the parabolic maneuvers, the chiller temperature was set and the chiller working fluid (distilled water) circulated through the condenser on the experiment loop, thus setting the saturation condition of the experiment, which matched thermodynamic data available for HCFC-123 [64]. The potential applied to the EHD conduction pump was set to 750 VDC in 250 VDC increments. This was a safe potential at which EHD conduction began and fluid motion was visible. Although the flow rate could be increased by increasing the applied potential, there was a risk of arcing at potentials exceeding 1200 VDC. Next, the heat flux was set by increasing the applied voltage to the heater. When the parabolic maneuvers began, the heat flux was kept constant until sufficient data were acquired (data were acquired and averaged over several parabolas). This was repeated with several values of heat flux, with and without the EHD pump activated, to make a comparison between the two cases.

4.2.4 Terrestrial results

Terrestrial experiments in liquid film flow boiling were conducted prior to the parabolic flight experiments which are presented in the next section. The experiment chamber was first evacuated and charged with a fixed amount of refrigerant HCFC-123 which resulted in a liquid film 2.0 ± 0.3 mm thick above the electrode disc and heater surface. The recirculating chiller was

set to a fixed temperature and the system was allowed to reach steady state (this was the point at which the saturation temperature and heater surface temperature did not fluctuate by more than 0.1°C/min about the mean value). Once the saturation temperature and pressure matched values from thermodynamic tables for pure HCFC-123, a potential of 0.75 kV was applied to the high voltage EHD electrodes. This caused the liquid film to be pumped from the periphery of the disc toward the heater at the center (the pumping was visible in the form of small ripples on the liquid surface). Next, power was applied to the electric heater. Applied voltage and current were measured to calculate heater power and this was divided by the heater surface area to give heat flux.

Heat flux was incremented initially by 0.25 W/cm^2 until 5.0 W/cm^2 was reached. After this point, it was incremented by 0.5 W/cm^2 until the critical heat flux was reached. The time between heat flux increments was 300 seconds, which allowed the surface temperature to reach steady state (defined above). Two separate tests were run; once with the EHD pump activated (referred to as the EHD case with 0.75 kV applied potential) and once without the EHD pump activated (referred to as the no-EHD case with 0 kV applied potential). The results of these two tests are shown in Figure 60. Heat flux is shown on the y-axis and heater superheat, or ΔT, is shown on the x-axis. The latter is the difference between the heater top surface temperature (defined previously) and the saturation temperature measured above the heater, i.e. $\Delta T = (T_{top\_surface} - T_{sat})$. The error bars show the standard deviations of measured values of ΔT (based on 60 measurements for each data point). At heat flux levels approaching the Critical Heat Flux (CHF), errors became large because of the sudden and rapid increase in surface temperature. Vertical error bars for heat flux are not shown since heater power variation was too minimal to be visible in the graph.

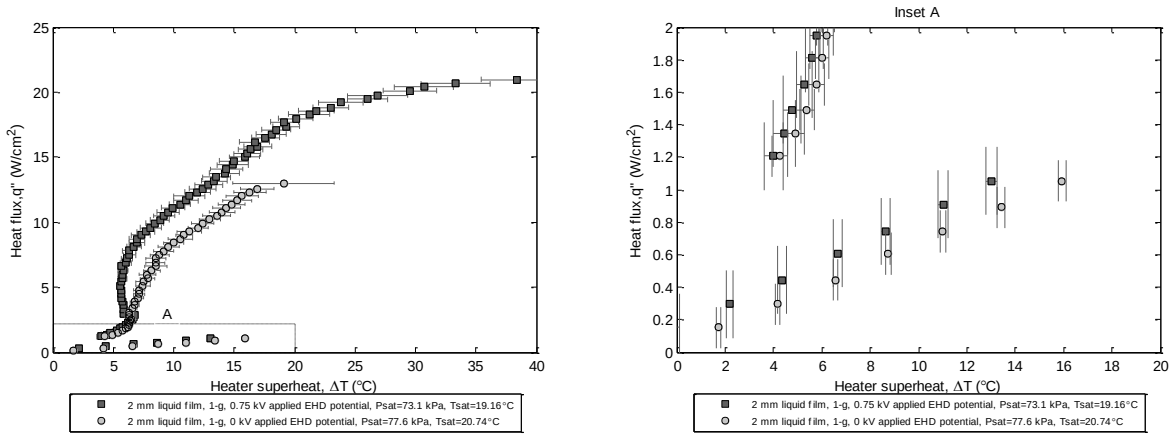

Figure 60: Terrestrial results for liquid film flow boiling with and without EHD conduction pumping of liquid film

As illustrated above, activation of the EHD pump had an effect on both the critical heat flux and the superheat. Both the EHD and no-EHD cases showed significant hysteresis at low heat fluxes. At a heat flux of 1.05 W/cm^2, superheat was reduced by 2.9°C in the EHD case compared to the no-EHD case, as shown in Figure 60 (Inset A). Nucleate boiling began at a heat flux of approximately 1.2 W/cm^2. As the heat flux was increased, the two boiling curves diverged. For example, at a heat flux of 10.0 W/cm^2, the corresponding superheat decreased by 3.9°C with EHD pumping activated. The reason for the lower superheat with EHD for a given heat flux is explained as follows: For the 2.0 mm liquid film in these experiments, hydrostatic pressure in the liquid was 30 Pa. The hydrostatic pressure caused the liquid film to flow and wet the heater surface during the boiling process. However, when the EHD conduction pump was activated, the electric body force produced by the strong electrical field (at applied potential of 750 V) resulted in pressure generation of 265 Pa, (approximated from other experimental measurement in [31, 62]) which was significantly greater than the hydrostatic pressure alone. This resulted in a higher flow rate of liquid to the heater surface and produced significant

circulating velocities in the liquid as well. Therefore, the increased liquid flow rate to the heater in the EHD case compared to the no-EHD case improved boiling heat transfer above the heater surface and lowered the superheat for a given heat flux.

The activation of the EHD conduction pump also led to enhancement in critical heat flux. In the no-EHD case, when the applied heat flux was close to CHF, rapid formation of vapor bubbles on the heater surface resulted in columns of vapor which eventually coalesced. At this high rate of vaporization, the hydrostatic pressure in the liquid film surrounding the heater was insufficient to maintain the liquid flow rate to wet the heater surface. Heat transfer deteriorated significantly as a result and when the critical heat flux was reached, even a small increase of 0.1 W/cm^2 caused the superheat to increase by more than 35°C per second. The CHF for the no-EHD case was 13.0 W/cm^2 (at this heat flux in the EHD case, the superheat was already lower by 6°C). For the EHD case, however, the increased liquid flow rate due to the EHD pump was effectively able to increase the critical heat flux to 20.9 W/cm^2 or 62% higher than the no-EHD case. The terrestrial results were also compared to previous similar experiments in EHD-driven liquid film flow boiling by Pearson and Yagoobi [44]. The observed differences in CHF and ΔT for the operating conditions studied were due to: (a.) EHD Electrode designs and spacing between electrode pairs that were studied in [44] were larger than those in the present work (dimensions were exactly double of those shown in Figure 55) and (b.) Both experimental setups were slightly different and heat losses beneath the heater were not compensated for in [44]. Nevertheless, the results of both experiments were based on comparing EHD and no-EHD cases and thus, the actual values of heat flux were not as important. Overall, these results demonstrate the great potential for EHD conduction pumping of the liquid film to facilitate liquid film flow boiling in the presence of gravity. More importantly, in the absence of gravity there will be no

hydrostatic pressure present to drive the liquid toward the heater; however, EHD pumping of the liquid film will function in the presence and absence of gravity.

4.2.5 Parabolic flight results

The same procedure used for terrestrial tests was followed for the parabolic flight test. However, because of limitations on the number of parabolas and flight length, only four heat fluxes were tested in micro-gravity (as opposed to as many as 80 heat fluxes in terrestrial tests shown in Figure 60). The video recordings of the EHD-driven liquid film flow boiling were made for the duration of the flight. The first 30 minutes of the parabolic flight test are shown in Figure 61 to give an example of the data acquisition timeline. When the aircraft was in level flight and terrestrial gravity (i.e. 1-g; variations during 1-g seen in the graph are due to turbulence during the flight), the recirculating chiller was activated. Next, the EHD pump and heater were activated; the ramp-up in applied potential to the EHD pump and applied power to the heater can be easily seen in the graph. As expected, the heater superheat or ΔT increased as soon as power was applied to the heater. The data acquired for 3 parabolas are illustrated in Figure 61. This process was repeated for heat fluxes of 1.7, 3.0, 4.2 and 5.5 W/cm^2 for both EHD and no-EHD cases.

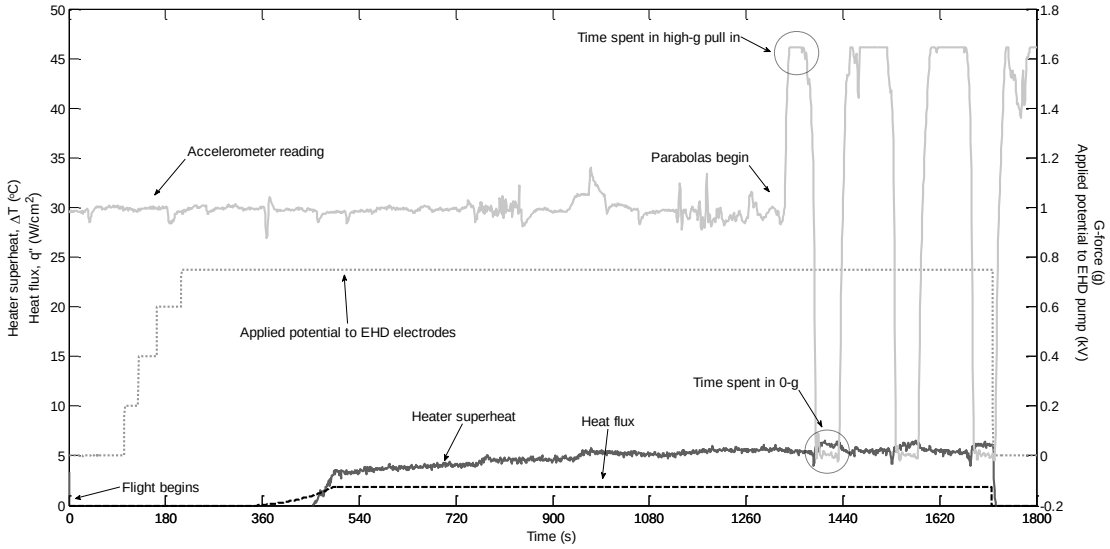

Figure 61: Parabolic flight results for liquid film flow boiling for first 30 min, showing first three parabolas

The average time spent in 0-g was between 20-30 seconds per parabola. In addition to this, periods of ~1.8g were also experienced during the pull-in and pull-out phases (described above) of the parabola and these are indicated in Figure 61 as well. To illustrate the liquid film boiling data, heat flux and ΔT were averaged over these times (and averaged again over two parabolas each for a given heat flux) for both the EHD and no-EHD cases. They were averaged over two parabolas because each operating condition was conducted for two consecutive parabolas. The averages are plotted in Figure 62 to show the effect of the EHD conduction pumping in micro-gravity liquid film flow boiling.

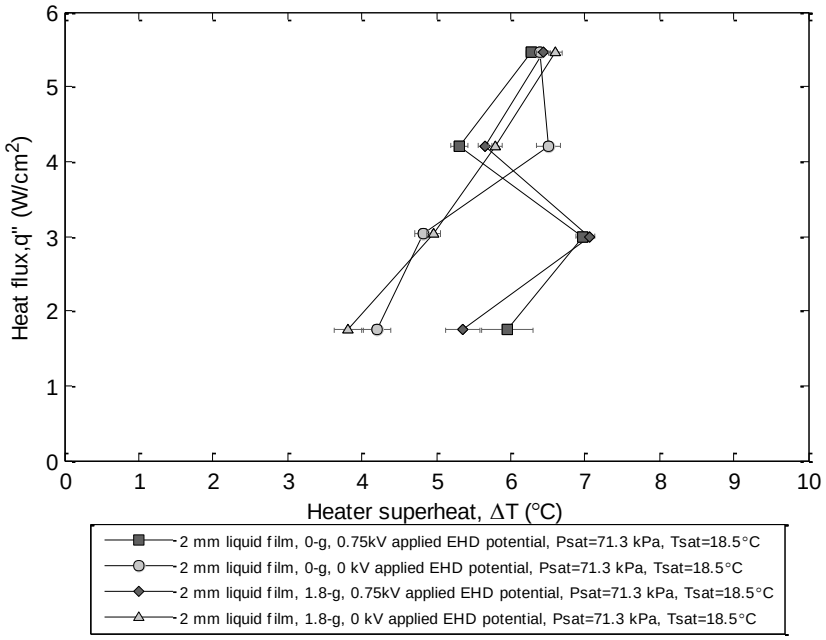

Figure 62: Parabolic flight results for liquid film flow boiling: average data for 0-g and 1.8-g

Observations during 1.8-g and transition into 0-g: The above results and corresponding discussion were substantiated with observations via nominal-speed video recording. For a given parabolic maneuver, as the aircraft transitioned from the 1.8-g pull-in phase into 0-g, there was a brief negative g-force (see Figure 61). This caused a portion of the liquid film on the EHD electrode disc surface to lift off and float in the vapor space. However, as the recirculating chiller was running continuously at a fixed setpoint, the disc surface temperature was low enough compared to other surfaces in the chamber (aluminum walls and glass lid) to facilitate condensation. Thus, some liquid remained on the disc surface, which was then pumped toward the heater by the EHD conduction pump. A thin liquid film was observed on the heater surface, even at higher heat fluxes when bubble nucleation had begun. As the aircraft transitioned from 0-g to the 1.8-g pull-out phase, there was another brief period of negative g-force which can also be seen in Figure 61. The floating liquid was rapidly pushed against the glass lid where large

droplets formed (droplet size was on the order of 5 mm). During the 1.8-g pull-out, the liquid droplets then moved quickly across the glass surface towards the chamber wall and flowed back down to the disc surface where the liquid film formed. This sudden influx of liquid during the 1.8-g pull-out phase strongly affected the temperature of the heater surface, as it further increased the liquid flow rate in addition to the EHD-generated flow (see Figure 62).

Superheat measurements at 1.7 W/cm^2 and 3.0 W/cm^2 during 0-g and 1.8-g: The results indicate that for the no-EHD case at heat flux of 1.7 W/cm^2, nucleate boiling had already initiated (bubbles were observed on the heater surface in 0-g and 1.8-g). Although bubbles formed in 0-g, they did not quickly detach from the heater surface. Instead they appeared to remain on the surface and grew in size, as they were fed by vapor. The superheat was approximately 4.2°C during 0-g and 3.8°C during 1.8-g. The slightly lower superheat during 1.8-g was attributed to the surge in liquid on the disc surface during the 1.8-g pull-out phase of the parabolic maneuver, as described above. The flow inertia from the surge also forced bubbles away from the heater surface and allowed for new bubbles to form. For the EHD cases at the same heat flux, the superheats were actually higher than during 0-g and 1.8-g, as seen in Figure 62. The reason was as follows: in the no-EHD cases, the flow regime at this heat flux was in the low range of nucleate boiling and heat transfer occurred with lowered superheat. For the EHD cases, the flow regime remained in forced convection, due to the much higher heat transfer coefficient with EHD, delaying the onset of nucleate boiling point. Thus, for the same heat flux, the superheat was higher in the EHD cases compared to the no-EHD cases. It is important to highlight that for the EHD cases at 1.7 W/cm^2, the ΔT was also lower by 0.6°C during 1.8-g compared to 0-g. This was due to the superposed forced convection from gravitational and EHD forces during 1.8-g vs. solely forced convection from EHD forces during 0-g. The superheat

increased when the heat flux was increased to 3.0 W/cm^2 for all cases. However, the nucleate boiling regime still had not initiated in the EHD cases. The results also give an indication of how much higher the heat transfer coefficient was for the nucleate boiling regime compared to that during the EHD-generated forced convection regime at 1.7 W/cm^2 and 3.0 W/cm^2.

Superheat measurements above 3.0 W/cm^2 during 0-g and 1.8-g: Above 3.0 W/cm^2, nucleate boiling regime began in the EHD cases. The heat transfer was improved significantly and the superheat was lowered immediately to below that of no-EHD cases, as illustrated in Figure 62. In this region the activation of the EHD pump caused liquid to be pumped towards the heater where the flow inertia was able to effectively displace bubbles that had formed on the surface. The introduction of fresh liquid led to lower surface temperature (and ΔT) and allowed for formation of new bubbles. At the heat flux of 4.2 W/cm^2, the maximum difference in superheat between the EHD and no-EHD cases during 0-g was 1.2°C. As the heat flux was increased to 5.5 W/cm^2, the EHD cases still showed lower ΔT than the no-EHD cases. However, the trend in the data indicates that if the heat flux was extended beyond 5.5 W/cm^2 the effect would have diminished and all results (i.e., EHD, no-EHD, 0-g, and 1.8-g) would converge. It was apparent that the strong effects of the 1.8-g phases of the parabolic maneuvers were carried over even through the transition into 0-g. The transitions were an unavoidable feature of the parabolic flight. However, the results also showed that if the system was given time to approach steady-state in a true 0-g environment (without such sudden transitions in g-force), the heater surface would have eventually dried out in the absence of EHD-generated flow. This transient nature of the results is discussed next.

Flight conditions: It is important to mention that the unsteady nature of the parabolic flight meant that the measured parameters did not approach steady-state. Therefore, all reported

results are transient. As stated above, the required time constant for achieving steady-state in terrestrial tests was ~300 seconds. Even though the total parabolic flight time was 2 hours, the time spent in micro-gravity per parabola was only between 20-30 seconds which was not enough to reach steady-state conditions. The time spent in the 1.8-g phases that preceded and followed every phase of 0-g also affected the results. The system did not have enough time to recover from this phase before the next zero-gravity condition was reached. The parabolic flight environment was also relatively harsh compared to the terrestrial laboratory. Significant vibrations were present (these were exacerbated when the aircraft experienced turbulence) as well as moderate changes in cabin temperature as the flight altitude changed. The effect of vibrations was most apparent during the brief periods of 1-g in the flight. The superheat measurements at low heat flux were similar to those in the lab experiments at the same heat flux, but at higher heat flux the superheat became lower (see Figure 60 and Figure 62). This was attributed to so-called g-jitter which assisted in transporting bubbles away from the heater surface and improved heat transfer, thereby lowering temperature.

In addition to the above, the design of the EHD conduction pump was not optimized. With the addition of more electrode pairs, higher pressure generation (and therefore, higher flow rate) can be achieved, which can result in greater enhancements in pool boiling critical heat flux. Much better results can be also obtained simply by increasing applied potential to the EHD pump from 750 V to 1000 V, for example (this was not done during the flight for safety and lack of time reasons, but a maximum of 1200V applied potential is possible with this electrode design before arcing between electrodes becomes an issue). The pressure generation would have increased from approximately 265 Pa to 370 Pa, based on experimental data [31, 62] , resulting in significantly higher heat transport capacity with the existing design. The power input for the

EHD pump was minimal as well. For terrestrial tests, at the applied potential of 750 V, the maximum measured EHD current was 0.25 mA. This resulted in a power input of 0.19 W, compared to a 13.3 W increase in the heat transport capacity that was achieved (13.3 W is the difference in heater power at critical heat flux for the EHD and no-EHD cases). Therefore, the ratio of power input for the EHD pump to heat transfer enhancement was 1:70. For the parabolic flight tests, the power input for the EHD pump was the same as terrestrial experiments. Although the maximum applied heater power for the parabolic flight experiments was 9.0 W (and hence the heat flux was 5.5 W/cm^2), the actual maximum power and corresponding critical heat flux in true micro-gravity conditions during liquid film flow boiling facilitated by EHD conduction is expected to be higher, with similar minimal power input for the EHD pump. Overall, the results demonstrate that in a micro-gravity environment, liquid film flow boiling will be a severely limited heat transport process without facilitation by the EHD conduction pump.

4.3 Terrestrial EHD-driven liquid film flow boiling study on nano-fiber enhanced heater surface

Considering the heat transfer limits described above, liquid film flow boiling on a bare surface driven by hydrostatic pressure alone cannot supply a high enough heat transfer coefficient for many applications such as cooling of high-powered microelectronics (some of which require high heat flux removal rates while maintaining low surface temperature). With this in mind, there are several methods of increasing the heat transfer coefficient and heat flux during liquid film flow boiling. We have already considered one method which is increasing the flow rate of the incoming liquid via EHD conduction pumping, which improves convective heat transfer and re-wets the heater surface. In this section we also consider an additional method whereby we modify the surface characteristics of the heater in order to increase the wetted area

or increase bubble nucleation site density, for example, since it has been shown that doing so substantially affects performance enhancement of nucleate pool boiling heat transfer. In order to create appropriate surface structures, various techniques have been proposed such as surface machining, chemical deposition etc. In [84-87], for example, it was demonstrated that irrespective of the boiling regime and gravity magnitude, copper-plated nanofiber-coated surfaces result in an almost order of magnitude higher heat removal rate. The improved heat removal capacity can be attributed to the increase of some important boiling parameters such as nucleation site density (resulting from very high surface area-to-volume ratio), higher superheat of the liquid in the boiling regime and bubble departure frequency. All these factors facilitate a significant increase of nucleate boiling over the nanofiber-coated surfaces in comparison with the corresponding bare surfaces. In collaboration with a group at the University of Illniois – Chicago, Multiscale Mechanics and Nanotechnology Laboratory, a copper surface was coated with a copper-plated nanofiber mat and experiments in liquid film flow boiling (similar to those in the previous section) were conducted using those samples.

The liquid film flow boiling process driven by EHD conduction pumping described above was also previously studied in [44]. The two major differences between the previous and present research setups are the following: (i.) EHD electrode design and spacing between electrode pairs that were studied in [44] were different as discussed above and (ii.) Liquid film flow boiling was only studied for a bare ceramic heater surface in [44], whereas the present work includes a comparison between bare and copper-plated nanofiber-enhanced heater surfaces.

The motivation of the research presented in this section is to use the unique combination of the two above-mentioned methods and study the entire liquid film flow boiling regime. in this experimental study, electrowetting of a copper-plated nanofiber-enhanced surface via EHD

conduction pumping mechanism is investigated for the full liquid film flow boiling regime up to the critical heat flux. The results of this study will allow development of an EHD conduction-driven two-phase heat transport system for thermal management in terrestrial and micro-gravity applications while the working dielectric fluid is allowed to be in direct contact with the heat source.

4.3.1 New heater design

In order to deposit the copper-plated nanofibers onto the heater surface, new copper heaters were designed (as opposed to the ceramic heater used in the previous section). Liquid film flow boiling on two heater surfaces was studied: a bare surface and nanofiber-enhanced surface. The heaters were fabricated using 32-gage Nichrome resistance wire (with a resistance of 34 Ω/m at 25°C) wrapped around machined copper pieces which had a thermal conductivity of 390 W/m·K. The resistance wire had a thin layer of Polyimide electrical insulation and the outer diameter of the wire (including the insulation layer) was 0.241 mm. The cylindrical copper pieces were machined with a metal lathe and the top surfaces were faced to make them smooth. The bare heater surface was polished successively with 240-grit and 600-grit sandpaper for a smooth finish. The diameter of the top surface (where boiling occurred) was 18.0 mm, which gave a surface area of 254 mm^2 or 2.54 cm^2. Applied voltage and resistance were used to calculate heater power and this was divided by the heater surface area to give heat flux. A 36-gage T-Type wire thermocouple was soldered to the copper piece which gave the measurement for $T_{surface}$ as shown in the results section. A hole with a depth of 3.0 mm was drilled into the side of the copper piece and the tip of the thermocouple (where the temperature was measured) was inserted in the hole and soldered. The tip was 1.5 mm below the top surface where the working fluid was boiled. A 2D axisymmetric numerical simulation (shown in Appendix B.3) of steady-

state heat conduction within the copper piece at all expected heat loads was performed. The results of the simulation confirmed a uniform heat flux on the top surface of the copper piece. They also showed that the maximum difference in temperature at the location of the thermocouple (as illustrated in Figure 63) and corresponding temperature on the top surface of the heater was 0.9°C. It is important to note that this only occurred for heat flux greater than 20.0 W/cm^2. Therefore, for the majority of heat loads the top surface temperature measurement via embedded thermocouple was justified. The resistance wire was wrapped around the copper piece and the assembly was inserted into a cylindrical thermal Delrin insulator as shown in Figure 63. The thermal conductivity of Delrin is 0.33 W/m·K and at the maximum heat load, the heat loss to the sides and bottom was estimated to be less than 3%. Epoxy was applied around the edge of the heater to ensure that working fluid did not infiltrate into the Delrin insulator. The heater assembly was installed into the experiment housing at the center of the electrode disc (described in the previous section) as shown in Figure 64.

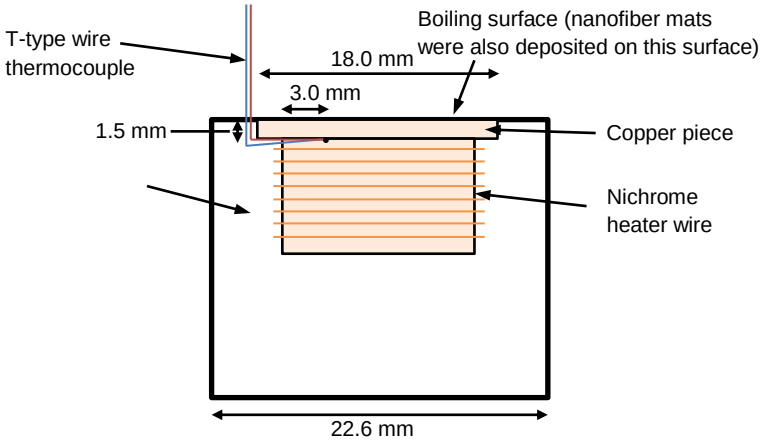

Figure 63: Heater assembly showing copper heater piece installed in Delrin insulator

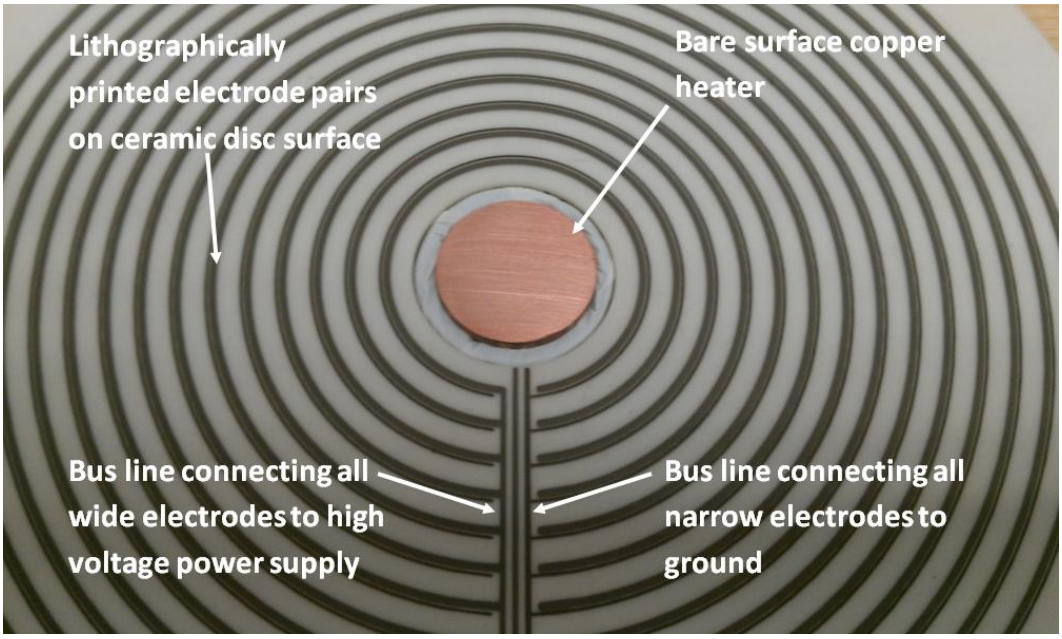

Figure 64: Electrode disc with bare surface copper heater

The same experiment housing as the previous section was used. However, some instrumentation was different. In place of the RTD probe for vapor temperature measurement (for T_{sat}), a T-type thermocouple probe was used. Absolute pressure of the fluid was measured using a Validyne AP10-42 pressure transducer. The heater power supply was a Lambda LMS 9000 and EHD power supply was a Glassman Series EH HV. Data were acquired using the National Instruments USB 6211 and NI 9213 with the NI-USB 9162 High Speed Carrier. For these reasons, the systematic errors and overall uncertainty were different than those in the previous section. The systematic errors in all measurements and maximum uncertainty of derived quantities are given in Table X.

Table X: Maximum systematic error of various measurement devices and experimental uncertainty for chapter 4, section 4.3

Measurement	Maximum systematic error
Temperature	±0.5°C
Applied voltage to EHD electrodes	±30 VDC
Current measured through EHD electrodes	±20 μA
Applied voltage to heater	±0.06 V
Resistance of heater	±0.05 Ω
Absolute pressure	±350 Pa
Derived quantity	**Maximum uncertainty**
Superheat, ΔT	±0.71°C
Heat flux, q”	±3.9%
Heat transfer coefficient, h	At ΔT = 1.8°C: ±40.0%*
	At ΔT = 15.3°C: ±5.8%
	At ΔT = 16.8°C: ±5.5%

*This large error only occurred at very low heat flux levels during the liquid phase convection regime.

4.3.2 Nano-fiber mat deposition process

For preparation of the copper-plated nanofiber-coated surface, the following steps were taken. Initially the bare surface was sputter-coated by Pt/Pd to a thickness of 7.5 nm. Then the sputter-coated surface was coated with electrospun Polyacrylonitrile (PAN) nanofibers from a 12 wt% PAN solution in N,N-dimethylformamide. Details of electrospinning are available in [88]. The electrospun nanofibers were used as a template for preparing the copper-plated nanofibers as described in [84, 85]. In brief, the electrospun nanofiber mat was then sputter coated to a

thickness of 7.5 nm. This sensitized the polymer nanofiber mat to facilitate the subsequent electroplating by copper using the methods described in [84, 85]. The sputter coating on the bare surface allowed better nanofiber adhesion to the heater surface. This made the nanofiber mat robust under vigorous boiling. A scanning electron microscope (SEM) image is shown in Figure 65. The SEM image reveals that in addition to a dramatically increased surface area of the nanofiber mat, the nano-scope features on the individual fibers also increases the overall surface area.

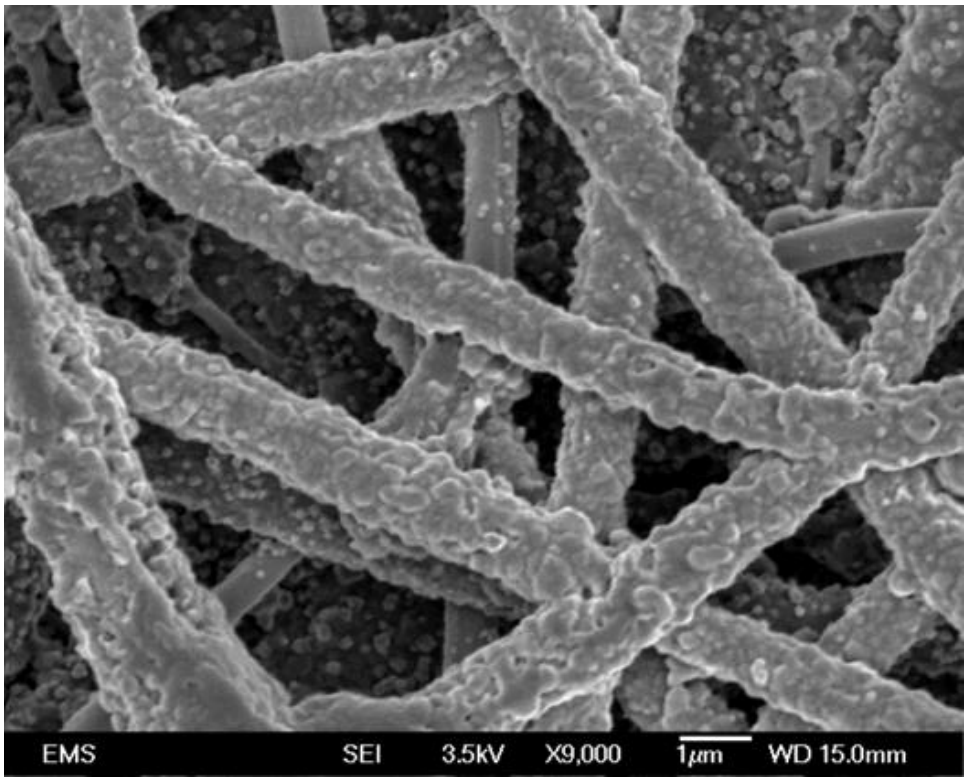

Figure 65: SEM image of copper-plated nanofiber mat

4.3.3 Results and discussion

The following four sets of experiments were performed to determine the combined effects of EHD conduction pumping of liquid film and the copper-plated nanofiber-enhanced surface:

Case 1: Bare surface, 0 kV applied EHD potential

Case 2: Bare surface, 0.75 kV applied EHD potential

Case 3: Nano-fiber enhanced surface, 0 kV applied EHD potential

Case 4: Nano-fiber enhanced surface, 0.75 kV applied EHD potential

The experimental chamber was first evacuated to remove air from the system. For the copper-plated nanofiber enhanced surface, a low heat flux was applied to the heater (<1.0 W/cm^2) during the evacuation process in order to facilitate the release of any trapped vapor or gases within the small micro-cavities in the nano-fiber mesh. Once the vacuum level was sufficient (~500 mTorr), the experimental chamber was charged with a fixed amount of refrigerant HCFC-123 which resulted in a liquid film 2.0 ± 0.3 mm thick above the electrode disc and heater surface. The recirculating chiller was set to a fixed temperature and the system was allowed to reach steady state (this was the point at which the saturation temperature and heater surface temperature did not fluctuate by more than 0.1°C/min about the mean value). Once the saturation temperature and pressure matched values from thermodynamic tables for pure HCFC-123, a potential of 0.75 kV was applied to the high voltage EHD electrodes. This caused the liquid film to be pumped from the periphery of the disc toward the heater at the center (the pumping was visible in the form of small ripples on the liquid surface). Next, power was applied to the electric heater. Heat flux was incremented initially by 0.25 W/cm^2 until 2.0 W/cm^2 was reached. After this point, it was incremented by 0.5 W/cm^2 until the critical heat flux was reached. The time between heat flux increments was 300 seconds, which allowed the surface temperature to reach steady state (defined above).

The results of all four experiments are shown in Figure 66. Heat flux, or q”, is shown on the y-axis and heater superheat, or ΔT, is shown on the x-axis. The latter is the difference

between the heater surface temperature and the saturation temperature measured above the heater, i.e. $\Delta T = (T_{surface} - T_{sat})$. The error bars show the measurement uncertainty in ΔT. Since uncertainties in heat flux (which have a maximum of ±3.9%) are too low to be visible as vertical error bars, they are not included. The lower left portion of the graph in Figure 66 is expanded Figure 67 in to highlight the low heat flux results. Uncertainty bars have been removed in Figure 67 for the sake of clarity. In addition to the liquid film flow boiling curves, the boiling heat transfer coefficients, h, (found by $h = q''/\Delta T$) as a function of ΔT for all cases are shown in Figure 68.

Case 1 is considered first. The liquid film flow boiling curve for this case shows that up to a heat flux of 1.0 W/cm^2, the superheat increased steadily with increasing heat flux, which is consistent with the natural convection regime of boiling. When the heat flux was increased to 1.1 W/cm^2, there was a reduction in ΔT of 0.6°C as the onset of nucleate boiling (ONB) was reached and heat transfer improved due to the formation of isolated bubbles on the heater surface. As heat flux was increased beyond 5.0 W/cm^2, bubble nucleation occurred on the entire heater surface. The high rate of vaporization due to rapid bubble formation was accounted for by incoming liquid from the surroundings. Even though the liquid film thickness was only 2.0 mm (therefore, hydrostatic pressure in the liquid film was ~30 Pa), this was sufficient to maintain liquid flow to the heater until critical heat flux was reached. The critical heat flux for case 1 was 20.14 W/cm^2 and ΔT was 29.85°C. At this heat flux, bubble formation was rapid and bubble coalescence occurred extensively. Eventually, coalescence led to vapor blanket formation over the heater surface and caused it to dry out. At this point, the heater surface temperature increased dramatically at a rate >30°C/s and the heater was automatically shut off by the data acquisition system.

Case 2 departed from case 1 as has been shown before [44] due to the activation of the EHD conduction pump. As before, the ΔT increased steadily with increasing heat flux initially in the natural convection phase. However, in this case, the activation of the EHD conduction pump increased the convection since there was now a flow of incoming fluid from the heater surroundings. Compared to the hydrostatic pressure (~30 Pa), the pressure generated by the EHD electrodes at applied potential of 0.75 kV was ~265 Pa (approximated from experimental measurements). This produced significant fluid circulation as fluid velocity was on the order of several cm/s. As a result, the onset of nucleate boiling was actually delayed from 1.0 W/cm^2 to 1.25 W/cm^2. As the heat flux was increased further beyond ONB, the values of ΔT began to match those in case 1, but eventually at a heat flux of 2.2 W/cm^2, the two curves crossed. From this point on, the ΔT for a given heat flux was lower for case 2 than case 1 (or from the other perspective, for a given ΔT, the corresponding heat flux was higher for case 2 than case 1). For example, at ΔT =25.0°C the corresponding heat flux (and boiling heat transfer coefficient as well) for case 2 was 30% higher than case 1. This notable enhancement was due to the increased flow rate of the EHD conduction driven liquid film, which was able to re-wet the heater surface with fresh cool liquid from the heater surroundings. These enhancements in heat flux and ΔT could be further improved by optimizing the design of the EHD electrodes and applying a higher potential, resulting in higher pressure generation (and therefore, higher flow rate) and improved heat transfer. In addition to terrestrial heat transfer enhancement, EHD conduction-driven liquid film boiling has also shown great promise for micro-gravity applications. When no hydrostatic pressure is present, this unique technique can be used to maintain liquid flow to the heater surface during liquid film flow boiling and lower surface temperature in the absence of gravity (as demonstrated successfully in the previous section).

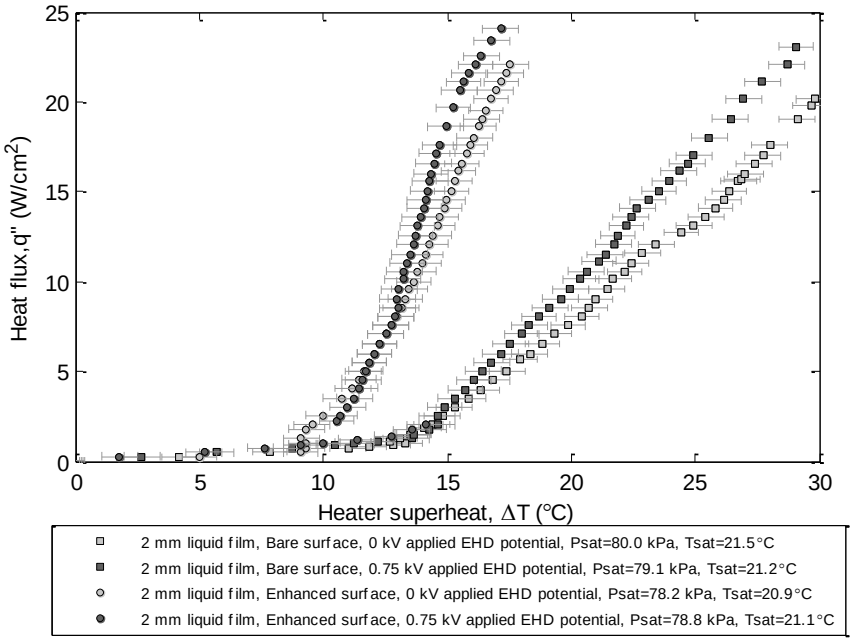

Figure 66: Liquid film flow boiling for bare and nano-fiber enhanced surfaces with and without EHD conduction pumping

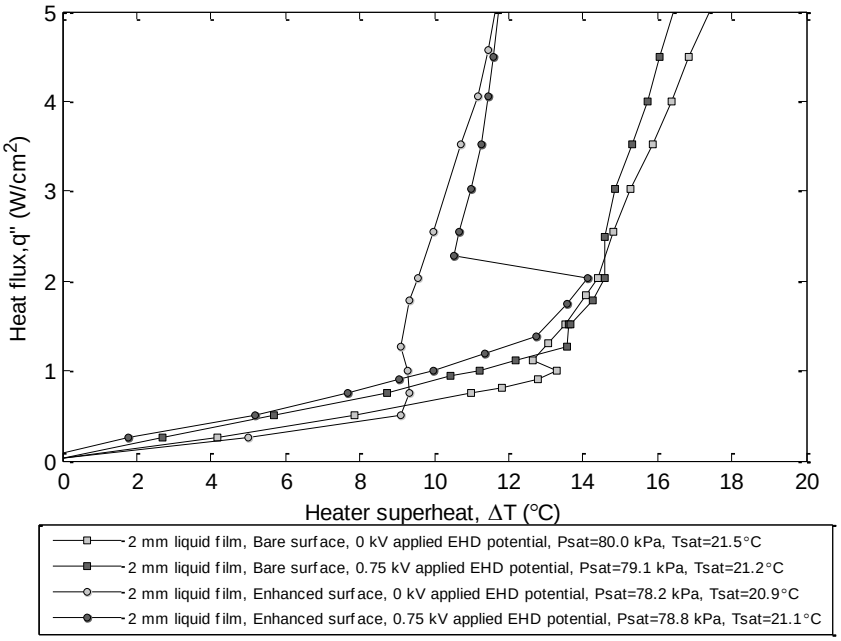

Figure 67: Low heat flux portion of Figure 66

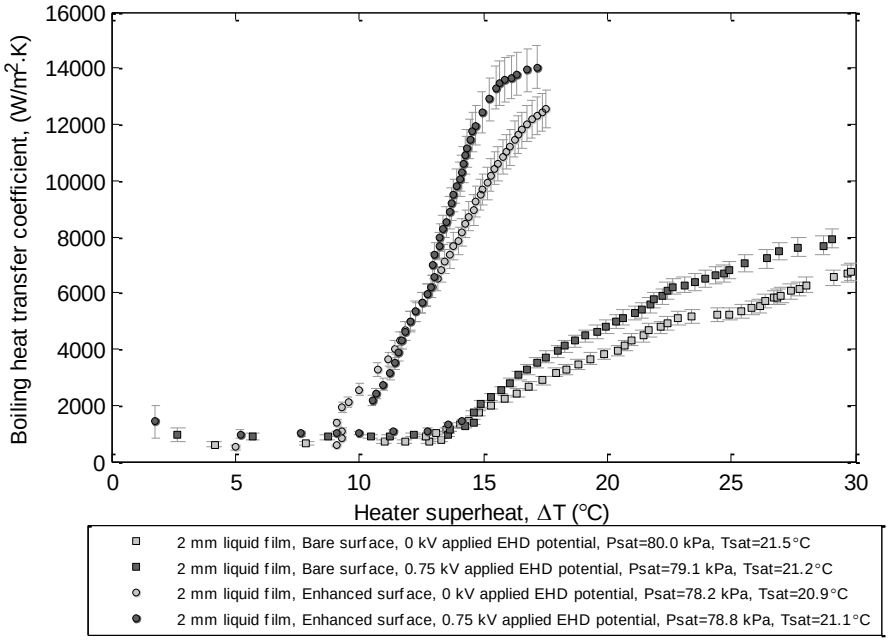

Figure 68: Boiling heat transfer coefficient for bare and enhanced surfaces with and without EHD conduction pumping

In case 3, there was a much more drastic shift in the liquid film flow boiling curve. The onset of nucleate boiling began earlier than any other case at a heat flux of 0.5 W/cm^2. This was characterized by localized bubble formation on the nano-fiber surface [85]. Bubbles appeared to be smaller than those during ONB for the bare surface. The results suggest that the presence of increased active nucleation sites and increased exposed surface area on the nano-fiber enhanced surface led to the lowering of ONB. They revealed improved the heat transfer as there were greater numbers of smaller bubbles for a given heat flux compared to the bare surface and this helped lower the heater surface temperature. Beyond ONB, the slope of the liquid film flow boiling curve in the case of the nanofiber-enhanced surface was much steeper than the one for the bare surface cases and this resulted in large heat transfer enhancement. Select values of ΔT are shown in Table XI with corresponding heat fluxes and enhancement in boiling heat transfer

coefficients. For example, at $\Delta T = 15.3°C$, the heat flux in case 3 was 418% higher than in case 1. At $\Delta T=16.8°C$, the enhancement was slightly reduced to 350% which was still well above the bare surface cases (cases 1 and 2) as shown in Table XI.

For the results of case 4, the low heat flux data showed interesting features. As the heat flux was increased during the natural convection regime, the ONB was delayed to 2.0 W/cm^2, which was the highest value among the four cases. At this point, bubble nucleation began suddenly and there was a 3.6 °C drop in ΔT. As heat flux was increased further, the curves of cases 3 and 4 crossed in a similar manner to cases 1 and 2. However, this happened over a larger range of heat flux (5.5-8.0 W/cm^2). For this heat flux range, the curves of cases 3 and 4 were identical. Beyond 8.0 W/cm^2, the liquid film flow boiling curve for case 4 showed lower ΔT for a given heat flux compared to the curve for case 3. The results indicate that the combined effects of the copper-plated nanofiber-enhanced surface and EHD conduction pumping of liquid film were actually adverse at low heat flux, since the EHD conduction effectively delayed ONB. However, both techniques complemented each other as the heat flux was increased beyond 8.0 W/cm^2. Therefore, despite the already significant enhancement in heat transfer present due to the copper-plated nanofiber-enhanced surface in case 3, activation of the EHD conduction pump in case 4 was able to enhance it even further. At $\Delta T = 15.3°C$, the heat flux for case 4 was 4.1 W/cm^2 higher than case 3, which corresponded to a heat removal rate of 10.4 W. The electric power input to the EHD pump (the product of average applied potential, 750V, and average current, 0.25 mA) was 0.19 W. This resulted in a power input-to-heat removal ratio of 1 to 55, which was an inconsequential power requirement considering the enhancement possible. The comparison between case 4 and case 1 at $\Delta T = 15.3°C$ also showed considerable enhancement of 555% in heat flux and heat transfer coefficient. This reduced to 422% for $\Delta T = 16.8°C$ but was

still a striking improvement. It is important to note that the magnitudes of boiling heat transfer coefficients achieved with the combined techniques in this work are relatively larger than typical values for dielectric refrigerants. As mentioned above, the performance of this system could be further improved by optimizing the EHD electrode design and increasing applied potential. Further optimization of the nanofiber coating process would also be necessary before proceeding towards commercialization for applications in thermal management. In addition to the terrestrial results presented here, EHD conduction pumping of liquid film is even more important in micro-gravity, since the liquid film flow boiling process cannot be sustained as a thermal management technique without it.

Table XI: Select ΔT values and corresponding enhancements for all cases

Case	ΔT (°C)	Corresponding heat flux (W/cm^2)	Heat transfer coefficient, h ($W/m^2 \cdot K$)	Comparison of h to case 1
1	15.3	3.0	1970	--
2		3.5	2300	17%
3		15.6	10190	418%
4		19.7	12900	**555%**
1	16.8	4.5	2670	--
2		5.5	3280	23%
3		20.1	12020	350%
4		23.4	13930	**422%**

4.4. Conclusions

EHD conduction pumping was successfully used for electro-wetting of a heater during liquid film flow boiling in terrestrial and micro-gravity conditions. The terrestrial tests showed that a 62% increase in the critical heat flux was possible for given operating conditions when

EHD conduction was used to pump fresh cool liquid toward the heater surface during liquid film flow boiling. The micro-gravity tests were conducted on board a variable gravity parabolic flight for the first time. The liquid film flow boiling process was facilitated by using EHD conduction to pump liquid film toward the heater surface, re-wetting it. The results indicate that at heat flux below 5.0 W/cm^2, activation of the EHD pump delayed the onset of nucleate boiling for both cases of 0-g and 1.8-g. Thus, there was an adverse effect of EHD on heater surface temperature. Above this heat flux however, at 7.0 W/cm^2 and 9.0 W/cm^2, the activation of EHD conduction pump did lower heater surface temperature. The observed differences were due to the EHD effect on reduction of the superheat under transient conditions. The results were valuable as they provided new insights into EHD-driven liquid film flow and liquid-vapor phase change process in the presence and absence of gravity. They demonstrated the capability of EHD conduction pumping of liquid film in the absence of gravity even under the harsh environment of the parabolic flight experiments. They also support the need for further experiments in electrically driven liquid film flow boiling in a continuous micro-gravity environment where steady-state conditions can be reached and concrete conclusions can be drawn.

In addition to the above, experiments in liquid film flow boiling driven by EHD conduction pumping were also successfully completed for bare- and copper-plated nanofiber-enhanced surfaces. The effect of the copper-plated nanofiber-enhanced surface was to primarily increase the effective surface area and nucleation site density which facilitated bubble formation and lowered the heater surface temperature. The results indicate that at low heat flux, activation of the EHD pump delayed the onset of nucleate boiling. Thus, there was an initial adverse effect of EHD on heater surface temperature in the combined EHD/enhanced surface experiment. However, beyond the isolated bubble regime, the two techniques worked exceedingly well

together and resulted a maximum of 555% enhancement in boiling heat transfer coefficient compared to the bare surface experiment without EHD conduction pumping. Furthermore, the results show that despite significant enhancements possible with the copper-plated nanofiber-enhanced surface (418%), activation of the EHD conduction pump at moderate applied potential was able to increase it even further (to 555%) with a ratio of electric power consumption to heat removal rate of 1:55. The results show great promise for development of EHD conduction-driven heat transport systems for both terrestrial and micro-gravity thermal management applications.

CHAPTER 5 – COMBINED DIELECTROPHORETIC AND EHD CONDUCTION PUMPING FOR ENHANCEMENT OF LIQUID FILM FLOW BOILING[4]

5.1 Introduction

Liquid film flow boiling driven by EHD conduction pumping has been described in detail in chapter 4. In this chapter, EHD conduction is combined with an additional technique known as dielectrophoresis and further experiments in liquid film flow boiling and pool boiling are conducted. The dielectrophoretic (DEP) force has already been introduced in chapter 1, section 1.3. It is one of the terms in the electric body force equation, in addition to the Coulomb force (which is responsible for conduction pumping). Unlike the Coulomb force, it acts on polarized charges and can be used to influence vapor bubble motion during nucleate boiling. The DEP force acting on a vapor bubble of diameter a is given by [45]

$$\boldsymbol{F_{DEP}} = 2\pi a^3 \varepsilon_1 \left(\frac{\varepsilon_2 - \varepsilon_1}{\varepsilon_2 + 2\varepsilon_1}\right) \boldsymbol{\nabla} |\boldsymbol{E}_e|^2 \tag{34}$$

In Eq. (34), particles are repelled from regions of stronger electric fields if their permittivity is less than that of suspension medium, $\varepsilon_2 < \varepsilon_1$. For the experiments in this work, the liquid medium is the working fluid HCFC-123 and its permittivity is found in Table VI, i.e. $\varepsilon_1 = 42.43 \times 10^{-12}$ F/m. For the vapor bubble, the permittivity of a vacuum is used, i.e. $\varepsilon_2 \approx \varepsilon_0 = 8.854 \times 10^{-12}$ F/m. The dielectrophoretic force is proportional to the gradient of the electric field squared. A strong non-uniform electric field results in a DEP force acting on individual vapor bubbles. Therefore, by designing the appropriate electrode geometry and applying a high enough potential, the DEP force magnitude can be made equal to or greater than the buoyancy force acting on a given vapor bubble (up to two orders of magnitude greater, as will be shown below). Vapor bubbles which

[4] The work in this chapter is currently under preparation for journal publication.

are departing from the heater surface during nucleate boiling can be removed at a much higher rate than that possible via buoyancy forces alone.

The research presented in this chapter is a combination of the above two methods. Experiments in liquid film flow boiling are conducted in the radial heat transport system configuration as done previously in chapter 4. EHD conduction pumping is used to generate liquid film flow from the surroundings for electro-wetting of the heater surface. Simultaneously, a strong non-uniform local electric field above the heater surface is also used to generate the dielectrophoretic force for increased vapor bubble extraction during the nucleate boiling regime. The height of the liquid film and applied potentials for the EHD and DEP electrodes are varied to determine their effect on the entire liquid film flow boiling regime up to critical heat flux.

5.2 Experimental setup

5.2.1 EHD pump substrate disc and heater design

The same liquid film flow boiling experimental setup from chapter 4 was used, with the exception of the EHD pump electrode disc, which was changed. Design A (as shown in Figure 25 and Table IV) was used instead of design B. Design A had fewer electrode pairs (7 vs. 14) but larger electrode sizes and spacing compared to design B. This allowed for higher applied potential (up to 2.0 kV), greater pressure generation and flow rate in the liquid film during the experiments. The dimensions are shown below in Figure 69 for convenience.

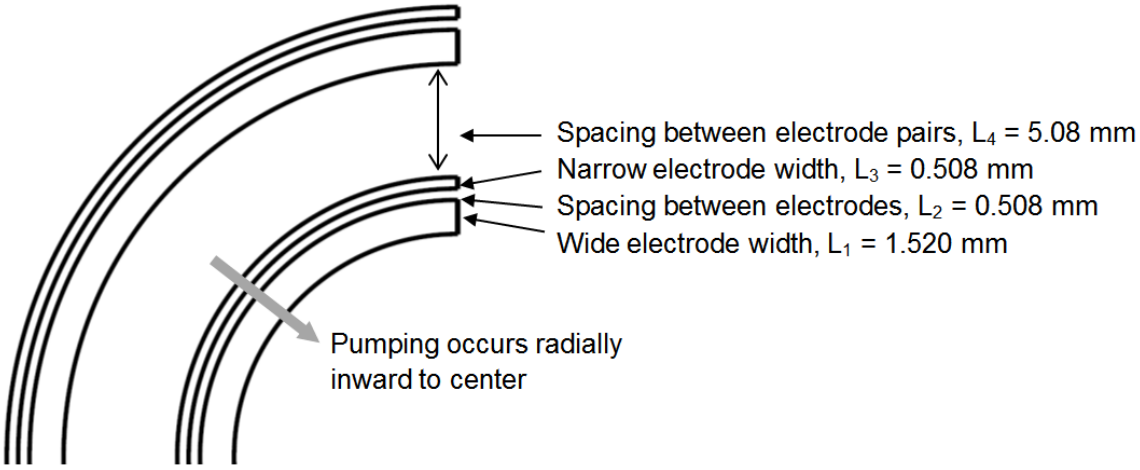

Figure 69: Schematic showing electrode dimensions and spacing between electrode pairs for EHD liquid film pump in chapter 5

The heater (which also functioned as the ground electrode) was the same circular copper surface used in previous liquid film flow boiling experiments in chapter 4, section 4.3. The details of the heater dimensions are shown in Figure 63.

5.2.2 DEP electrode design

The high voltage DEP electrode was a square stainless steel plate with sides of 22.6 mm and thickness of 0.381 mm, installed directly above the heater at a fixed height. It was designed such that it would be larger than the heater (which had a diameter of 18.0 mm) and could be installed in the existing experimental setup without having to make significant modifications. A total of 17 slots of 0.51 mm width were laser-cut into the electrode. This type of geometry was chosen for two reasons: (i) it allowed for a high degree of non-uniformity of the electric field, which caused the gradient of the electric field to be high and consequently increased the dielectrophoretic force generated (as shown in Eq. (34)) and (ii) since the electrode would be directly above the heater surface where bubbles nucleated and departed, slots were necessary to allow extracted bubbles to escape. The DEP electrode dimensions are shown in Figure 70.

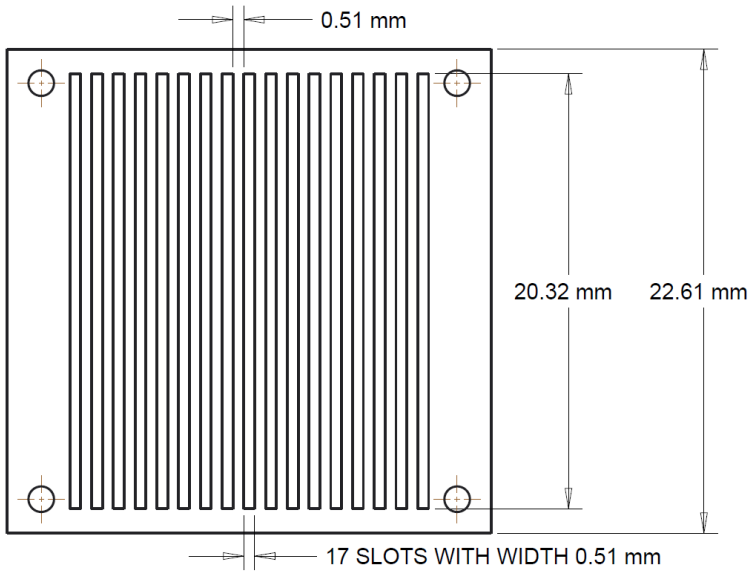

Figure 70: Stainless steel DEP electrode design

Four threaded holes were made at the corners for Nylon screws which would support the DEP electrode on the EHD electrode disc surface. Nylon was chosen because it was electrically insulating and compatible with the working fluid. The height of the DEP electrode could be easily adjusted by turning the screws with a screwdriver. A copper rod was soldered to the DEP electrode and this acted as an additional structural support but also served as the connection to the high voltage feedthrough installed in the wall of the experiment housing. In this way, potential could be applied to the DEP electrode separately from the EHD electrodes.

5.2.3 Combined EHD and DEP electrode installation

The heater assembly was installed into the experiment housing at the center of the electrode disc described above. The DEP electrode was installed directly above the heater at a height of 1.0 mm. An additional wire was also soldered to the side of the heater and connected to the common ground bus line of the EHD electrodes. The entire assembly is shown below in Figure 71. The experimental uncertainty in all measurements and propagation of error analysis are given in Table XII.

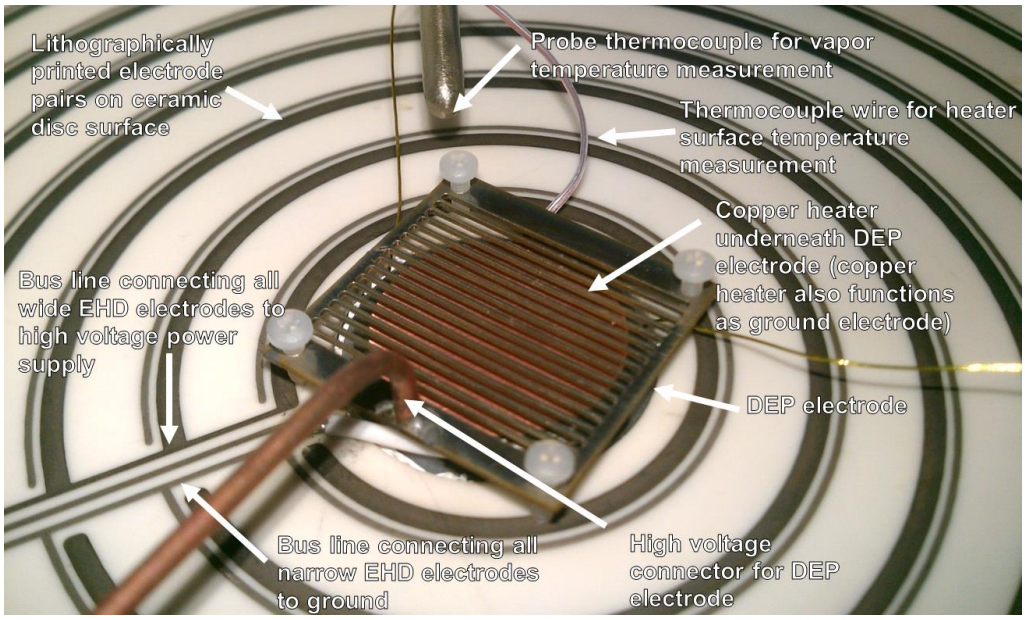

Figure 71: Combined EHD and DEP electrode installation in liquid film flow boiling experiment

Table XII: Maximum systematic error of various measurement devices and experimental uncertainty for chapter 5

Measurement	Maximum uncertainty
Temperature	±0.5°C
Applied voltage to EHD electrodes	±30 VDC
Applied voltage to DEP electrodes	±50 VDC
Current measured through EHD electrodes	±20 μA
Current measured through DEP electrode	±150 μA
Applied voltage to heater	±0.06V
Resistance of heater	±0.05 Ω
Absolute pressure	± 350 Pa
Derived quantity	**Maximum uncertainty**
Superheat, ΔT	±0.71°C
Heat flux, q”	±3.9%

5.3 Experimental results and discussion

The experiment procedure was identical to that in chapter 4. However, the applied potentials were different and there was an additional step to activate the DEP electrode. The experiment chamber was first evacuated and charged with a fixed amount of refrigerant HCFC-123. Depending on the experiment, it was either a liquid film 2.0 ± 0.3 mm thick or a liquid pool 10.0 ± 0.3 mm deep above the electrode disc and heater surface The recirculating chiller was set to a fixed temperature and the system was allowed to reach steady state (this was the point at which the saturation temperature and heater surface temperature did not fluctuate by more than 0.1°C/min about the mean value). Once the saturation temperature and pressure matched values from thermodynamic tables for pure HCFC-123, a potential of 1.5 kV was applied to the high voltage EHD electrodes. At the same time, a potential of 2.5 kV was applied to the high voltage DEP electrode. Next, power was applied to the electric heater. Applied voltage and resistance were measured to calculate heater power which was divided by the heater surface area to give heat flux. The following liquid film flow boiling and pool boiling experiments were performed using the combination of EHD conduction pumping and DEP force:

Table XIII: Experimental matrix for chapter 5

Case	Liquid film thickness or pool depth (mm)	Applied EHD potential (kV)	Applied DEP potential (kV)
1	2.0	0	0
2	2.0	0	2.5
3	2.0	1.5	2.5
4	2.0	2.0	2.5
5	10.0	0	2.5

Heat flux was incremented initially by 0.25 W/cm^2 until 2.50 W/cm^2 was reached. After this point, it was incremented by 0.50 W/cm^2 until the critical heat flux was reached. The time between heat flux increments was 300 seconds, which allowed the surface temperature to reach steady state (defined above). The results of all experiments are shown in Figure 72. Heat flux, *q",* was plotted against the superheat, $\Delta T = (T_{surface} - T_{sat})$. The low heat flux data for all cases from Figure 72 are shown in Figure 73. The error bars show the measurement uncertainty in ΔT. Since uncertainties in heat flux (which have a maximum of ±3.9%) are too low to be visible as vertical error bars, they are not included. For clarity, uncertainty bars in Figure 73 have been removed.

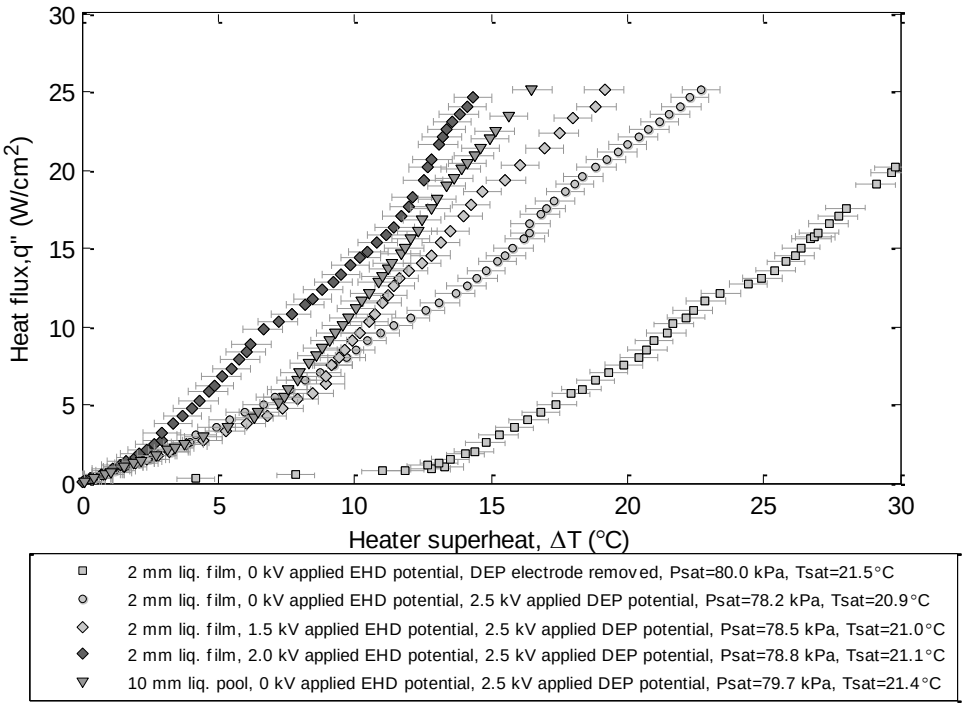

Figure 72: Experimental data for combined EHD- and DEP-enhanced liquid film flow boiling and pool boiling

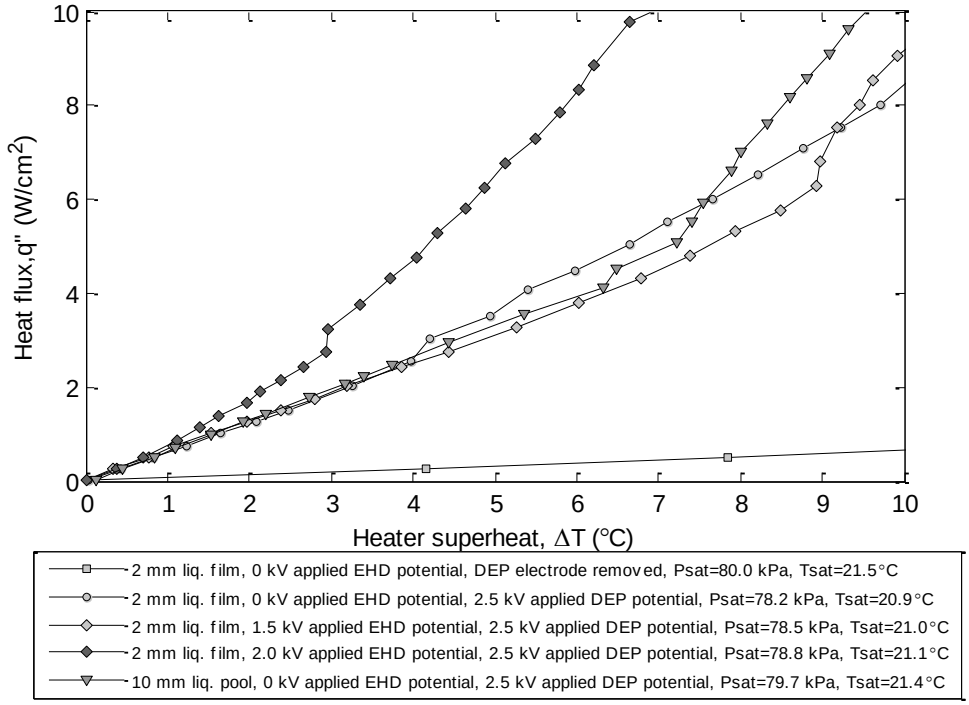

Figure 73: Low heat flux data for all cases from Figure 72

Case 1 represents the experimental data for liquid film flow boiling in the absence of any applied electric field (with the DEP electrode removed). The data were the same as chapter 4; section 4.3 and were simply repeated here. They show that the superheat increased steadily with increasing heat flux. The onset of nucleate boiling (ONB) occurred at 1.10 W/cm^2. As heat flux was increased beyond 5.00 W/cm^2, bubble nucleation occurred on the entire heater surface. The high rate of vaporization due to rapid bubble formation was accounted for by incoming liquid from the surroundings and liquid flow was driven exclusively by hydrostatic pressure. The critical heat flux for case 1 was 20.14 W/cm^2 at ΔT of 29.9°C.

In case 2, the applied potential to the DEP electrode was set to 2.5 kV (potential was not applied to the EHD electrodes for this case). When this was done, liquid circulation was observed above the DEP electrode in the vicinity of the heater/ground electrode. Therefore,

although the purpose of the DEP electrode was to increase the rate of vapor bubble extraction via the dielectrophoretic force acting on the bubbles during nucleate boiling, at low heat flux in the presence of liquid, EHD conduction pumping occurred. This strong local liquid circulation caused the heater superheat to be significantly lower in case 2 than case 1 for a given heat flux. For example, at a heat flux of 2.00 W/cm^2, the heater superheat in case 2 was 3.25°C, vs. 14.4°C in case 1. The onset of nucleate boiling was signified by an increase in the slope of the boiling curve as shown in Figure 73. For case 2, this occurred at a heat flux of 2.25 W/cm^2 and bubble nucleation was observed on the heater surface as well. As the heat flux was increased further to 10.0 W/cm^2, superheat remained low in case 2 (11.4°C) compared to case 1 (21.7°C). Bubble nucleation occurred on the whole heater and the fraction of vapor covering the heater surface compared to liquid was increased. The continued enhancement suggests that the mechanism of EHD conduction that initially caused liquid circulation at low heat fluxes gave way to the dielectrophoretic force which dominated at higher heat fluxes by acting directly on polarized bubbles (since EHD conduction cannot function in vapor phase due to low conductivity). The higher rate of vapor bubble extraction allowed for increased inflow of liquid from the surroundings, maintaining a low superheat in case 2 compared to case 1 for a given heat flux. Although there was no discrete cross-over point at which one mechanism dominated over the other (i.e. EHD conduction vs. DEP), the onset of nucleate boiling was a useful indicator of when the DEP force began to influence vapor bubble motion.

In case 3, 1.5 kV was applied to the EHD electrodes and 2.5 kV was applied to the DEP electrode. The flow rate of liquid from the heater surroundings was increased as a result, since in addition to the hydrostatic pressure (~30 Pa) in the liquid film, the pressure generated by the EHD electrodes at applied potential of 1.5 kV resulted in flow velocities of 2-5 cm/s

(approximated from experimental measurements [30]). The increased incoming flow, as well as local liquid circulation directly above the heater surface due to the DEP electrode, caused the onset of nucleate boiling to be increased from 1.10 W/cm^2 in case 1 to 6.25 W/cm^2 in case 3. Despite the reduction in superheat already present in case 2 compared to case 1, the activation of the EHD conduction pump in case 3 reduced it even further for heat fluxes greater than 10.0 W/cm^2. For example, at 14.5 W/cm^2, superheat in case 3 was 12.8°C vs. 15.5°C in case 2 and 26.1°C in case 1. Alternatively, the enhancements in heat flux for a given superheat were quite remarkable. The enhancements in heat flux for ΔT = 14.1°C for all cases are given in Table XIV. Up to 834% enhancement in heat flux (and boiling heat transfer coefficient) was possible for case 3 compared to case 1.

Table XIV: Enhancements in heat flux for ΔT = 14.1°C for all cases

Case	ΔT (°C)	Corresponding heat flux (W/cm^2)	Comparison of h to case 1
1		1.83	--
2		12.6	589%
3	14.1	17.1	834%
4		24.1	**1217%**
5		20.4	1015%

In case 4, the applied EHD potential was increased to 2.0 kV and applied DEP potential was kept at 2.5 kV. Case 4 saw the highest enhancement of all results in heat flux. As shown in Table XIV, up to 1217% enhancement was made possible by application of both EHD (at higher potential) and DEP techniques. The combined power input for both EHD and DEP electrodes was 0.39W (based on applied potential and current measurements). Based on the above heat

fluxes at ΔT = 14.1°C (and heater surface area of 2.54cm^2), heater power for case 4 was 61.2W vs. 4.65W for case 1. This meant that the power input for the combined EHD and DEP mechanisms was only 0.7% compared to the increase in heater power that was achieved, which was an inconsequential power requirement.

In Case 5 the applied EHD potential was set to 0 kV, but applied DEP potential was 2.5 kV and the height of the liquid-vapor interface above the heater surface was also changed from 2.0 mm to 10.0 mm. This increased the hydrostatic pressure in the liquid from ~30 Pa to ~150 Pa. The results show that the pool boiling curve of case 5 initially had similar values of ΔT to that of case 2 up to a heat flux of 6.00 W/cm^2. However, beyond this heat flux, the two curves crossed and the pool boiling (with DEP) results of case 5 showed lower ΔT values for all heat fluxes compared to liquid film flow boiling (with DEP) of case 2. They also fell in between the curves for cases 3 and 4. For a given heat flux (above 10.0 W/cm^2), the ΔT values followed the following trend: case 4 < case 5 < case 3. This suggests that the increase in hydrostatic pressure in pool boiling was equivalent to increasing the applied EHD potential in liquid film flow boiling to a value between 1.5 – 2.0 kV. However, other effects were also observed. During liquid film flow boiling, when vapor bubbles reached the liquid-vapor interface (which was only 2.0 mm above the heater surface), they were free to move radially outward. During pool boiling, vapor bubbles moved vertically upward from the heater surface to the liquid-vapor interface (which was 10.0 mm above the heater surface) before moving in the radial direction. This meant that the amount of time vapor bubbles spent in the vicinity of the heater was different for liquid film flow boiling vs. pool boiling and which affected the heat transfer results as well.

The observations during liquid film flow boiling and pool boiling in the presence and absence of an electric field were recorded as videos and images. Figure 74 shows liquid film

flow boiling with the listed operating conditions. For this particular experiment, potential was applied to both EHD and DEP electrodes. The liquid film thickness was 2.0 mm, ensuring that the DEP electrode was submerged in liquid when the experiment was started. As the heat flux was increased and nucleate boiling regime was reached (and vapor bubbles covered the whole surface), the strong electric field created a large vapor bubble dome above the DEP electrode. The height of the dome was on the order of ~4 mm above the liquid-vapor interface. The rate of bubble nucleation and departure was rapid and the applied electric field appeared to facilitate bubble removal at a much higher rate than that possible with only buoyancy forces present. The EHD conduction pump also maintained a high liquid inflow from the heater surroundings through the gap in between the heater and DEP electrode. The simultaneous operation of the two mechanisms resulted in the highest enhancement in heat transfer achieved, as discussed above.

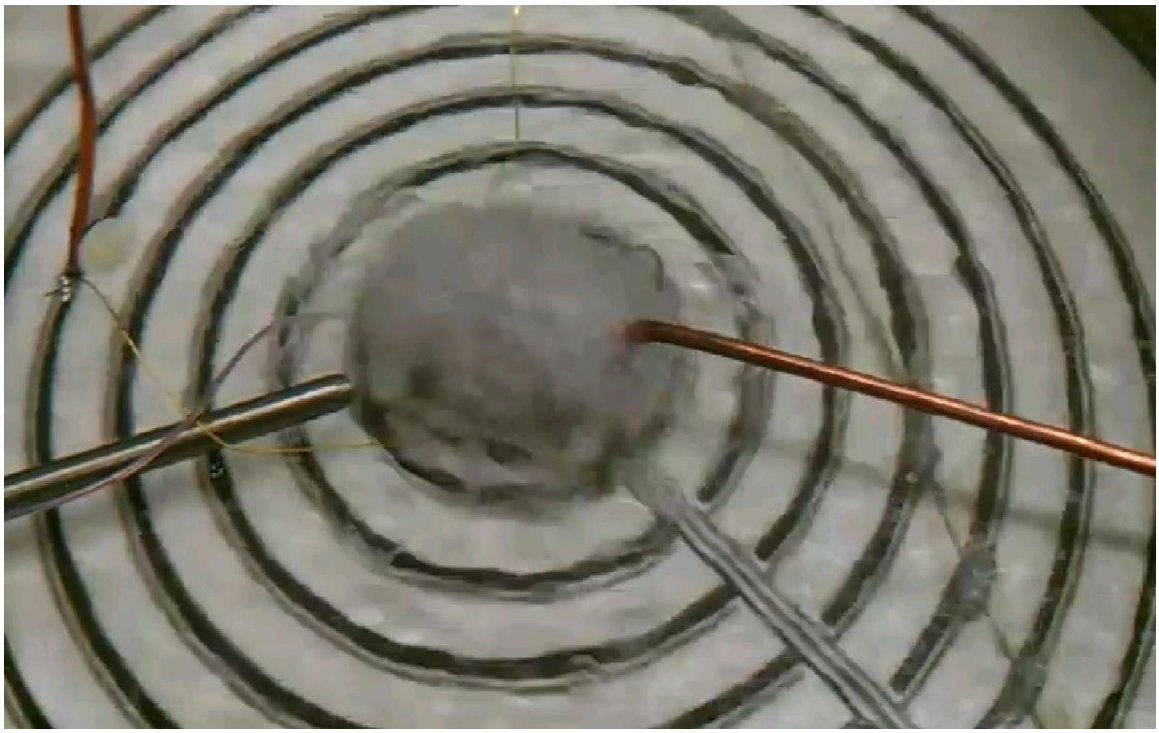

Figure 74: Image of liquid film flow boiling with film thickness: 2.0 mm, Heat flux: 15.0 W/cm^2, Applied EHD potential: 2.0 kV, Applied DEP potential: 2.5 kV

Interesting effects were observed for the experiments in pool boiling with applied potential to the DEP electrode, shown in Figure 75 with the listed operating conditions. For this heat flux and greater, when the vapor bubble columns reached the liquid-vapor interface they collectively created a wave which moved radially outward to the experiment chamber wall. There the wave reflected and moved back radially inward to the center. This caused a cyclic oscillation of the liquid-vapor interface during pool boiling. This effect was not observed for liquid film flow boiling or for pool boiling at heat fluxes less than 7.0 W/cm^2.

Figure 75: Image of pool boiling with pool depth: 10.0 mm, Heat flux: 12.0 W/cm^2, Applied EHD potential: 0 kV, Applied DEP potential: 2.5 kV

5.4 Numerical simulation of non-uniform electric field in dielectric liquid

In order to determine the order of magnitude of the dielectrophoretic force acting on the vapor bubbles during the boiling process, Eq. (34) was used and compared to the buoyancy force on a bubble in Eq. (38) (also given in chapter 1, section 1.3) [46].

$$\boldsymbol{F_{buoyancy}} = \frac{4}{3}\pi a^3(\rho_l - \rho_v)\boldsymbol{g} \tag{38}$$

Other forces acting on a bubble as it moves through a liquid medium include viscous drag and distortional effects due to the electric field. However, this analysis was simply a direct comparison between the DEP and buoyancy forces and others were not considered. To determine the dielectrophoretic force on a bubble of radius *a*, the electric field intensity was first found as a function of the spatial variables for the geometry considered, since the force was directed along its gradient. For the heater/DEP electrode geometry, shown below in Figure 76, a numerical simulation was necessary to determine the electric field distribution.

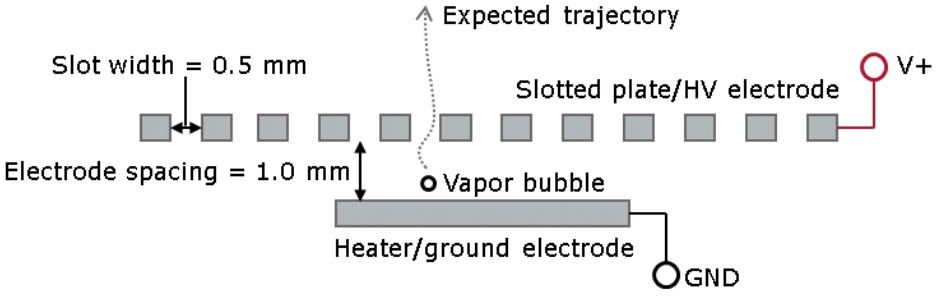

Figure 76: Heater/DEP electrode geometry

To determine the electric field distribution, the Laplace equation was first solved for the potential, ϕ, with zero space charge in the dielectric medium in a 2D numerical domain. Only the dielectric liquid medium was considered (with permittivity of ε_1 as specified above), and it was assumed that no bubbles were present for the calculation of potential. Voltage was specified at the electrodes. The Laplace equation for potential was

$$\nabla^2\phi = 0 \tag{43}$$

The electric field was then found by the relation

$$\boldsymbol{E_e} = -\nabla\phi \tag{44}$$

The boundary conditions for the high voltage and ground electrodes were

$$\begin{aligned} \phi_{HV} &= 2500V \\ \phi_{GND} &= 0V \end{aligned} \tag{45}$$

The charge at each boundary in the overall domain was also set to zero. The numerical simulation was performed in COMSOL Multiphysics and the solution of the electric potential and electric field norm, given by $E_{norm} = \sqrt{E_x^2 + E_y^2}$, are shown in Figure 77.

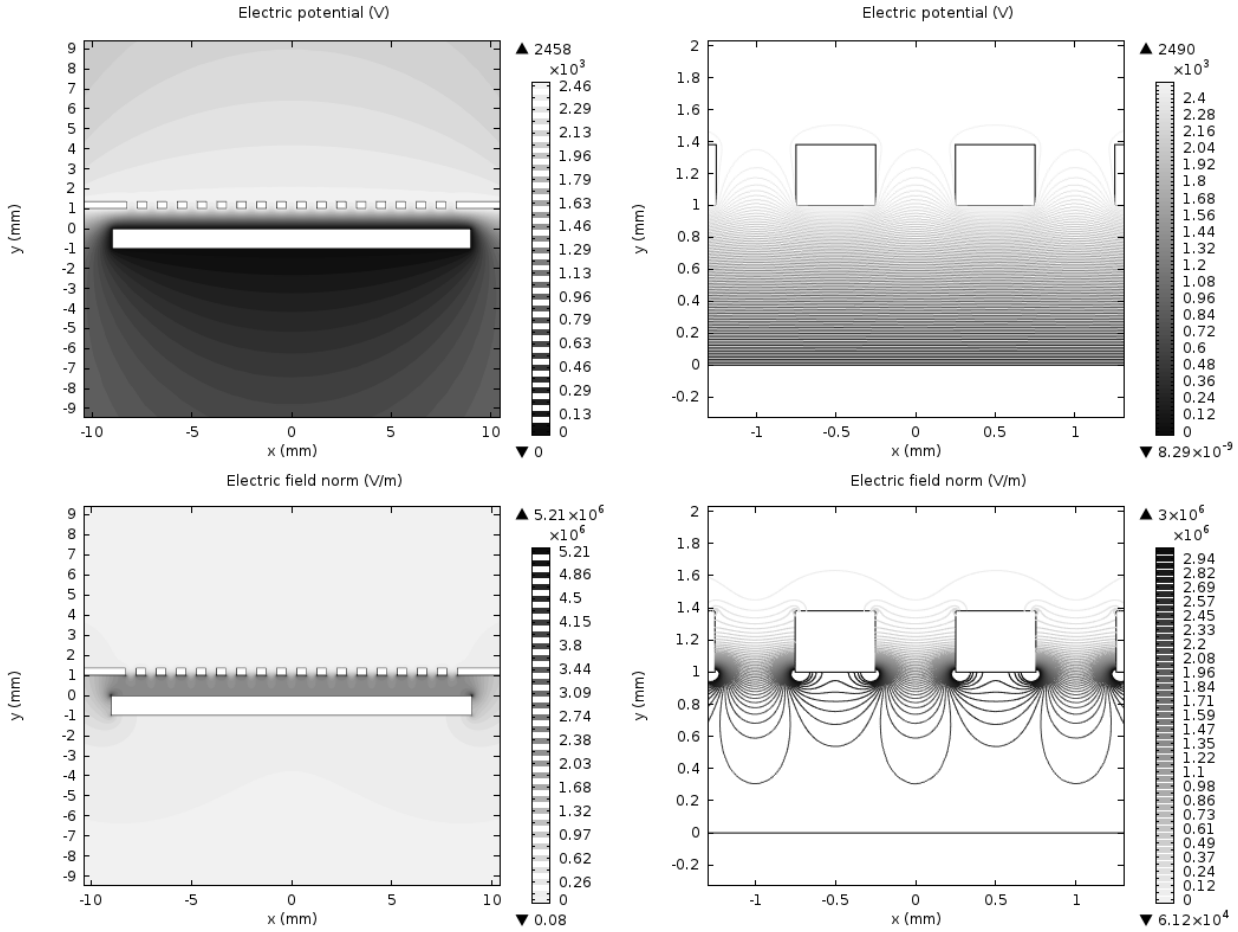

Figure 77: Electric potential (top left and right) and electric field distribution (bottom left and right) for heater/DEP electrode geometry

In order to determine the DEP force in the y-direction (since buoyancy force was only relevant in the y-direction), the electric field magnitude needed to be squared and differentiated with respect to the y-coordinate, i.e. $E^2 = E_x^2 + E_y^2$. This was done at the four x-locations illustrated in Figure 78. The variation of $E_x^2 + E_y^2$ along the y-axis at these locations is shown in Figure 79.

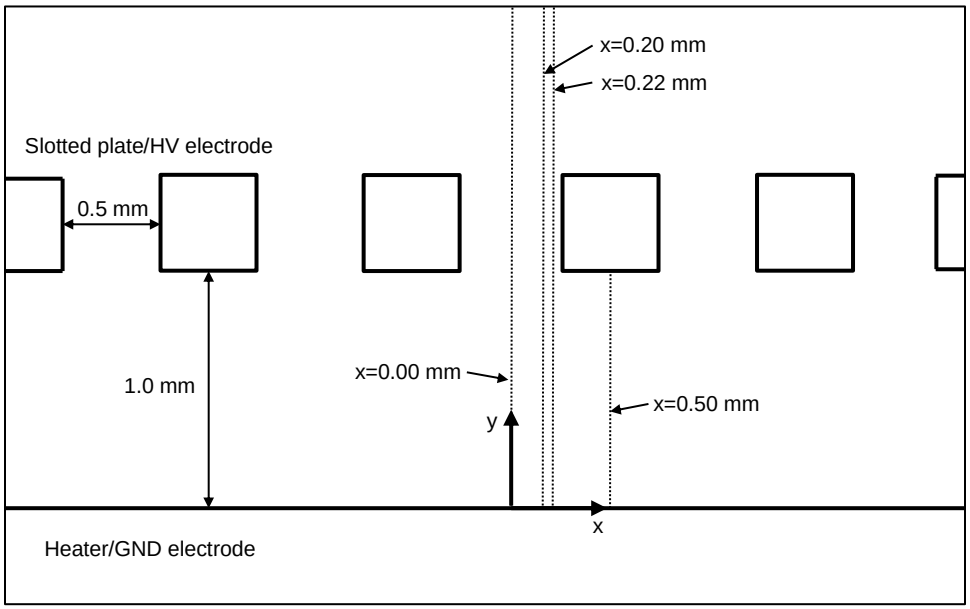

Figure 78: x-locations for electric field calculations

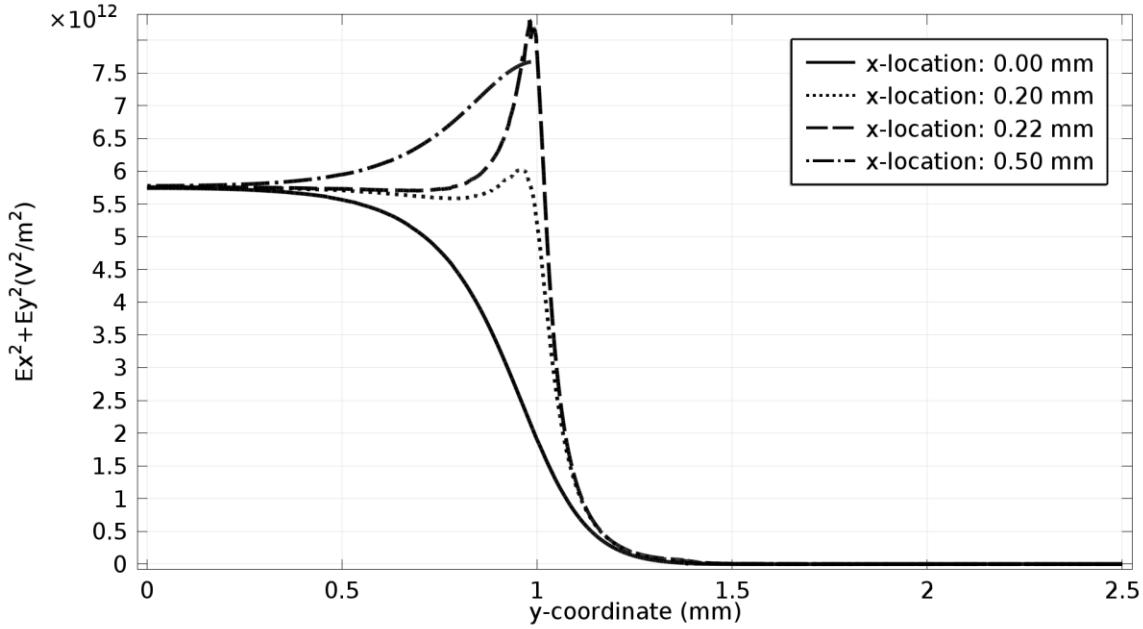

Figure 79: Square of electric field magnitude along y-axis at various x-locations

In the figure above, $E_x^2 + E_y^2$ at the center line (x=0.00 mm) is highest in the vicinity of the ground electrode and decreases along the y-axis through the slot in the high-voltage electrode. There are localized regions of high electric field strength near the slot edges due to the corners, and these are indicated by the sudden increase in $E_x^2 + E_y^2$ at location x=0.22 mm. At x=0.50 mm, the value of $E_x^2 + E_y^2$ increases along the y-axis until y=1.0 mm. Here, there is a discontinuity in the curve since the high voltage electrode surface is reached. The next step in the analysis was to determine the gradient of E^2. The curves in Figure 79 were differentiated with respect to the y-coordinate and used in Eq. (34), along with the above-mentioned values of permittivity to give estimated values of the DEP force magnitude on a bubble of radius 0.25 mm. This was chosen so that the bubble diameter was equal to the slot spacing in the high voltage electrode. The expected buoyancy force on a bubble of radius 0.25 mm was also determined using Eq. (38), where values of liquid and vapor density were found in Table VI. The results are shown in Figure 80.

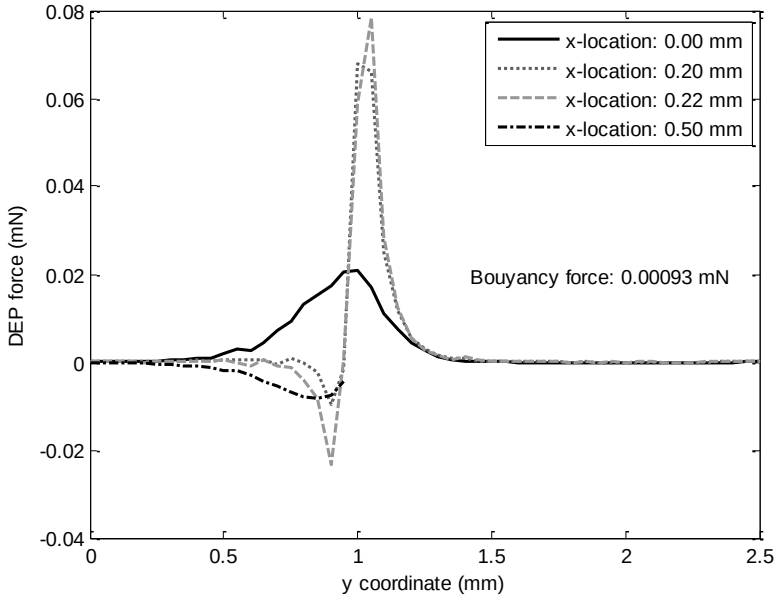

Figure 80: Estimation of DEP force magnitude along y-axis at various x-locations vs. buoyancy force for 0.5 mm bubble diameter

The results of the estimation in Figure 80 show that the DEP force at x=0.20 mm and x=0.22 mm suddenly increases as the high voltage electrode is approached at y=1.0 mm. However, these are only included to illustrate sudden changes in electric field gradient due to the effect of the corners on the electric field distribution. The large surges in DEP force for these locations are not considered for the analysis since the area of effect is only localized to a small region in the electrode slot near the corners. At x=0.00 mm, the DEP force increases along the y-axis up to a maximum value of 0.021 mN at y=1.0 mm. Compared to the buoyancy force of 0.00093 mN, this is two orders of magnitude larger (the ratio of DEP force to buoyancy force is **22 to 1**). At x=0.50 mm, the DEP force decreases along the y-axis and the lowest value is -0.0083 mN. This indicates that the vapor bubbles in the inter-electrode region (in between the slots) would be repelled away from the high-voltage electrode toward the heater surface.

The effect of the DEP force on nucleate boiling heat transfer can be quantified by using one of the simplest transport models developed by Rohsenow [89]. The model assumed that bubble growth and departure from the heater surface during nucleate boiling led to corresponding liquid motion which facilitated convective heat transfer. A single-phase forced convection heat transfer correlation related the bubble Nusselt number, Nu_b, to the bubble Reynolds number, Re_b, the liquid Prandlt number, Pr_l, and several system-specific constants

$$Nu_b = \frac{hL_b}{k_l} = ARe_b^n Pr_l^m \tag{46}$$

The correlation was adapted for nucleate boiling using appropriate length and time scales: L_b was the bubble length scale, which was equal to the bubble departure diameter and a function of the contact angle, surface tension, buoyancy and system characteristics. The velocity scale was taken to be the vapor superficial velocity. The correlation is given by

$$\frac{q"}{\mu_l h_{fg}}\left[\frac{\sigma}{g(\rho_l-\rho_v)}\right]^{\frac{1}{2}} = \left(\frac{1}{C_{sf}}\right)^{\frac{1}{r}} Pr_l^{-\frac{s}{r}}\left[\frac{c_p(T_w-T_{sat})}{h_{fg}}\right]^{\frac{1}{r}} \tag{47}$$

where C_{sf}, r and s are system-specific constants. All other quantities are as previously defined. Equation (47) can be rearranged to solve for the superheat, ΔT

$$\Delta T = (T_w - T_{sat}) = \frac{C_{sf} Pr_l^s h_{fg}}{c_p}\left(\frac{q"}{\mu_l h_{fg}}\right)^r \left[\frac{\sigma}{g(\rho_l-\rho_v)}\right]^{\frac{r}{2}} \tag{48}$$

Fluid properties from Table VI were substituted into Eq. (48) along with prescribed heat fluxes and constants (C_{sf} = 0.0065, r = 0.33 and s = 1.7 were found in the literature from experimental results [90] of nucleate boiling of HCFC-123 on a polished copper surface) to give values of the superheat. The expected effect of the DEP force was determined by using the ratio $F_{DEP}/F_{buoyancy}$ = 22 from the above analysis as a multiplication factor for the gravitational acceleration, g, in Eq.

(48). Therefore, ΔT values were found at 1-g (which represented nucleate boiling in absence of electric field) and compared to the ΔT values at 22-g (which represented nucleate boiling enhanced by dielectrophoretic force). These results were also compared to the experimental data as shown in Figure 81.

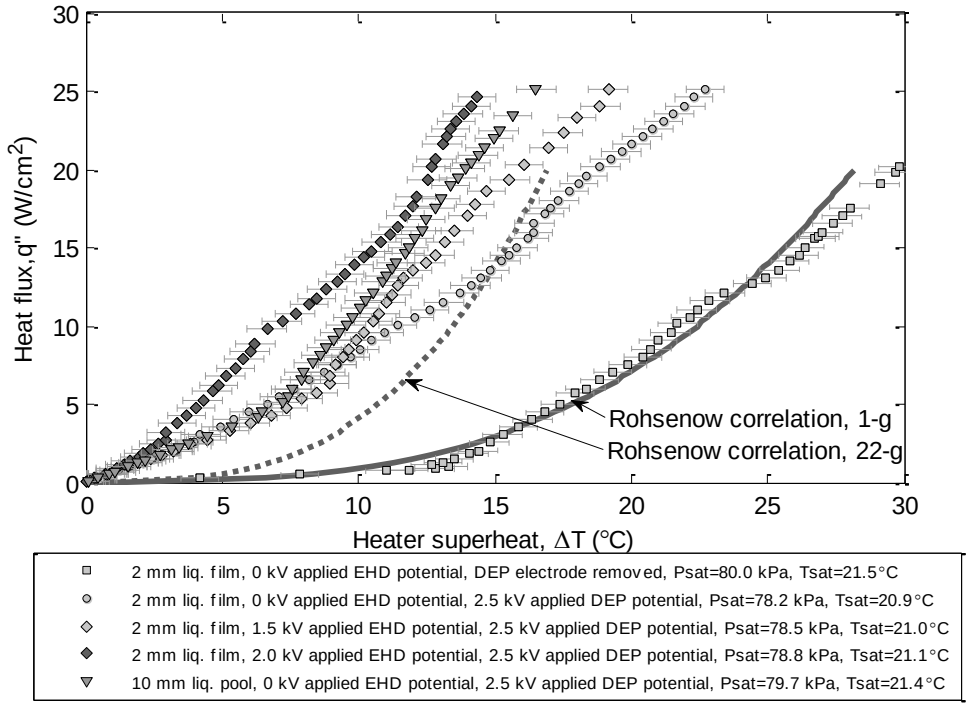

Figure 81: Results of Rohsenow correlation [89] for prescribed heat fluxes, estimated effect of DEP force on boiling curves and comparison to experimental data

The predictions of the correlation showed good agreement with the experimental data for case 1, even for the relatively simple heat transport model chosen. The reduction in superheat values resulting from the imposed increase in gravitational acceleration were also of similar order of magnitude to those found from experimental data of case 2. The largest differences between the Rohsenow correlation prediction (at 22-g) and experimental data of case 2 occurred at low heat flux below 10.0 W/cm^2; the experimental data for case 2 showed notably lower

superheat values. One possible reason for this was the liquid circulation in between the DEP and ground electrodes brought about by EHD conduction pumping mechanism. This caused superheat to be lower than the no-electric field experimental data of case 1. At higher heat fluxes, as mentioned above, the dielectrophoretic force began to dominate and superheat values between the correlation prediction at 22-g and experimental data of case 2 were closer together. The comparisons suggest that there is an optimal range of heat fluxes where the DEP force dominates and EHD conduction has diminished, due to increased presence of vapor bubbles above the heater surface. It is important to mention that the above methodology was only used as an order-of-magnitude analysis. Accurate numerical prediction of liquid film flow boiling and pool boiling in the presence of dielectrophoretic force and EHD conduction pumping of liquid film which takes into account all physical phenomena occurring are beyond the scope of the current work.

5.5 Conclusions

Liquid film flow boiling and pool boiling in the presence of combined EHD conduction pumping and dielectrophoretic force were successfully studied. The results showed remarkable enhancement in heat flux and heat transfer coefficient up to 1217% for a given superheat value when both mechanisms were used. The ratio of electric power input for the combined techniques was only 0.7% compared to the corresponding heater power increase for this level of enhancement. The results also provided new physical insights into the dominant mechanisms of heat transfer enhancement during liquid film flow boiling and pool boiling in the presence and absence of electric fields. For example, they showed that at low heat flux, the EHD conduction-generated liquid film flow allowed for increased forced convection and delayed the onset of nucleate boiling. It was found that increasing the depth of the liquid pool was equivalent to

increasing the applied EHD potential, since both resulted in higher pressure within the liquid which resulted in higher flow rate and lower ΔT. The estimation of the DEP force magnitude (via numerical simulation of electric field) in comparison to the buoyancy force revealed important understanding of the expected enhancement in the liquid film flow boiling curve when the results were applied to a basic heat transport model. They highlighted that the DEP force was only applicable for a certain range of heat flux when nucleate boiling began, although the DEP electrode was responsible for liquid circulation via EHD conduction mechanism in the low heat flux regime.

CHAPTER 6 – CONCLUSIONS AND RECOMMENDATIONS

6.1 Conclusions

The interaction between electric fields and flow fields were successfully studied in the presence and absence of liquid-vapor phase change and presence and absence of gravity, through extensive and varied experimental research. The contributions of this work are as follows:

Operation of a meso-scale EHD conduction-driven single-phase flow heat transport system was confirmed in terrestrial and micro-gravity environments (for the first time). Preliminary single-phase data showed that the absence of gravity did not affect performance of EHD pumps based on conduction mechanism. For two-phase flow terrestrial experiments, the 1 mm diameter open-tube EHD pump was used as the sole driving mechanism for a meso-scale heat transport system. The system was able to transport 7.3W of heat with just 0.015W power input to the EHD pump. Successful recovery from evaporator dryout condition was also achieved for the first time in meso-scale for an EHD-driven two-phase flow heat transport system. A new and improved understanding of the relationship between net EHD pump pressure generation and downstream single- and two-phase flow pressure drop was also gained for this type of geometry and scale. The low mass fluxes generated by the EHD pump made it possible to measure the in-tube, local flow boiling heat transfer coefficients as a function of vapor quality along the evaporator length, providing limited but useful data points for this flow regime. In addition to the above results, the EHD conduction-driven two-phase flow heat transport system was tested successfully for 105 hours of intermittent operation without failure, where 5W of heat transport was consistently achieved with only 0.0042W power input.

EHD conduction pumping was successfully used for electro-wetting of a heater during liquid film flow boiling in terrestrial and micro-gravity conditions. A 62% increase in the critical

heat flux was achieved in terrestrial experiments when the EHD conduction pump was activated. The experiments in micro-gravity were conducted for the first time on board a variable gravity parabolic flight. The transient results showed that the EHD conduction pump had an adverse effect on liquid film flow boiling below 5.0 W/cm^2 due to delayed onset of nucleate boiling but eventually resulted in lowering of heater surface temperature at heat fluxes higher than 7.0 W/cm^2. The most important determination, however, was that the EHD conduction-driven liquid film flow made the boiling process feasible in the absence of gravity. Experiments in liquid film flow boiling driven by EHD conduction pumping were also successfully completed for bare- and copper-plated nanofiber-enhanced surfaces. The results showed that the increased effective surface area and nucleation site density of enhanced surfaces led to lower surface temperatures. Like previous experiments, a delay in ONB and increase in surface temperature was observed during initial activation of the EHD pump at low heat fluxes. Beyond the isolated bubble regime, however, the combination of enhanced surface and EHD conduction pumping resulted in a maximum of 555% enhancement in boiling heat transfer coefficient compared to the bare surface experiment without EHD conduction pumping. The ratio of electric power consumption to heat removal rate was 1:55. The results were valuable as they provided new insights into EHD-driven liquid film flow and liquid-vapor phase change process in the presence and absence of gravity and paved the way for further experiments in micro-gravity. They also showed great promise for development of EHD conduction-driven heat transport systems for both terrestrial and micro-gravity thermal management applications.

Finally, liquid film flow boiling and pool boiling in the presence of combined EHD conduction pumping and dielectrophoretic force were successfully studied. The results provided new physical insights of these boiling processes in the presence and absence of electric fields.

The combination of these two techniques resulted in up to 1217% enhancement in heat flux and heat transfer coefficient for a given superheat value with only 0.7% electric power input (compared to the corresponding heater power increase). A numerical simulation of the electric field for the DEP electrode/heater geometry used in the experiments was conducted. This was used to estimate the DEP force magnitude in comparison to the buoyancy force and applied to a basic heat transport model. The analysis was compared to experimental data to reveal an important understanding of the expected enhancement in the liquid film flow boiling curve. As with all other experimental results, the data were important for applications in thermal management in terrestrial and micro-gravity conditions.

6.2 Recommendations

The meso-scale EHD conduction pump studies of chapters 2 and 3 revealed important insights into the design and performance of the stacked-disc electrode pumps. One of the ways the stainless steel electrodes were micro-polished was to tumble them in fine silica sand for extended periods of time (up to 3 days). This ensured that ion injection was minimized as there were no sharp edges on the electrode surface. The process was shown to improve performance significantly compared to pumps in which electrodes did not undergo this additional step. The electrodes were also soldered to the main bus lines one by one, to ensure electrical contact. Although time-consuming, this was found to be more reliable than the simple press-fit solution used previously. The use of small springs in between electrode pairs (as was done in previous rectangular cross-section pump designs) was also considered but abandoned due to the small metal pieces breaking off and causing shorting between electrodes.

For the liquid film flow boiling experiments of chapters 4 and 5, the working fluid was filtered to $< 2\mu m$, as using a larger filter caused problems during experiments. Particles would

inadvertently end up in the inter-electrode spacing and cause the EHD current to increase, especially if the particle material was conductive. It is recommended that the working fluid be highly filtered to prevent this from happening.

The parabolic flight experiments of chapters 2 and 4 revealed important information regarding certain aspects of the flights. The nature of the parabolic maneuvers is such that a maximum of 25 s of micro-gravity can be achieved. As mentioned above, for the liquid film flow boiling experiments of chapter 4, the results were transient but averaged over several parabolas. The experiments were successful despite the harsh conditions during the parabolic flight, but they are a stepping-stone to future planned experimental work in EHD-conduction driven liquid film flow boiling, on board the orbiting International Space Station Laboratory. The high-quality continuous micro-gravity environment will allow the system to approach true steady state.

For the combined EHD and DEP experiments of chapter 5, the grounding of the heater and EHD electrodes were common. However, these sometimes caused problems towards the end of the experiment as the insulation of the heater wire thinned, causing current to increase slightly. It is recommended that separate grounding be used to prevent this from happening in future experiments.

The experimental results in this work have laid the foundation for different directions of future research in EHD conduction-driven heat transport systems. These include further experimental and numerical studies in smaller scales, such as micro- or even nano-scale heat transport systems (some of these have already begun), flow distribution and control in micro-scale, investigation of new and alternative dielectric working fluids (such as 3M and DuPont Engineered Fluids), and further investigation of electrically driven heat transport systems in micro-gravity.

APPENDIX A – UNCERTAINTY ANALYSIS

A.1 General uncertainty analysis

This section outlines the uncertainty analysis carried out for experimental measurements in this work. The analysis follows the classical works by Kline and McClintock [91] and later by Moffat [92] which clearly demonstrate the procedure for obtaining a correct estimate of the uncertainty for experiments in thermal and fluid sciences. The analysis does not account for factors such as human error in incorrectly reading or connecting a device, for example. These can be corrected if discovered and the experiment can be repeated; thus the uncertainty analysis assumes that the experiments were conducted correctly and provides an estimate of what the errors might be for the given measurement technique and sensor being used.

A.1.1 Systematic or bias errors

Systematic or bias errors refer to fixed errors that are inherent in the measurement devices, and they are caused by many factors. They can result from calibration (since references or standards used in calibration also have bias errors of their own), curve-fitting of calibration data and errors in the data acquisition system caused by environmental effects, for example. Systematic errors must be estimated from manufacturer specifications and accounted for in the overall uncertainty analysis. They are referred to as fixed errors because they are constant for every measurement. For certain calibration references, systematic uncertainty is determined by the smallest measurement that can accurately be made. For example, water-filled manometers are used to calibrate differential pressure transducers in this work. The smallest graduation on the manometer scale determines the systematic uncertainty that will be present each time a reading is made.

A.1.2 Random or precision errors

Random or precision errors arise because when a quantity is measured multiple times, there is bound to be a variation in the measured value which is unavoidable. Random errors arising from repeated measurements are characterized by the mean and standard deviation. For a given measurement, a fixed number of measurements, n, of data points, x_i, are acquired. The arithmetic mean, $\bar{x}$, and standard deviation, s_x, of these are found in order to quantify the scatter of the data. The arithmetic mean is simply the summation of all measured values divided by the number of values.

$$\bar{x} = \frac{1}{n}\sum_{i=1}^{n} x_i \tag{49}$$

The standard deviation is found using

$$s_x = \sqrt{\frac{1}{n-1}\sum_{i=1}^{n}(x_i - \bar{x})^2} \tag{50}$$

where n-1 is used in the denominator. The standard deviation was illustrated in the form of error bars above and below the arithmetic mean in the graphs of results presented in this work.

A.1.3 Propagation of error for derived quantities

In many experiments, the final quantity that is studied must be determined by inputting measured variables into a well-known theoretical model or equation that governs the physical phenomena. A simple example is measuring applied voltage and current through a resistance heater and using Ohm's law to calculate the electric power. The errors in the measurement of voltage and current (both bias and precision errors) will propagate through the equation for

electric power. Each measurement must be weighted to determine its contribution to the total error in the final calculation. The process for performing this analysis is described. If we have a desired result, R, which is a function of measured variables, X_1, X_2, X_3… and so on, we have

$$R = R(X_1, X_2, X_3 \cdots, X_N) \tag{51}$$

After conducting the experiment, we can input the measured variables into a function to determine the result. However, we must also determine the effective uncertainty in the result, δR. The contribution made by the uncertainty in one variable, δX_i, towards the overall uncertainty of the result, δR, can be found using the root-sum-square (RSS) method

$$\delta R = \left\{ \sum_{i=1}^{N} \left(\frac{\partial R}{\partial X_i} \delta X_i \right)^2 \right\}^{\frac{1}{2}} \tag{52}$$

The partial derivatives of R with respect to X_i are known as the sensitivity coefficients. They provide the weighting of each measured variable to determine its contribution to the total error. It is important to mention that the use of the root-sum-square method assumes the following:

1. Each measurement is independent.
2. If repeated observations of each measurement were made, they would follow a Gaussian distribution.
3. The uncertainty in each measurement was initially expressed at the same confidence level.

Calculation of propagation of error can be illustrated by an example. In Chapter 3, Section 3.3, we used Eq. (40) to determine flow boiling heat transfer coefficient from experimentally measured values and it is repeated here for convenience

$$h = \frac{q"}{\Delta T} \tag{53}$$

From this, we see that the heat flux, q" and temperature difference, ΔT were used to determine the heat transfer coefficient. In order to perform the sensitivity analysis, we can apply Eq. (52) as follows to determine the overall uncertainty in the heat transfer coefficient, δh

$$\delta h = \sqrt{\left(\frac{\partial h}{\partial q"}\delta q"\right)^2 + \left(\frac{\partial h}{\partial \Delta T}\delta \Delta T\right)^2} \tag{54}$$

The partial derivatives are found by taking the partial derivatives of Eq. (53)

$$\frac{\partial h}{\partial q"} = \frac{1}{\Delta T} \;\; and \;\; \frac{\partial h}{\partial \Delta T} = -\frac{q"}{(\Delta T)^2} \tag{55}$$

Substituting into Eq. (54) gives

$$\delta h = \sqrt{\left(\frac{1}{\Delta T}\delta q"\right)^2 + \left(-\frac{q"}{(\Delta T)^2}\delta \Delta T\right)^2} \tag{56}$$

Before proceeding, the contributions made by the uncertainty in each variable must be known. Therefore, a similar analysis must first be performed for each individual variable, i.e. the heat flux and temperature difference. However, the individual contributors to the heat transfer coefficient are themselves determined by separate equations which relate measured quantities. The heat flux is determined from measured heater voltage and resistance (which give heater power from Ohm's law) and surface area. The temperature difference is a straightforward subtraction of one measured temperature from another. These analyses were conducted previously and the maximum contributions made by the uncertainty in each variable are as follows:

$$\delta q" = \pm 0.018 \text{ W/cm}^2$$

$$\delta\Delta T = \pm 0.5°C$$

If we consider an example case where the applied heat flux was q" = 1.02 W/cm^2 and measured $\Delta T = 5.12°C$, the heat transfer coefficient would be h = 1992.2 W/m^2·K. Using the above values, the overall uncertainty in the flow boiling heat transfer coefficient from Eq. (56) is $\delta h = \pm 198$ W/m^2·K. Therefore, the value of heat transfer coefficient is reported as h = 1992.2 ±198 W/m^2·K. As a percentage, the overall maximum uncertainty in heat transfer coefficient would be ±10 % for the given operating conditions.

A.2 Temperature measurement

Various T-type thermocouples were used for temperature measurement since they have a wide temperature range (-200 to 350°C). Fine-gage (36 AWG) wire thermocouples were used for surface temperature measurement and stainless steel probe thermocouples were used for bulk fluid temperature measurement. Thermocouples were used in the range -40 to 125°C where they had an accuracy of ±0.5°C according to IEC Tolerance Class 1 EN 60584-2; JIS C 1602. The relationship between thermoelectric voltage, *E*, and temperature t_{90} was given by

$$E = \sum_{i=0}^{n} c_i (t_{90})^i \tag{57}$$

where *E* was in mV, t_{90} was in °C and c_i were the polynomial coefficients. When converting voltage to temperature, inverse polynomial coefficients, D_i, were needed:

$$t_{90} = \sum_{i=0}^{n} D_i (E)^i \tag{58}$$

The coefficients for each thermocouple type for a given temperature range were provided by the National Institute of Standards and Technology, NIST ITS-90 Thermocouple Database. The

National Instruments NI 9213 24-bit ADC data acquisition system (DAQ) was used, with a range of ±78.125 mV. With this resolution, the accuracy of measurement for T-type thermocouples corresponded to < 0.02°C. The data acquisition system had built-in cold junction compensation, eliminating the need for maintaining the reference at a known temperature with a fixed-temperature ice bath, for example.

In some experiments, Resistance Temperature Detectors (RTDs) were used, such as Platinum Resistance Thermometers (PRTs). The probe PRTs were Omega P-M-A-1/8-6-0-P-3 100 Ω (at 0ºC 0.00385Ω/Ω/ºC) with a class "A" accuracy of ± (0.15 + 0.002 |T|)°C. For the maximum temperature this corresponded to ±0.3°C. Resistance was measured using the 4-wire method in order to account for the additional resistance of connecting wires. The Callendar-Van Dusen equation was used to determine the relationship between resistance, *R*, and temperature, *T*, for these standard 100 Ω platinum RTDs, as shown below:

$$R(T) = R_0[1 + AT + BT^2 + CT^3(T - 100)] \quad (-200°C < T < 0°C)$$

$$R(T) = R_0[1 + AT + BT^2] \quad (0°C \leq T \leq 850°C)$$

$$A = 3.9083 \times 10^{-3}{}^{\circ}C^{-1} \tag{59}$$

$$B = -5.775 \times 10^{-7}{}^{\circ}C^{-1}$$

$$C = -4.183 \times 10^{-12}{}^{\circ}C^{-4}$$

where *R* was in *Ω*, *T* was in °C and R_0 was the resistance at 0°C The National Instruments NI 9217 PT100 RTD Analog Input, 100 S/s/ch, 4 Ch module data acquisition system was used for these measurements, with a 24-bit resolution, 50/60 Hz noise rejection and support for 3- and 4-wire RTDs with built-in excitation and automatic detection.

A.3 Pressure measurement

Differential pressure in terrestrial experiments was measured using Validyne DP-15 variable reluctance pressure transducers. The transducers relied on a thin diaphragm which deformed when the pressure on one side exceeded that on the other side. A carrier-demodulator was used to convert the high-frequency carrier signal from the transducer into an analog voltage which was input into the data acquisition system. The accuracy of the transducers was ±10 Pa. Transducers were calibrated in the lab with a manometer as the reference and the range was 0-3.5 in of water or 0-882 Pa. The accuracy of the manometer was determined by the smallest graduation on the scale, which was ±0.01 in, or ±2.5 Pa in hydrostatic pressure of the water column. An example of a typical calibration curve for pressure measurement is given below in Figure 82.

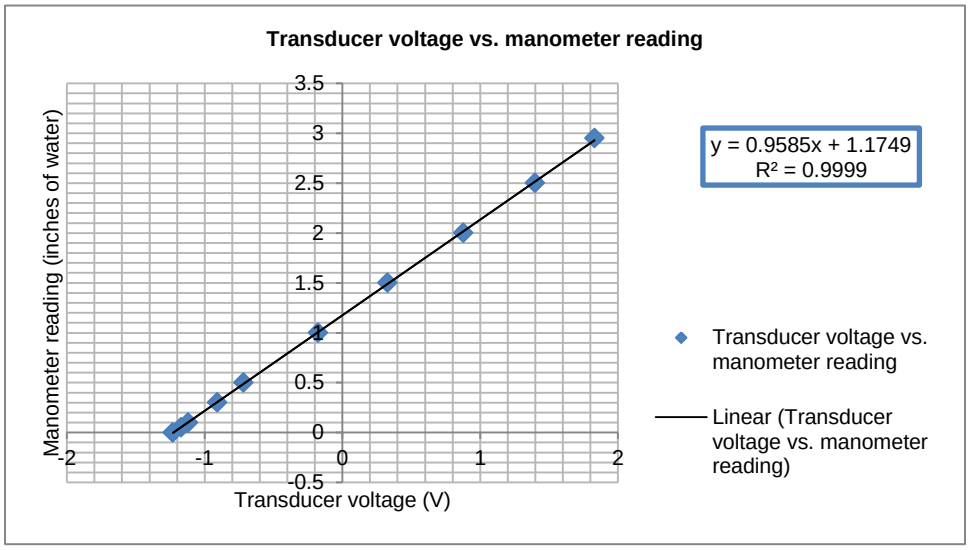

Figure 82: Typical calibration curve for differential pressure transducer

The absolute pressure or system pressure was measured using a Validyne AP-10 pressure transducer, in the range of 0-140 kPa. The accuracy of this transducer was ±350 Pa. For the first parabolic flight experiment, the differential pressure was measured using a Honeywell FP2000

transducer which had an accuracy of ± 6 Pa. For the second parabolic flight experiment, the absolute or system pressure was measured using a Omegadyne PX19 transducer, with an accuracy of ±275 Pa. Voltage signals from the pressure transducers were measured using the National Instruments USB 6211 16-Bit, 250 kS/s M Series multifunction data acquisition system. It had 16 analog inputs (16-bit, 250 kS/s) and 2 analog outputs (16-bit, 250 kS/s) with 4 digital inputs, 4 digital outputs and 2 32-bit counters. The maximum voltage range was -10 V to 10 V with an accuracy of 2.69 mV. The minimum voltage range was -200 mV to 200 mV with an accuracy of 0.088 mV.

A.4 Flow rate

Flow rate was measured using a Sensirion HLQ-60 flow meter. The flow meter was chosen based on the flow rate range, compatibility of wetted parts with the working fluid and cost. It worked by measuring minute changes in energy of the fluid between the inlet and outlet and had an analog output voltage signal. The flow meter was calibrated in the lab using a scale (accuracy of ±2.0g) and stopwatch (accuracy of ±0.01s) to determine the reference flow rate. The calibration curve of analog output voltage vs. flow rate was an exponential and is shown below in Figure 83.

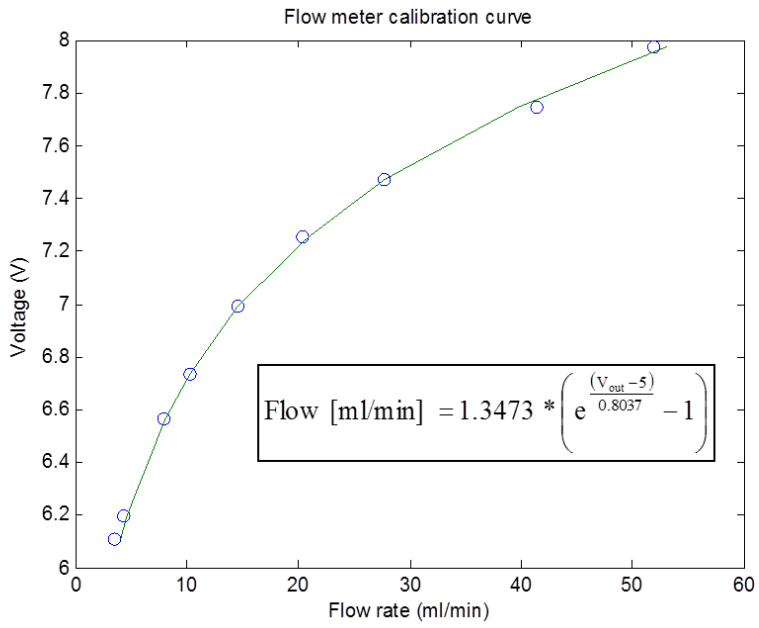

Figure 83: Calibration curve for flow meter

The flow rate range was 0-52 ml/min. The flow detection response time was < 50 ms and accuracy was ±10% of the measured value. Repeatability was 0.2 sec integration time was 1.5% of the measured value or 0.2% of the full scale range. Voltage signals from the flow meters were measured using the National Instruments USB 6211 data acquisition system described above.

A.5 Voltage and current

The heater and evaporator power supplies for terrestrial experiments was a Lambda LMS 9000, which had a voltage range of 0-120 VDC and current range of 0-7 A. The voltage load regulation was 0.05% of the maximum and voltage ripple was 5 mV rms. For remote programming, a 0-5 V signal was used which was linearly proportional to output voltage.

The power supply for the parabolic flight experiments was a TDK-Lambda GEN150-10, which had a range of 0-150 VDC. It had a rated output current of 10 A, which gave a rated output power of 1500 W. The remote voltage programming function had a resolution of 18 mV

and accuracy of ±150 mV. The remote current programming function had a resolution of 1.2 mA and accuracy of ±20 mA. On the other hand, the readback voltage resolution was the same but accuracy was ±300 mV. In the same way, the accuracy of the readback current was ±40 mA. Voltage signals from the power supplies were measured using the National Instruments USB 6211 data acquisition system described above. In addition, analog output voltage signals for control of power supplies were also applied using the same DAQ board.

A.6 EHD voltage and current

The power supply for the EHD pumps in all terrestrial experiments was a Glassman Series EH HV supply which had a range of 0-30 kV DC and 0-3 mA. However, it was only used in the range of 0-1.5 kV. The power supply had built in voltage and current monitors and analog output voltage control. The units could be configured in either fixed-voltage or fixed-current modes. For all experiments in this work, fixed-current mode was used. If the current exceeded the prescribed value (set using a dial on the front panel), the unit automatically shut down to prevent damage to the internal circuitry.

The power supply for EHD pumps in parabolic flight experiments was a Trek 677B which had a range of 0-2 kV DC. The input voltage signal was amplified at a gain of 200 V/V. The current range was 0-5 mA. The output voltage had a resolution of 1V. The voltage monitor had a DC accuracy better than 0.1 % of full scale, with offset voltage < 5 mV and output noise < 10 mV rms. The current monitor had a scale factor of 1 V/mA and DC accuracy better than 0.1 % of full scale. Voltage signals from the power supplies were measured using the National Instruments USB 6211 data acquisition system described above. In addition, analog output voltage signals for control of power supplies were also applied using the same DAQ board.

A.7 Acceleration due to gravity

A Honeywell accelerometer (model MA311) was employed to measure the gravitational acceleration throughout the duration of both variable gravity parabolic flights. The MA311 was a DC response accelerometer with an input voltage of 12-24 Vdc and an output of 100 mV/G. The model that was used for the flights had a range of ± 2g and accuracy of ± 0.02g. Voltage signals from the accelerometer was measured using the National Instruments USB 6211 data acquisition system described above.

APPENDIX B – NUMERICAL SIMULATION RESULTS FOR ENGINEERING DESIGN

B.1 Meso loop evaporator

In order to explain differences between the experimental results for the boiling heat transfer coefficient in section 3.6, a 2-D axisymmetric numerical simulation was performed for heat conduction within the copper evaporator tube (the tube length was 110 mm and wall thickness was 0.5 mm). The reason for this was that in the downstream region of the evaporator, where quality approached 1, heat transfer to the fluid was severely diminished. However, when calculating heat transfer coefficient, the assumption was made that the heat flux was uniform and only important in the radial direction. Axial heat flux was considered negligible but this assumption became less valid at the end of the tube where it had the potential to be significant. The results indeed showed that axial conduction accounted for up to 10% of heat load compared to radial conduction, effectively decreasing the heat transfer coefficients at highest vapor quality, shown in Figure 47. If this correction was applied, there would be better overall agreement between experimental data and the predictions of both correlations for vapor quality >0.5. The results of the numerical simulation are shown in Figure 84 and Figure 85 for the temperature distribution and radial heat flux distribution, respectively.

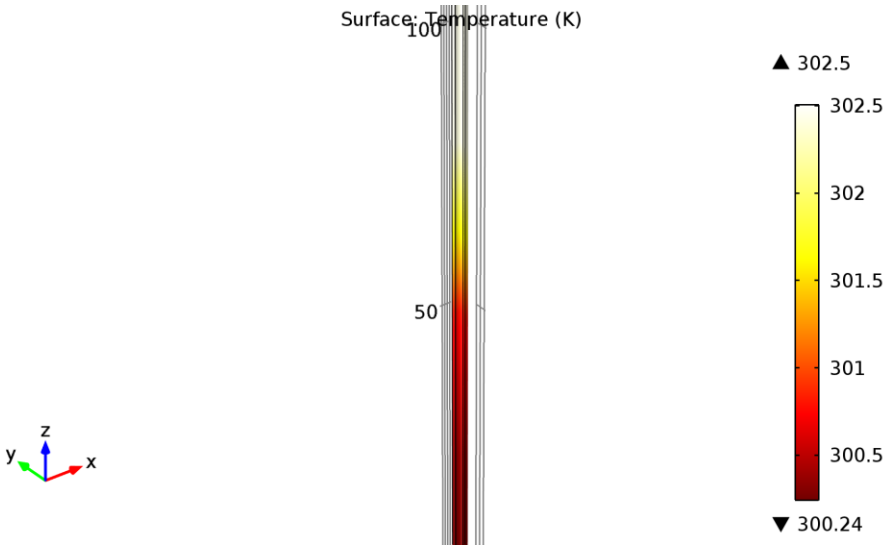

Figure 84: Copper evaporator tube temperature distribution

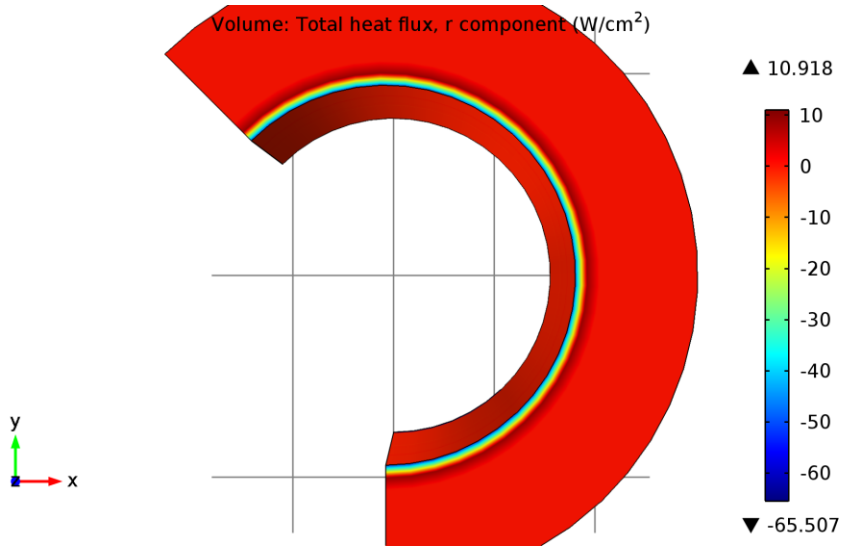

Figure 85: Copper evaporator tube radial heat flux distribution

B.2 Liquid film flow boiling ceramic heater

A 3-D numerical simulation of heat conduction within the ceramic heater piece was performed in order to determine the heat flux distribution and temperature on the top surface of the heater. The reason was that there was a difference between the surface areas of the square printed resistor (a limitation of the fabrication process) and the circular ceramic substrate (a

requirement for the heat transport system in the radial configuration). In addition, since temperature was measured on the bottom surface of the heater, a determination of the temperature on the top surface was necessary. The simulation was performed for all heat loads to determine the temperature difference between the top ($T_{top\_surface}$) and bottom ($T_{bottom\_surface}$) surfaces as shown in Figure 86. The following procedure was used:

1. ΔT was first calculated using ($T_{bottom\_surface} - T_{sat}$) from the measured experimental data.
2. Each value of ΔT and corresponding heat flux were used to determine the boiling heat transfer coefficient.
3. The heat transfer coefficient was used as a boundary condition in the 3D numerical simulation of heat conduction within the ceramic heater substrate.
4. $T_{top\_surface}$ was found from the above numerical simulation and used to determine a new, corrected ΔT.
5. The new corrected value of ΔT was used iteratively until successive values of $T_{top\_surface}$ were the same.

In addition, the heat flux was not calculated using the whole area of the circular substrate (the substrate had a diameter of 2.2 cm which gave a total area of 3.8 cm^2). Instead, a smaller portion with an area of 1.67 cm^2 was used for the heat flux calculation. This was based on numerical simulation of the heat flux distribution on the top surface of the heater. The analysis showed that up to 90% of the heat was dissipated through the central area of the heater and only 10% was dissipated through the outer periphery even for the most conservative parameters. As mentioned above, the reason for this uneven distribution was the use of the smaller square 1.0 cm^2 printed resistor to generate heat for the much larger circular 3.8 cm^2 substrate. The heat

dissipation and corresponding areas from the numerical analysis were therefore used as weighting functions to determine the effective area which was then used to determine the true heat flux, as shown in Figure 87 and Figure 88. Therefore, the values of ΔT in the results of section 4.2 reported in Figure 60, Figure 61 and Figure 62 were corrected according the above analysis.

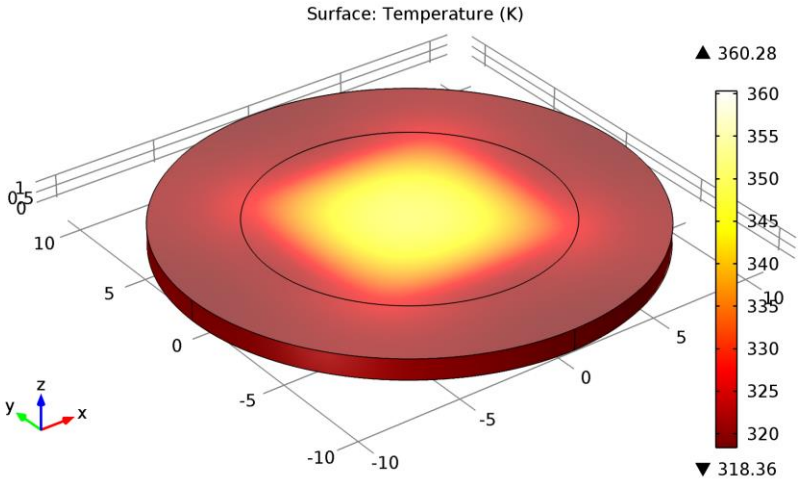

Figure 86: Ceramic heater temperature distribution for q = 35W, non-uniform heat transfer coefficient

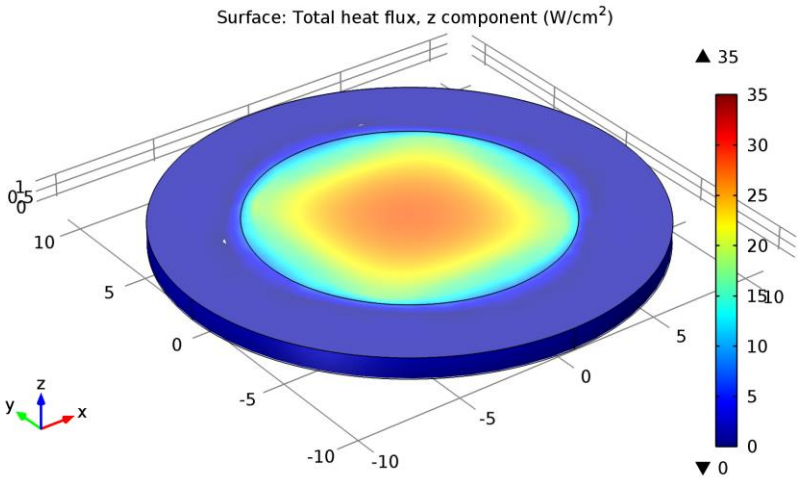

Figure 87: Ceramic heater axial heat flux for q = 35W, non-uniform heat transfer coefficient

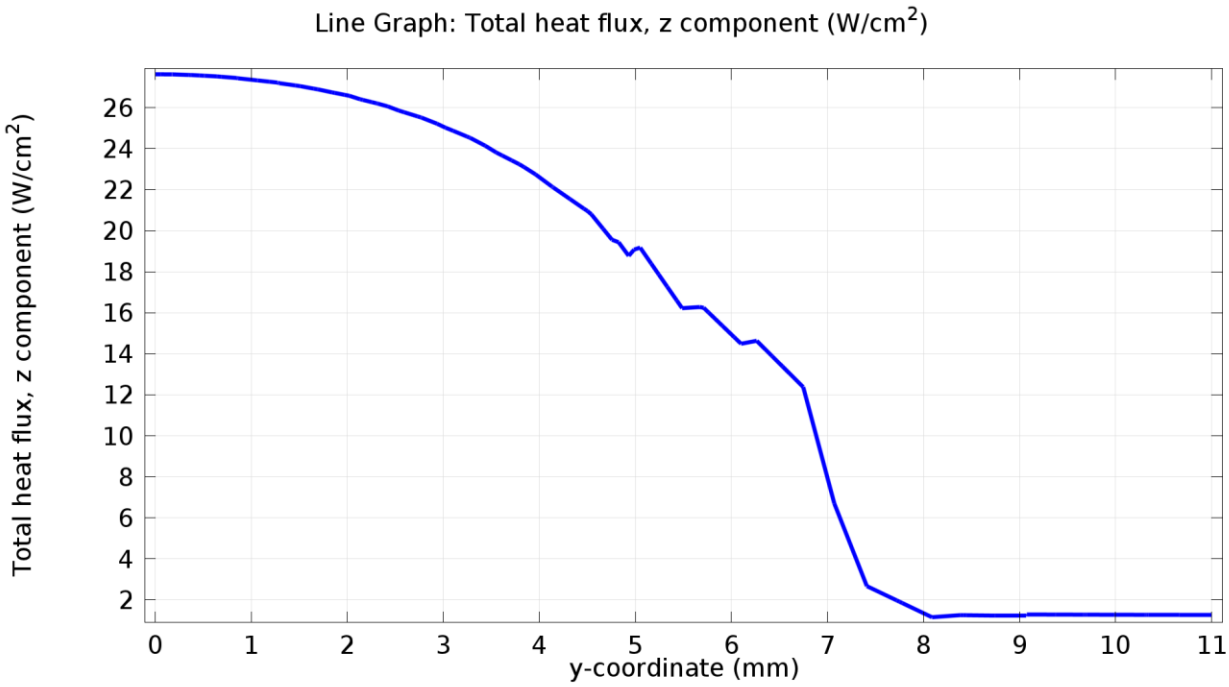

Figure 88: Ceramic heater axial heat flux for q = 35W, non-uniform heat transfer coefficient

B.3 Liquid film flow boiling copper heater

A 2-D axisymmetric numerical simulation of steady-state heat conduction within the copper heater piece used in the experiments of chapter 4, section 4.3 and chapter 5 was performed at all expected heat loads. A uniform heat was applied on the side wall where the nichrome heater wire was wrapped for the actual experiment. For the top surface, a convection boundary condition was used based on the maximum expected heat flux and ΔT. All other surfaces had an insulation boundary condition. The results of the simulation confirmed a uniform heat flux on the top surface of the copper piece. They also showed that the maximum difference in temperature at the location of the thermocouple (as illustrated in Figure 63) and corresponding temperature on the top surface of the heater was 0.9°C. It is important to note that this only occurred for heat flux greater than 20.0 W/cm^2. Therefore, for the majority of heat loads the top surface temperature measurement via embedded thermocouple was justified. The temperature

distribution is shown in Figure 89 and Figure 90 and arrows indicating heat flux are also shown in the latter figure.

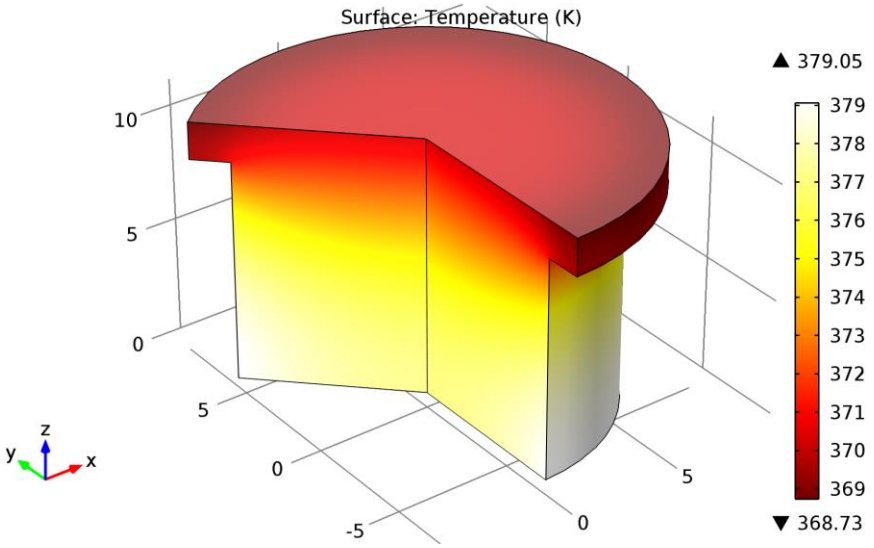

Figure 89: Temperature distribution for q" = 35 W/cm^2

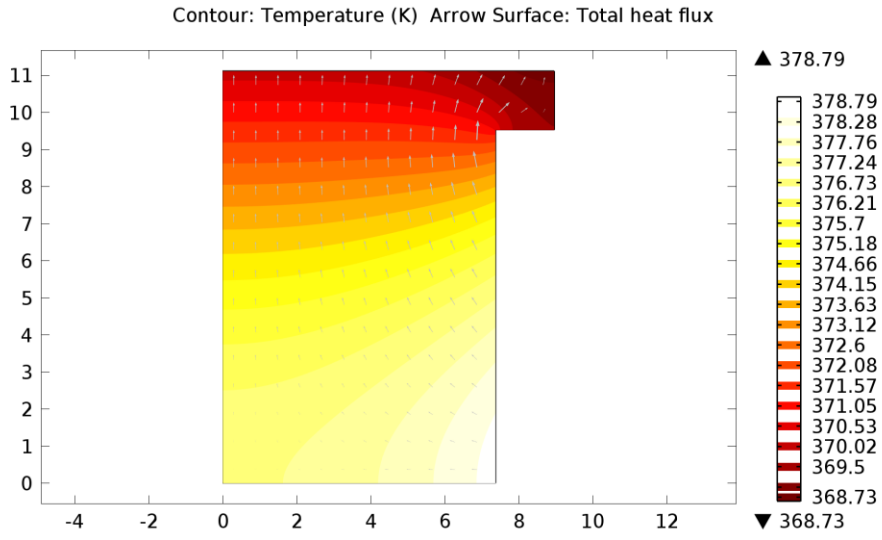

Figure 90: Temperature distribution and arrows showing heat flux for q" = 35 W/cm^2

BIBLIOGRAPHY

[1] J. R. Melcher, *Continuum Electromechanics*, Cambridge, MA: MIT Press, 1981.

[2] J. Seyed-Yagoobi, "Electrohydrodynamic Pumping of Dielectric Liquids," *Journal of Electrostatics,* vol. 63, no. 6–10, pp. 861-869, 6//, 2005.

[3] O. M. Stuetzer, "Ion Drag Pressure Generation," *Journal of Applied Physics,* vol. 30, no. 7, pp. 984-994, 1959.

[4] W. F. Pickard, "Ion Drag Pumping. I. Theory," *Journal of Applied Physics,* vol. 34, no. 2, pp. 246-250, 1963.

[5] W. F. Pickard, "Ion Drag Pumping. II. Experiment," *Journal of Applied Physics,* vol. 34, no. 2, pp. 251-258, 1963.

[6] G. H. Krawinkel, "Efficiency of an Electrostatic Pump," *Zeitschrift für angewandte Physik,* vol. 25, no. 5, pp. 302-6, 1968.

[7] P. Foroughi, A. Shooshtari, S. Dessiatoun, and M. M. Ohadi, "Experimental Characterization of an Electrohydrodynamic Micropump for Cryogenic Spot Cooling Applications," *Heat Transfer Engineering,* vol. 31, no. 2, pp. 119-126, 2010/02/01, 2010.

[8] S. Mohammed Hasnain, A. Bakshi, P. Ravi Selvaganapathy, and C. Y. Ching, "On the Modeling and Simulation of Ion Drag Electrohydrodynamic Micropumps," *ASME Journal of Fluids Engineering,* vol. 133, no. 5, pp. 051102-051102, 2011.

[9] J. Darabi, and W. Haixia, "Development of an Electrohydrodynamic Injection Micropump and Its Potential Application in Pumping Fluids in Cryogenic Cooling Systems," *IEEE Journal of Microelectromechanical Systems,* vol. 14, no. 4, pp. 747-755, 2005.

[10] J. R. Melcher, "Traveling-Wave Induced Electroconvection," *Physics of Fluids,* vol. 9, no. 8, pp. 1548-1555, 1966.

[11] K. Brand, and J. Seyed-Yagoobi, "Experimental Study of Electrohydrodynamic Induction Pumping of a Dielectric Micro Liquid Film in External Horizontal Condensation Process," *ASME Journal of Heat Transfer,* vol. 125, no. 6, pp. 1096-1105, 2003.

[12] M. R. Pearson, and J. Seyed-Yagoobi, "Advances in Electrohydrodynamic Conduction Pumping," *IEEE Transactions on Dielectrics and Electrical Insulation,* vol. 16, no. 2, pp. 424-434, 04, 2009.

[13] P. Atten, and J. Seyed-Yagoobi, "Electrohydrodynamically induced dielectric liquid flow through pure conduction in point/plane geometry," *IEEE Transactions on Dielectrics and Electrical Insulation,* vol. 10, no. 1, pp. 27-36, Feb, 2003.

[14] S.-I. Jeong, J. Seyed-Yagoobi, and P. Atten, "Theoretical/numerical Study of Electrohydrodynamic Pumping Through Conduction Phenomenon," *IEEE Transactions on Industry Applications,* vol. 39, no. 2, pp. 355-361, Mar-Apr, 2003.

[15] S.-I. Jeong, and J. Seyed-Yagoobi, "Fluid Circulation in an Enclosure Generated by Electrohydrodynamic Conduction Phenomenon," *IEEE Transactions on Dielectrics and Electrical Insulation,* vol. 11, no. 5, pp. 899-910, 2004.

[16] Y. Feng, and J. Seyed-Yagoobi, "Understanding of Electrohydrodynamic Conduction Pumping Phenomenon," *Physics of Fluids (1994-present),* vol. 16, no. 7, pp. 2432-2441, 2004.

[17] Y. Feng, and J. Seyed-Yagoobi, "Electrical Charge Transport and Energy Conversion with Fluid Flow during Electrohydrodynamic Conduction Pumping," *Physics of Fluids (1994-present),* vol. 19, no. 5, pp. 057102, 2007.

[18] M. Yazdani, and J. Seyed-Yagoobi, "Numerical Investigation of Electrohydrodynamic-Conduction Pumping of Liquid Film in the Presence of Evaporation," *ASME Journal of Heat Transfer,* vol. 131, no. 1, pp. 011602-011602, 2008.

[19] M. Yazdani, and J. Seyed-Yagoobi, "Electrically Induced Dielectric Liquid Film Flow Based on Electric Conduction Phenomenon," *IEEE Transactions on Dielectrics and Electrical Insulation,* vol. 16, no. 3, pp. 768-777, 2009.

[20] M. Yazdani, and J. Seyed-Yagoobi, "Fluid Circulation Within a Spherical Reservoir With EHD Conduction Pumping," *IEEE Transactions on Industry Applications,* vol. 45, no. 4, pp. 1491-1498, 2009.

[21] M. Yazdani, and J. Seyed-Yagoobi, "Thermal Homogenization in Spherical Reservoir by Electrohydrodynamic Conduction Phenomenon," *ASME Journal of Heat Transfer,* vol. 131, no. 9, pp. 094502-094502, 2009.

[22] M. Yazdani, and J. Seyed-Yagoobi, "An Electrically Driven Impinging Liquid Jet for Direct Cooling of Heated Surfaces," *IEEE Transactions on Industry Applications,* vol. 46, no. 2, pp. 650-658, 2010.

[23] M. Yazdani, and J. Seyed-Yagoobi, "Heat Transfer Augmentation of Parallel Flows by Means of Electric Conduction Phenomenon in Macro- and Microscales," *ASME Journal of Heat Transfer,* vol. 132, no. 6, pp. 062402-062402, 2010.

[24] M. Yazdani, and J. Seyed-Yagoobi, "Effect of Charge Mobility on Dielectric Liquid Flow Driven by EHD Conduction Phenomenon," *Journal of Electrostatics,* vol. 72, no. 4, pp. 285-294, 8//, 2014.

[25] M. Yazdani, and J. Seyed-Yagoobi, "Heat Transfer Enhancement of Backstep Flow by Means of EHD Conduction Pumping," *International Journal of Heat and Mass Transfer,* vol. 73, no. 0, pp. 819-825, 6//, 2014.

[26] L. Onsager, "Deviations from Ohm's Law in Weak Electrolytes," *The Journal of Chemical Physics,* vol. 2, no. 9, pp. 599-615, 1934.

[27] S.-I. Jeong, and J. Seyed-Yagoobi, "Experimental Study of Electrohydrodynamic Pumping through Conduction Phenomenon," *Journal of Electrostatics,* vol. 56, no. 2, pp. 123-133, 9/26/, 2002.

[28] S.-I. Jeong, and J. Seyed-Yagoobi, "Innovative Electrode Designs for Electrohydrodynamic Conduction Pumping," *IEEE Transactions on Industry Applications,* vol. 40, no. 3, pp. 900-904, 2004.

[29] Y. Feng, and J. Seyed-Yagoobi, "Control of Liquid Flow Distribution Utilizing EHD Conduction Pumping Mechanism," *IEEE Transactions on Industry Applications,* vol. 42, no. 2, pp. 369-377, 2006.

[30] M. Siddiqui, and J. Seyed-Yagoobi, "Experimental Study of Pumping of Liquid Film With Electric Conduction Phenomenon," *IEEE Transactions on Industry Applications,* vol. 45, no. 1, pp. 3-9, 2009.

[31] M. R. Pearson, and J. Seyed-Yagoobi, "Experimental Study of EHD Conduction Pumping at the Meso- and Micro-scale," *Journal of Electrostatics,* vol. 69, no. 6, pp. 479-485, 12//, 2011.

[32] S. R. Mahmoudi, K. Adamiak, G. S. P. Castle, and M. Ashjaee, "Study of Electrohydrodynamic Micropumping Through Conduction Phenomenon," *IEEE Transactions on Industry Applications,* vol. 47, no. 5, pp. 2224-2234, 2011.

[33] R. Gharraei, E. Esmaeilzadeh, M. Hemayatkhah, and J. Danaeefar, "Experimental Investigation of Electrohydrodynamic Conduction Pumping of Various Liquids Film using Flush Electrodes," *Journal of Electrostatics,* vol. 69, no. 1, pp. 43-53, 2//, 2011.

[34] M. Hemayatkhah, R. Gharraei, and E. Esmaeilzadeh, "Flow Pattern Visualization of Liquid Film Conduction Pumping Using Flush Mounted Electrodes," *Experimental Thermal and Fluid Science,* vol. 35, no. 6, pp. 933-938, 9//, 2011.

[35] R. Hanaoka, S. Takata, M. Murakumo, and H. Anzai, "Properties of Liquid Jet Induced by Electrohydrodynamic Pumping in Dielectric Liquids," *Electrical Engineering in Japan,* vol. 138, no. 4, pp. 1-9, 2002.

[36] R. Hanaoka, H. Nakamichi, S. Takata, and T. Fukami, "Distinctive Flow Properties of Liquid Jet Generated by EHD Pump and Conical Nozzle," *Electrical Engineering in Japan,* vol. 154, no. 1, pp. 9-19, 2006.

[37] R. Hanaoka, I. Takahashi, S. Takata, T. Fukami, and Y. Kanamaru, "Properties of EHD Pump with Combination of Rod-to-rod and Meshy Parallel Plates Electrode Assemblies," *IEEE Transactions on Dielectrics and Electrical Insulation,* vol. 16, no. 2, pp. 440-447, 2009.

[38] J. E. Bryan, and J. Seyed-Yagoobi, "Heat Transport Enhancement of Monogroove Heat Pipe with Electrohydrodynamic Pumping," *AIAA Journal of Thermophysics and Heat Transfer,* vol. 11, no. 3, pp. 454-460, 1997.

[39] Y. Feng, and J. Seyed-Yagoobi, "Control of Adiabatic Two-phase Dielectric Fluid Flow Distribution with EHD Conduction Pumping," *Journal of Electrostatics,* vol. 64, no. 7–9, pp. 621-627, 7//, 2006.

[40] S.-I. Jeong, and J. Didion, "Thermal Control Utilizing an Electrohydrodynamic Conduction Pump in a Two-Phase Loop With High Heat Flux Source," *ASME Journal of Heat Transfer,* vol. 129, no. 11, pp. 1576-1583, 2007.

[41] S.-I. Jeong, and J. Didion, "Performance Characteristics of Electrohydrodynamic Conduction Pump in Two-Phase Loops," *AIAA Journal of Thermophysics and Heat Transfer,* vol. 22, no. 1, pp. 90-97, 2008/01/01, 2008.

[42] M. R. Pearson, and J. Seyed-Yagoobi, "Electrohydrodynamic Conduction Driven Single- and Two-Phase Flow in Microchannels with Heat Transfer," *ASME Journal of Heat Transfer,* vol. 135, no. 10, pp. 101701-101701, 2013.

[43] M. R. Pearson, and J. Seyed-Yagoobi, "EHD Conduction-Driven Enhancement of Critical Heat Flux in Pool Boiling," *IEEE Transactions on Industry Applications,* vol. 49, no. 4, pp. 1808-1816, 2013.

[44] M. R. Pearson, and J. Seyed-Yagoobi, "Experimental Study of Linear and Radial Two-Phase Heat Transport Devices Driven by Electrohydrodynamic Conduction Pumping," *ASME Journal of Heat Transfer,* vol. 137, no. 2, pp. 022901, 02, 2015.

[45] T. B. Jones, *Electromechanics of Particles,* Cambridge, UK: Cambridge University Press, 2005.

[46] T. B. Jones, and G. W. Bliss, "Bubble Dielectrophoresis," *Journal of Applied Physics,* vol. 48, no. 4, pp. 1412-1417, 1977.

[47] H. A. Pohl, *Dielectrophoresis: The Behavior of Neutral Matter in Nonuniform Electric Fields,* Cambridge, UK: Cambridge University Press, 1978.

[48] A. R. Von Hippel, *Dielectrics and Waves,* New York: John Wiley & Sons, Inc, 1954.

[49] J. M. Crowley, *Fundamentals of Applied Electrostatics*: John Wiley & Sons, 1986.

[50] M. R. Pearson, and J. Seyed-Yagoobi, "Numerical Study of Dielectric Fluid Bubble Behavior Within Diverging External Electric Fields," *ASME Journal of Heat Transfer,* vol. 130, no. 3, pp. 032901-032901, 2008.

[51] P. Wang, D. J. Swaffield, P. L. Lewin, and G. Chen, "Thermal Bubble Motion in Liquid Nitrogen under Nonuniform Electric Fields," *IEEE Transactions on Dielectrics and Electrical Insulation,* vol. 15, no. 3, pp. 626-634, 2008.

[52] J. Seyed-Yagoobi, C. A. Geppert, and L. M. Geppert, "Electrohydrodynamically Enhanced Heat Transfer in Pool Boiling," *ASME Journal of heat transfer,* vol. 118, no. 1, pp. 233, 1996.

[53] J. Seyed-Yagoobi, J. T. Hardesty, P. Raghupathi, and J. E. Bryan, "Experimental Study of Electrohydrodynamically Augmented Pool Boiling Heat Transfer on Smooth and Enhanced Tubes," *Journal of Electrostatics,* vol. 40–41, no. 0, pp. 597-602, 6//, 1997.

[54] Y. C. Kweon, and M. H. Kim, "Experimental Study on Nucleate Boiling Enhancement and Bubble Dynamic Behavior in Saturated Pool Boiling using a Nonuniform DC Electric Field," *International Journal of Multiphase Flow,* vol. 26, no. 8, pp. 1351-1368, 8/1/, 2000.

[55] Y. Hristov, D. Zhao, D. B. R. Kenning, K. Sefiane, and T. G. Karayiannis, "A Study of Nucleate Boiling and Critical Heat Flux with EHD Enhancement," *Heat and Mass Transfer,* vol. 45, no. 7, pp. 999-1017, 2009/05/01, 2009.

[56] I. Kano, Y. Higuchi, and T. Chika, "Development of Boiling Type Cooling System Using Electrohydrodynamics Effect," *ASME Journal of Heat Transfer,* vol. 135, no. 9, pp. 091301-091301, 2013.

[57] C. Herman, E. Iacona, I. B. Földes, G. Suner, and C. Milburn, "Experimental Visualization of Bubble Formation from an Orifice in Microgravity in the Presence of Electric Fields," *Experiments in Fluids,* vol. 32, no. 3, pp. 396-412, 2002/03/01, 2002.

[58] V. Dhir, G. Warrier, E. Aktinol, D. Chao, J. Eggers, W. Sheredy, and W. Booth, "Nucleate Pool Boiling Experiments (NPBX) on the International Space Station," *Microgravity Science and Technology,* vol. 24, no. 5, pp. 307-325, 2012/11/01, 2012.

[59] R. Raj, J. McQuillen, and J. Kim, "Pool Boiling Heat Transfer on the International Space Station: Experimental Results and Model Verification," *ASME Journal of Heat Transfer,* vol. 134, no. 10, pp. 101504-101504, 2012.

[60] T. J. Snyder, and J. N. Chung, "Terrestrial and Microgravity Boiling Heat Transfer in a Dielectrophoretic Force Field," *International Journal of Heat and Mass Transfer,* vol. 43, no. 9, pp. 1547-1562, 5/1/, 2000.

[61] P. Di Marco, and W. Grassi, "Effects of External Electric Field on Pool Boiling: Comparison of Terrestrial and Microgravity Data in the ARIEL Experiment," *Experimental Thermal and Fluid Science,* vol. 35, no. 5, pp. 780-787, 7//, 2011.

[62] V. K. Patel, F. Robinson, J. Seyed-Yagoobi, and J. Didion, "Terrestrial and Microgravity Experimental Study of Microscale Heat-Transport Device Driven by Electrohydrodynamic Conduction Pumping," *IEEE Transactions on Industry Applications,* vol. 49, no. 6, pp. 2397-2401, 2013.

[63] DuPont, "DuPont HCFC-123 Properties, Uses, Storage and Handling," *DuPont Fluorochemicals, Wilmington, DE,* 2005.

[64] DuPont, "Thermodynamic Properties of HCFC-123 Refrigerant," *DuPont Fluorochemicals, Wilmington, DE*, 2005.

[65] H. B. Chae, J. W. Schmidt, and M. R. Moldover, "Surface Tension of Refrigerants R123 and R134a," *Journal of Chemical & Engineering Data,* vol. 35, no. 1, pp. 6-8, 1990/01/01, 1990.

[66] J. E. Bryan, "Fundamental Study of Electrohydrodynamically Enhanced Convective and Nucleate Boiling Heat Transfer," Department of Mechanical Engineering, Texas A&M University, College Station, TX, 1998.

[67] ZeroGravityCorporation, *Interface Control Document Boeing 727-200*, Revision A2 ed.: Revision A2, 2009.

[68] V. K. Patel, and J. Seyed-Yagoobi, "A Mesoscale Electrohydrodynamic-Driven Two-Phase Flow Heat Transport Device in Circular Geometry and In-Tube Boiling Heat Transfer Coefficient Under Low Mass Flux," *ASME Journal of Heat Transfer,* vol. 137, no. 4, pp. 041504-041504, 2015.

[69] V. K. Patel, and J. Seyed-Yagoobi, "Long-Term Performance Evaluation of Microscale Two-Phase Heat Transport Device Driven by EHD Conduction," *IEEE Transactions on Industry Applications,* vol. 50, no. 5, pp. 3011-3016, 2014.

[70] A. Faghri, *Heat Pipe Science and Technology*, p.^pp. Chap. 4., New York, USA: Taylor & Francis, 1995.

[71] I. Mudawar, "Two-Phase Microchannel Heat Sinks: Theory, Applications, and Limitations," *ASME Journal of Electronic Packaging,* vol. 133, no. 4, pp. 041002-041031, Dec, 2011.

[72] S. M. Sri-Jayantha, G. McVicker, K. Bernstein, and J. U. Knickerbocker, "Thermomechanical Modeling of 3D Electronic Packages," *IBM Journal of Research and Development,* vol. 52, no. 6, pp. 623-634, Nov, 2008.

[73] W. Qu, and I. Mudawar, “Flow Boiling Heat Transfer in Two-phase Micro-channel Heat Sinks—I. Experimental Investigation and Assessment of Correlation Methods,” *International Journal of Heat and Mass Transfer,* vol. 46, no. 15, pp. 2755-2771, 7//, 2003.

[74] S. S. Bertsch, E. A. Groll, and S. V. Garimella, “Review and Comparative Analysis of Studies on Saturated Flow Boiling in Small Channels,” *Nanoscale and Microscale Thermophysical Engineering,* vol. 12, no. 3, pp. 187-227, 2008/09/05, 2008.

[75] T. Harirchian, and S. V. Garimella, “Effects of Channel Dimension, Heat Flux, and Mass Flux on Flow Boiling Regimes in Microchannels,” *International Journal of Multiphase Flow,* vol. 35, no. 4, pp. 349-362, Apr, 2009.

[76] S. G. Kandlikar, “History, Advances, and Challenges in Liquid Flow and Flow Boiling Heat Transfer in Microchannels: A Critical Review,” *ASME Journal of Heat Transfer,* vol. 134, no. 3, pp. 034001-034001, 2012.

[77] J. C. Mankins, "Technology Readiness Levels: A White Paper," A. C. Office, ed., Office of Space Access and Technology, NASA, 1995.

[78] T.-H. Yen, N. Kasagi, and Y. Suzuki, “Forced Convective Boiling Heat Transfer in Microtubes at Low Mass and Heat Fluxes,” *International Journal of Multiphase Flow,* vol. 29, no. 12, pp. 1771-1792, 12//, 2003.

[79] S. G. Kandlikar, and P. Balasubramanian, “An Extension of the Flow Boiling Correlation to Transition, Laminar, and Deep Laminar Flows in Minichannels and Microchannels,” *Heat Transfer Engineering,* vol. 25, no. 3, pp. 86-93, 2004/04/01, 2004.

[80] S. S. Bertsch, E. A. Groll, and S. V. Garimella, "A Composite Heat Transfer Correlation for Saturated Flow Boiling in Small Channels," *International Journal of Heat and Mass Transfer,* vol. 52, no. 7–8, pp. 2110-2118, 3//, 2009.

[81] S.-M. Kim, and I. Mudawar, "Universal approach to predicting two-phase frictional pressure drop for adiabatic and condensing mini/micro-channel flows," *International Journal of Heat and Mass Transfer,* vol. 55, no. 11–12, pp. 3246-3261, 2012.

[82] V. K. Patel, J. Seyed-Yagoobi, F. Robinson, and J. Didion, "Effect of Gravity on Liquid Film Flow Boiling Driven by Electrohydrodynamic Conduction Pumping," *AIAA Journal of Thermophysics and Heat Transfer,* vol. (under review), 2015.

[83] V. K. Patel, J. Seyed-Yagoobi, S. Sinha-Ray, S. Sinha-Ray, and A. Yarin, "EHD Conduction Pumping Driven Liquid Film Flow Boiling on Bare- and Nanofiber-enhanced Surfaces," *ASME Journal of Heat Transfer,* vol. (under review), 2015.

[84] S. Sinha-Ray, Y. Zhang, and A. L. Yarin, "Thorny Devil Nanotextured Fibers: The Way to Cooling Rates on the Order of 1 kW/cm2," *Langmuir,* vol. 27, no. 1, pp. 215-226, 2011/01/04, 2010.

[85] S. Jun, S. Sinha-Ray, and A. L. Yarin, "Pool Boiling on Nano-textured Surfaces," *International Journal of Heat and Mass Transfer,* vol. 62, no. 0, pp. 99-111, 7//, 2013.

[86] S. Sinha-Ray, S. Sinha-Ray, A. L. Yarin, C. M. Weickgenannt, J. Emmert, and C. Tropea, "Drop Impact Cooling Enhancement on Nano-textured Surfaces. Part II: Results of the Parabolic Flight Experiments [zero gravity (0g) and supergravity (1.8g)]," *International Journal of Heat and Mass Transfer,* vol. 70, no. 0, pp. 1107-1114, 3//, 2014.

[87] S. Sinha-Ray, and A. L. Yarin, “Drop Impact Cooling Enhancement on Nano-textured Surfaces. Part I: Theory and Results of the Ground (1g) Experiments,” *International Journal of Heat and Mass Transfer,* vol. 70, no. 0, pp. 1095-1106, 3//, 2014.

[88] D. H. Reneker, A. L. Yarin, E. Zussman, and H. Xu, "Electrospinning of Nanofibers from Polymer Solutions and Melts," *Advances in Applied Mechanics*, A. Hassan and G. Erik van der, eds., pp. 43-346: Elsevier, 2007.

[89] W. M. Rohsenow, “Method of Correlating Heat-transfer Data for Surface Boiling of Liquids,” *ASME Transactions,* vol. 74, no. 6, pp. 969-975, 1952.

[90] J. M. S. Jabardo, E. F. d. Silva, G. Ribatski, and S. F. d. Barros, “Evaluation of the Rohsenow Correlation through Experimental Pool Boiling of Halocarbon Refrigerants on Cylindrical Surfaces,” *Journal of the Brazilian Society of Mechanical Sciences and Engineering*, vol. 26, pp. 218-230, 2004.

[91] S. J. Kline, and F. McClintock, “Describing Uncertainties in Single-sample Experiments,” *Mechanical Engineering,* vol. 75, no. 1, pp. 3-8, 1953.

[92] R. J. Moffat, “Describing the Uncertainties in Experimental Results,” *Experimental Thermal and Fluid Science,* vol. 1, no. 1, pp. 3-17, 1988.